thermo scientific

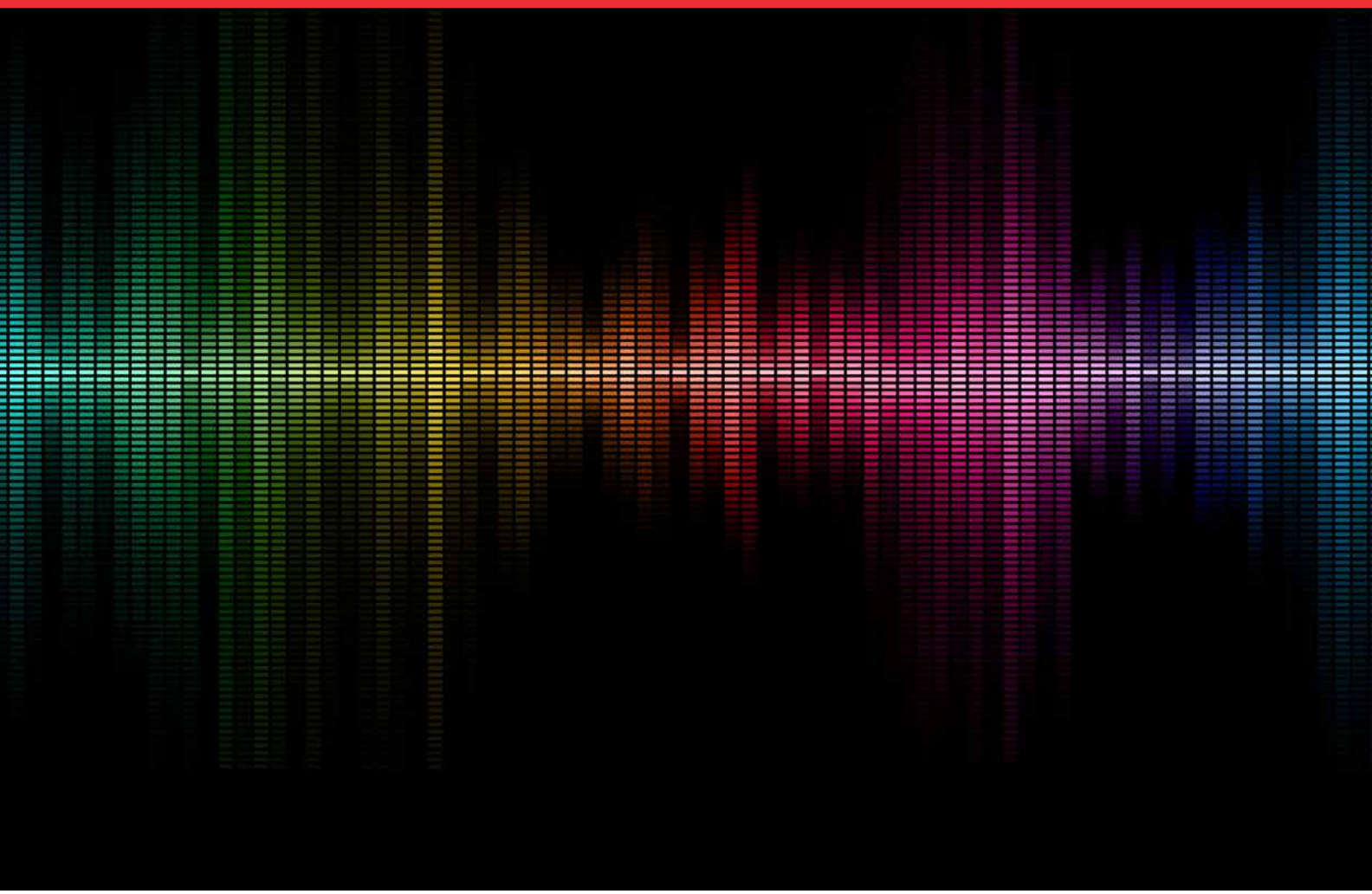

Advanced FTIR Spectroscopy

Principles, experiments and applications

ThermoFisher SCIENTIFIC

Table of Contents

Chapter 1:
Introduction to Modern FTIR Spectroscopy

1.1 Principles of FTIR: The Michelson Interferometer

Invented more than one hundred years ago, the two-beam Michelson interferometer[1] is still the heart of most modern Fourier transform infrared (FTIR) spectrometers. It consists of a fixed mirror, a moving mirror and a beamsplitter, as illustrated in Figure 1.1. The beamsplitter is a laminate material that reflects and transmits light equally. The collimated infrared (IR) beam from the source (S) is partially transmitted to the moving mirror and partially reflected to the fixed mirror by the beamsplitter. The two IR beams are then reflected back to the beamsplitter by the mirrors. The detector (D) then sees the transmitted beam from the fixed mirror and reflected beam from the moving mirror simultaneously. The two combined beams interfere constructively or destructively depending on the wavelength of the light (or frequency in wavenumbers) and the optical path difference introduced by the moving mirror. The latter is referred to as retardation, δ (cm). To obtain an interferogram, I(δ), the detector signal is digitized and recorded as a function of retardation. The interferogram intensity of a polychromatic source is mathematically describe as:[2]

$$I(\delta) = \int_{-\infty}^{+\infty} B(\sigma)cos(2\pi\sigma\delta)d\sigma \quad (1\text{-}1)$$

where $B(\sigma)$ is the spectral intensity at wavenumber σ (cm^{-1}).

The interferogram I(δ) is a simple sinusoidal wave when a monochromatic source is used, as shown in Figure 1.2. For a continuum (or polychromatic) source, I(δ) is a superposition of sinusoidal waves for IR light at all wavenumbers σ. At zero path difference (ZPD) or zero optical retardation, all the sinusoidal waves are totally constructive, producing a centerburst on the interferogram. Fourier transformation (FT) of I(δ) gives the single beam IR spectrum expressed as below:

$$B(\sigma) = \int_{-\infty}^{+\infty} I(\delta)cos(2\pi\sigma\delta)d\delta \quad (1\text{-}2)$$

In practice, a discrete Fourier transform (DFT) is used as a digital approximation of the continuous Fourier series. Thus Equation (1-2) reduces to:

$$B(k.\Delta\sigma) = \sum_{n=0}^{N-1} I(n.\Delta\delta)cos(2\pi kn/N) \quad (1\text{-}3)$$

where the continuous variables of wavenumber σ, and optical retardation δ, have been replaced by discrete values k and n, respectively. The summation is then over the total number of discrete data points N.

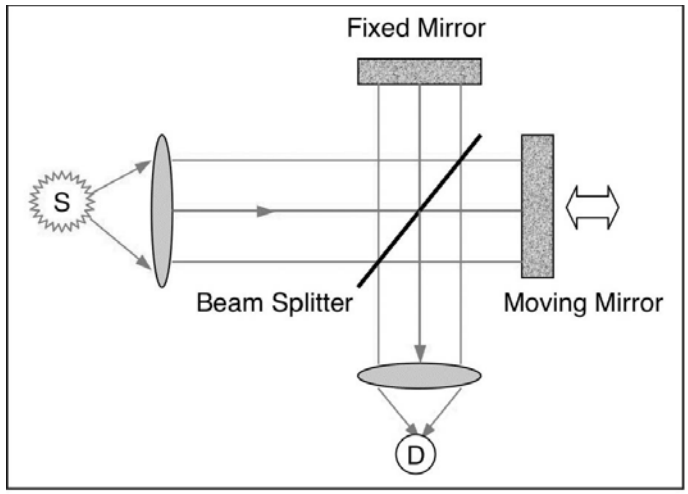

Figure 1.1. Optical diagram of a classic Michelson interferometer, which consists of three major components: a fixed mirror, a moving mirror and a beamsplitter.

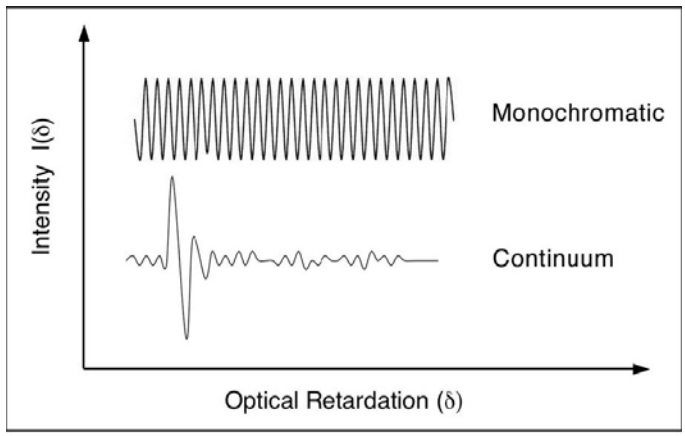

Figure 1.2. Sinusoidal and center-burst interferograms for monochromatic and continuum light sources, respectively.

1.2 Continuous-scan interferometry

In a continuous-scan FTIR spectrometer, the moving mirror moves continuously at a constant velocity, v (cm/s), and the optical path difference at time t(s) is given by $\delta = 2vt$ (cm). The interferogram data points are digitized at the zero crossings of a helium neon (HeNe) laser signal on the fly, as shown in Figure 1.3. The use of laser signal ensures that I(δ) is measured at precisely equal intervals of mirror positions and provides an internal wavelength calibration for every scan. Because of the continuous movement of the mirror, the interferogram I(δ) becomes an explicit function of time. The Fourier frequency (f_F) of IR light at wavenumber σ is given by:

$$f_F = 2v\sigma \quad (1\text{-}4)$$

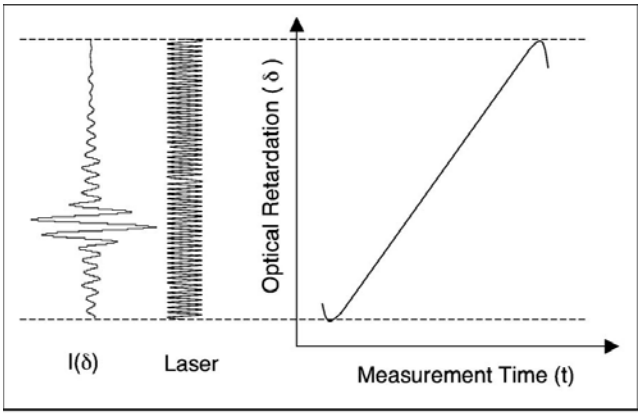

Figure 1.3. Schematic illustration of continuous-scan interferometric data collection.

Continuous-scan is a preferred choice for routine static or relatively slow kinetic measurements that require time resolution not faster than 20 ms. In this mode, the graphite bearing of the research interferometers rides on a cushion of air. This allows precise control of the mirror velocities from 0.0063 to 8.86 cm/s*. The slow velocities are chosen for thermal detectors; such as a triglycine sulfate (TGS) or a photoacoustic (PA) detector. The fast velocities are chosen for fast quantum detectors, such as a mercury cadmium telluride (MCT) or an indium antimonide (InSb) detector, for routine or kinetic measurements requiring time resolution that is not faster than 20 ms.

For dynamic and time-dependent processes occurring at rates faster than 20 ms time scales, continuous-scan is no longer useful, because the temporal Fourier frequencies become convolved with the time-dependence of the processes. These difficulties associated with continuous-scan can be overcome with step-scan interferometry. Step-scan provides advantages for spectroscopic measurements of dynamic experiments where the signal is phase-, time-, or space-dependent.[3]

1.3 Step-scan interferometry

1.3.1 Introduction

One of the research-grade Thermo Scientific™ Nicolet™ iS™50R FTIR spectrometers' advanced scanning capabilities is step-scan. In step-scan, the moving mirror moves incrementally in steps. Step-scan eliminates Fourier modulation interference encountered in continuous-scan FTIR and allows measurements to be made as an explicit function of phase, time, or space. Typical applications of step-scan FTIR can be classified into two primary categories: **1) phase-resolved spectroscopy** (PRS) for modulation experiments, such as photoacoustic depth profiling; and **2) time-resolved spectroscopy** (TRS) for fast kinetic processes down to nanosecond time scales. These powerful techniques have opened up new avenues for solving a variety of fundamental research and industrial problems in life sciences, chemistry, physics, materials sciences and many other fields.

1.3.2 Phase-, time-, and space-resolved step-scan data acquisition

Data acquisition schemes for step-scan phase-, time-, and space-resolved FTIR experiments are illustrated in **Figure 1.4**. At each sampling position of the moving mirror (usually at a zero-crossing of the HeNe laser interferogram) data are collected (or processed) at 0° (in-phase, I) and 90° (quadrature, Q) in PRS; or at time intervals defined by the sampling rate of the digitizer in TRS. Interferograms corresponding to different phases and times and are then constructed and phase-, time-, and space-resolved spectra are finally computed by performing fast Fourier transform on the interferogram data sets.

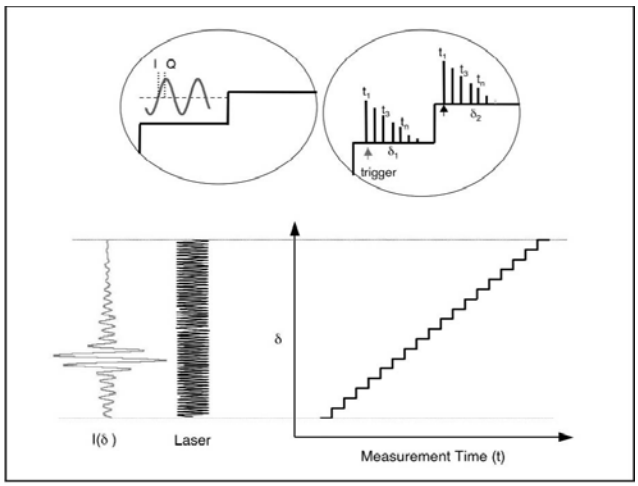

Figure 1.4. The data acquisition schemes fro phase- (left) and time-resolved (right) step-scan FTIR experiments. Interferograms corresponding to each phase and time are recorded as the mirror steps.

1.3.3 The Vectra-Piezo interferometer design

The Vectra-Piezo air-cushioned graphite step-scan interferometer, as shown in **Figure 1.5**, is the heart of research-grade iS50R FTIR spectrometers. This uniquely designed interferometer preserves some of the key performance characteristics of an air bearing and offers many unique advantages for step-scan capabilities. The performance advantages are attributed to the use of the computational power of the multi-embedded, digital signal processors (DSP) for many interferometer functions, including step-and-hold servo controls, dynamic alignment, modulation/demodulation signal generation and bench routine diagnostics. The near-zero friction of the air-cushioned interferometer with full DSP control allows the moving mirror to stop completely at a precise position for ideal step-scan data collection.

Dynamic alignment: The dynamic alignment of the Vectra-Piezo interferometer maintains the optical system of the interferometer in nearly perfect alignment during a scan. It actively compensates for any potential optical misalignment caused by ambient temperature changes or environmental

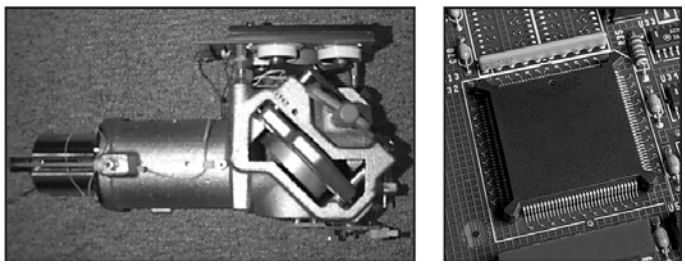

Figure 1.5. Vectra-Piezo interferometer (left) with full DSP control (right).

*The mirror velocities can also be expressed in terms of the HeNe laser modulation frequencies. The HeNe laser modulation frequency is calculated from Equation (1-4) with σ = 15,798 cm^{-1}. Therefore, the mirror velocity range 0.0063 – 8.86 cm/s, on the iS50R research spectrometers, corresponds to 199 Hz – 280 kHz, in terms of the laser modulation frequencies.

vibration disturbances and thus improves the line shape for high-resolution scans. This is accomplished by monitoring the signal phases of two orthogonally located and one centrally located, DC-coupled laser detectors at each mirror position (step). The dynamic alignment is active during the mirror pre-settling of each step, ensuring that the phases between the three laser detectors are identical to those of the previous step. Once the moving mirror comes to a complete stop for data collection, the dynamic alignment becomes inactive, thus it is referred to as smart dynamic alignment.

Mirror position accuracy. The designs of the interferometer and the advanced DSP control algorithms make the research-grade iS50R FTIR spectrometers nearly immune to ambient acoustic noises and vibrations. As shown in Figure 1.6, the mirror position accuracy is as good as ± 0.2 nm, as measured from the peak-to-peak noise of the laser signals with the instrument placed on a regular laboratory table. This peak-to-peak noise is a critical performance parameter to ensure all step-scan experimental data is collected with high signal-to-noise ratio (SNR).

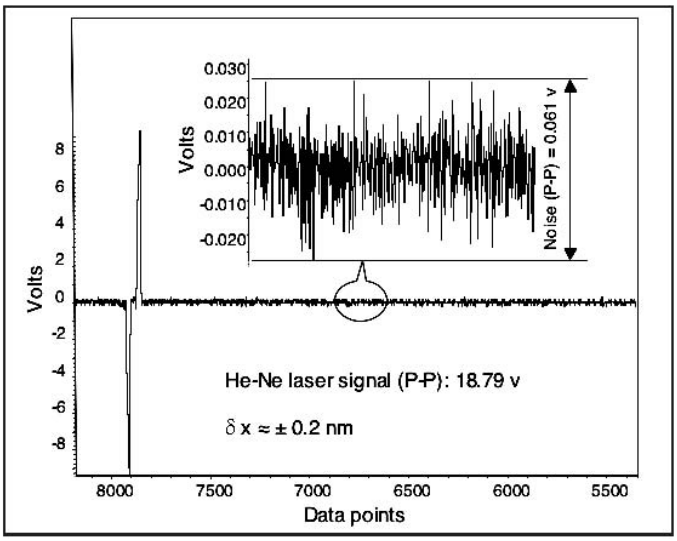

Figure 1.6. The mirror position accuracy of the iS50R Vectra-Piezo step-scan interferometer was calculated to be +/- 0.2 nm from the measured peak-to-peak noise of the HeNe laser signal.*

*The intensity of the HeNe laser interferogram generated from a Michelson interferometer, V(x), as shown in Figure 1.6, can be expressed in terms of mirror displacement, x(nm), by

$$V(x) = A\cos(4\pi\sigma x)$$

where A = 18.79/2 v, σ = 1/633 nm1. The peak-to-peak mirror position deviation, δx, can be measured from the total fluctuation (noise) of the laser signal δV (v), at any zero crossing (assume the first one, i.e. 4πσx= π/2, or x = 1/(8σ)), using the derivative of the above equation, i.e.

$$\delta V(x) = -4\pi\sigma A\sin(4\pi\sigma x)\delta x$$

Thus,

$$\left|(\delta x)_{(x=1/8\sigma)}\right| = \left|\left(\delta V(x)/-4\pi\sigma A\sin(4\pi\sigma x)\right)_{(x=1/8\sigma)}\right|$$

$$\left|(\delta x)\right| = \left|\left(0.061\nu/\left(-4\pi(18.79/2)\nu(1/633)nm^{(-1)}\right)\right)\right| = 0.33nm$$

or δx = ± 0.33/2 ≥ ± 0.2 nm.

Phase modulation/demodulation characteristics. In the Vectra-Piezo step-scan interferometer, phase modulation (ΦM)** is produced by dithering the fixed mirror along the retardation direction at a constant frequency. The DSP-controlled piezoelectric transducers actuate this dithering. The term "phase modulation" comes from the fact that the optical path difference modulation, or dithering, actually modulates the derivative, or phase, of the IR intensity.4 There are two important parameters for ΦM: modulation frequency fΦM and amplitude ε. The ΦM frequency (Hz) refers to the number of mirror oscillations per second and the ΦM amplitude measures the distance of the mirror oscillation and is usually expressed in terms of the HeNe laser wavelength (λHeNe). The raw step-scan ΦM interferogram can be expressed by modifying Equation (1-1), i.e.

$$I(\delta) = \int_{-\infty}^{+\infty} B(\sigma)\cos\left[2\pi\sigma\left(\delta + \epsilon\sin\left(2\pi f_{(\phi M)}t\right)\right)\right]d\sigma \quad (1\text{-}5)$$

The integrand in the above equation can be expanded and further expressed in terms of Bessel functions Jn(2πσε), where n=0,1,2,3, …,and sin(2mπfΦM t), where m = 1, 2, 3…. When a DSP board or a phase sensitive lock-in amplifier is used to demodulate the detector signal at the fundamental ΦM frequency, only the J1 (2πσε) term is significant, and therefore, the demodulated ΦM interferogram can be expressed as

$$I(\delta) = \int_{-\infty}^{+\infty} B'(\sigma)J_1(2\pi\sigma\epsilon)\sin(2\pi\sigma\delta)d\sigma \quad (1\text{-}6)$$

Thus, the ΦM interferogram (in the absence of phase errors) is antisymmetric with respect to the zero path difference (ZPD) and is the derivative of the amplitude modulation interferogram. In addition, the integrand is convolved with the first order Bessel function, J1(2πσε), and thus the demodulated ΦM interferogram and single-beam profiles depend on ΦM amplitude, ΦM frequency and energy of the light.

The design of the Vectra-Piezo step-scan interferometer allows ΦM frequencies and amplitudes to vary over the wide ranges typically needed for near-IR and mid-IR experiments. It offers better stability and flexibility than systems that rely on dithering a much heavier moving mirror assembly for ΦM, because the DSP easily controls the relatively lighter "fixed" mirror assembly. Figure 1.7 shows the representative laser signals for the Vectra-Piezo interferometer at a ΦM frequency of 400 Hz and amplitudes from 0.5to3.5 λHeNe, as recorded on a digital oscilloscope. The nearly perfect repeating laser fringes show that the mirror position and the ΦM amplitude are very stable and reproducible. The ability to independently control the ΦM frequency and amplitude enables users to optimize the experiment for the spectral region of interest. The modulation efficiency varies as a function of infrared wavenumber and the modulation amplitude. When the ΦM amplitude is fixed, the wavenumber-dependent profile (normally referred as the phase modulation characteristics) is given by the absolute values of the first order Bessel function. The theoretical phase modulation characteristics at amplitudes of 0.5, 1.5, 2.5, and 3.5 λHeNe are shown in Figure 1.8.

**Phase modulation is often abbreviated as PM. In this book, we use ΦB instead of PM in order to differentiate it from polarization modulation (PM), a subject to be discussed extensively in Chapter 5.

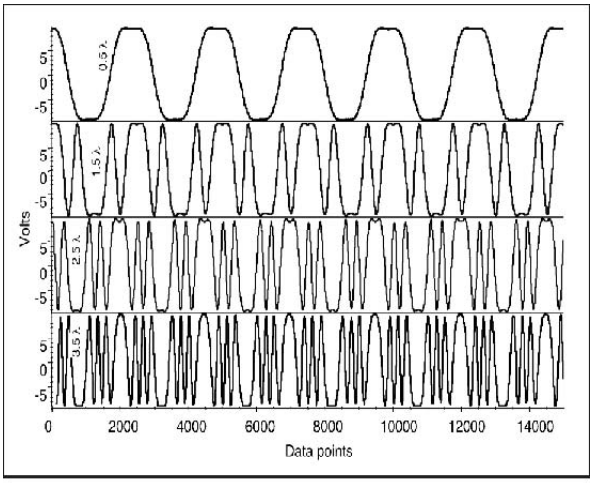

Figure 1.7. Phase modulation amplitudes in terms of the He-Ne laser wavelength from 0.5 to 3.5 $\lambda_{He\text{-}Ne}$.

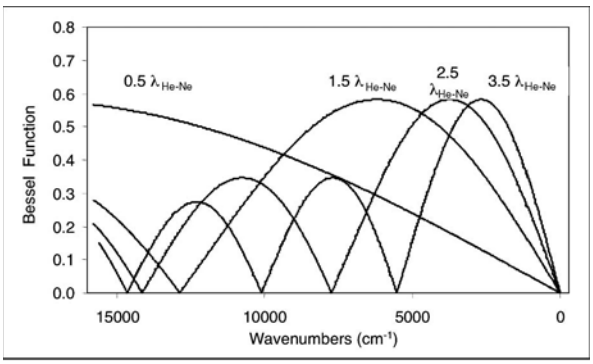

Figure 1.8. Theoretical phase modulation characteristics at amplitudes of 0.5, 1.5, 2.5 and 3.5 $\lambda_{He\text{-}Ne}$ are determined by the first order of the Bessel function.

The Bessel function characteristics contribute to the throughput profile of ΦM experiment. In general, the first lobe at the lowest wavenumber region is the largest, the lobes at higher energies become smaller in magnitude. All lobes become narrower and shift to lower energies as the ΦM amplitude increases. Figure 1.9 illustrates single-beam spectra measured with a TGS detector at a ΦM frequency of 400 Hz and a ΦM amplitudes varying from 0.5 to 5.5 λ_{HeNe}. The results are plotted on the same scale. These throughput curves are results of the combined effects of the spectrometer's normal throughput and the ΦM modulation characteristics.

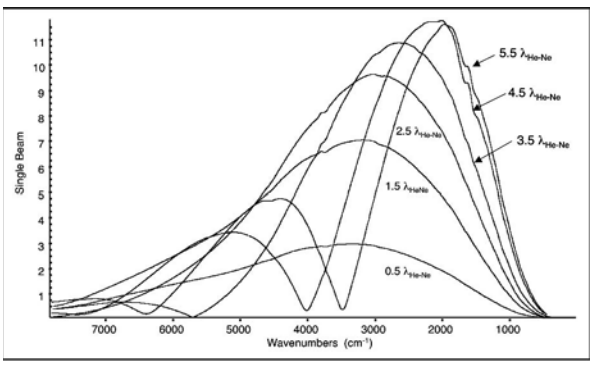

Figure 1.9. Single-beam magnitude spectra collected from step-scan ΦM experiment with different modulation amplitudes from 0.5 to 5.5 $\lambda_{He\text{-}Ne}$.

The throughput for the mid-IR region, especially the fingerprint region, is improved significantly from ΦM amplitude of 0.5 to 3.5 λHeNe. However, the throughput in the near-IR region is reduced at ΦM amplitudes of 2.5 and 3.5 λHeNe because of the presence of nodes. Thus the ΦM amplitude should be selected according to the spectral range of interest. ΦM amplitudes of 0.5 λHeNe or 1.5 λHeNe are appropriate for near IR experiments. A ΦM amplitude of 3.5 λHeNe provides excellent coverage over the entire mid-IR region. Larger ΦM amplitudes shift the largest lobe to lower energies and bring nodes (zero efficiency) into the mid-IR region. Therefore, a ΦM amplitude of 3.5 λHeNe is often chosen to optimize mid-IR throughput.

The ΦM frequency should be selected based on the characteristics of the detector and other constraints of the experiment. For example, in a sample modulation experiment where multiple modulations are used, the ΦM frequency and the sample modulation frequency should be separated by a factor of 10 or larger. For PAS depth profiling, different ΦM frequencies are used to vary the sampling depth as described in Chapter 3 of this book.

1.4 Overview of advanced FTIR applications

Research-grade iS50R FTIR research spectrometers offer a full range of step-scan operation modes, and dual-channel continuous-scan mode for polarization modulation/demodulation experiments, as well as conventional single-channel continuous-scan operation. The spectrometers are equipped with a series of highly integrated synchronous sampling technique (SST) modules. The open architecture design of these SST modules allows the research spectrometer to be configured to perform many advanced experiments. Two electronically matched digitizers are used independently or simultaneously for step-scan time-resolved or polarization modulation/demodulation dual-channel experiments. Each digitizer has an independent, software-controlled amplifier and a set of electronic highpass and lowpass filters. The dual-channel capability allows simultaneous acquisition of two channel signals. For example, in a polarization modulation-based experiment such as infrared reflection absorption (PM-IRRAS), vibrational linear dichroism (VLD) or vibrational circular dichroism (VCD) measurements, both the static (reference) and dynamic differential spectra can be measured simultaneously.

Typically, the advanced experiments that research-grade iS50R FTIR spectrometers perform can be classified into eight broadly defined experimental categories. These categories are based on different operation modes and demonstrated with thirteen representative application examples. The eight experimental categories include:

1. Extended spectral range experiments (28,000–10 cm^{-1}, i.e. from far-IR up to near ultra violet)
2. High resolution spectroscopy (better than 0.09 cm^{-1} for gas phase measurements)
3. Single-channel rapid-scan kinetics (90 spectra/sec at 16 cm^{-1} resolution)
4. Dual-channel polarization modulation spectroscopic experiments (IRRAS, VLD and VCD, absorbance level on the order of 10-3 to 10-5)
5. Step-scan amplitude modulation (electroluminescence measurement)

6. Step-scan phase modulation (photoacoustic depth profiling
7. Step-scan sample modulation (liquid crystal dynamics and spectro-electrochemistry)
8. Step-scan time-resolved spectroscopy (nano-second chemical kinetics, liquid crystal dynamics and photo-acoustic depth profiling).

The potential for other modulation and TRS experiments is unlimited. Combined techniques from different categories may also be used, enabling experiments such as TRS-based PM-IRRAS, kinetic PM-IRRAS and so forth. The relationship between these typical experiments is summarized in Figure 1.10. In the following chapters, these experiments will be addressed in more detail.

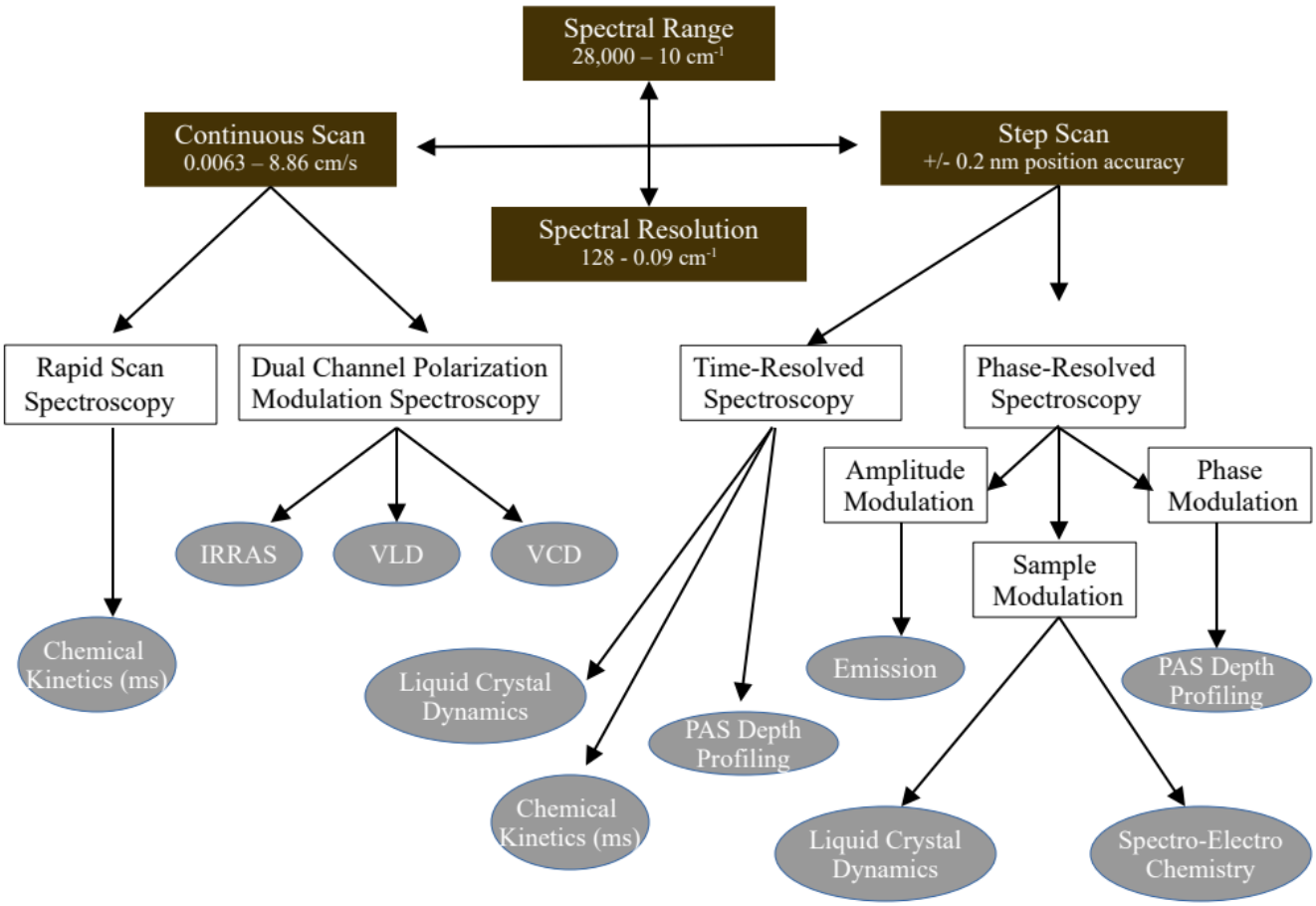

Figure 1.10. The relationship between classes of advanced FTIR experiments.

Chapter 2:
High-Resolution, High-Speed and Spectral Range Extension of FTIR

2.1 High-resolution FTIR spectroscopy

Research-grade iS50R FTIR spectrometers provide a wide range of software-selectable spectral resolution $\Delta\sigma$, from 128 to 0.125 cm^{-1}. The high-resolution capability (better than 0.5 cm^{-1}) is often needed for gas phase analysis due to the rotational fine structure present in the vibrational spectra of gaseous molecules. The highest spectral resolution of 0.125 cm^{-1} is achieved by translating the moving mirror to the extreme position at 0.5 ($1/\Delta\sigma$) = 4 cm away from the ZPD location, or the centerburst of an interferogram. However, since the data points (Ns) sampled on one side of the interferogram are a power of 2 required by current OMNIC™ software in the continuous-scan mode, the spectral resolution $\Delta\sigma$ is then defined by the interferometric data points actually collected when 0.125 cm^{-1} is chosen on the software for the data acquisition, i.e.

$$\Delta\sigma = 2\sigma_{max}/N_s = 2x7902cm^{-1}/131{,}072 = 0.121cm^{-1} \quad (2\text{-}1)$$

where σ_{max} is the maximum wavenumber allowed with the sample space (undersampling ratio) of 2. Therefore the actual spectral resolution is slightly higher than the software defined. Note that the average full width at half height (FWHH*) of the peaks over the entire CO band region is 0.084 cm^{-1} (with a standard deviation of 0.002 cm^{-1}) when spectral resolution of 0.125 cm^{-1} is selected by OMNIC software. Thus, an actual spectral resolving capability of better than 0.09 cm^{-1} for the natural separation of two identical lines is achieved.[5] Figure 2.1 shows a spectrum of the standard CO sealed gas cell in the region of 2250 – 2000 cm^{-1} with an expanded view of the spectrum around the peak at 2180 cm^{-1}. This spectrum was obtained with standard boxcar apodization function and a software selected resolution of 0.125 cm^{-1}.

2.2 Rapid-scan FTIR spectroscopy

Rapid-scan capability on the research-grade iS50R FTIR spectrometers is based on continuous-scan mode. It allows the study of reactions or processes as fast as 11 ms (or 90 spectra/sec) at a spectral resolution of 16 cm^{-1} (or 8 cm^{-1} data resolution due to a zero filling factor). The synchronization between the spectrometer measurements and the process under study can be easily achieved using an optional Remote Start Cable (RSC) with the iS50 hub. This cable passes a trigger signal from the spectrometer to your experiment. Thus a precisely timed signal can be provided to the experiment. The RSC further allows you to start data collection from a remote location.

Rapid-scan is applicable to many kinetic processes as long as the rate of process is under the limit of the spectrometer speed. Applications of rapid-scan FTIR include monitoring liquid phase dispersion, gas phase mechanics and many chemical reaction kinetics such as polymer curing and so forth.[6] Figure 2.2 shows a series of rapid scan spectra of a butane flame generated from a Weber™ lighter with periodic spark ignitions, collected at a speed of 77 spectra/sec, and spectral resolution of 16 cm^{-1}. When a reaction process is much faster and on the scale of microsecond or nanosecond, a step-scan FTIR with a fast TRS digitizer is required. Microsecond and nanosecond time-resolved applications will be addressed in detail in Chapter 4.

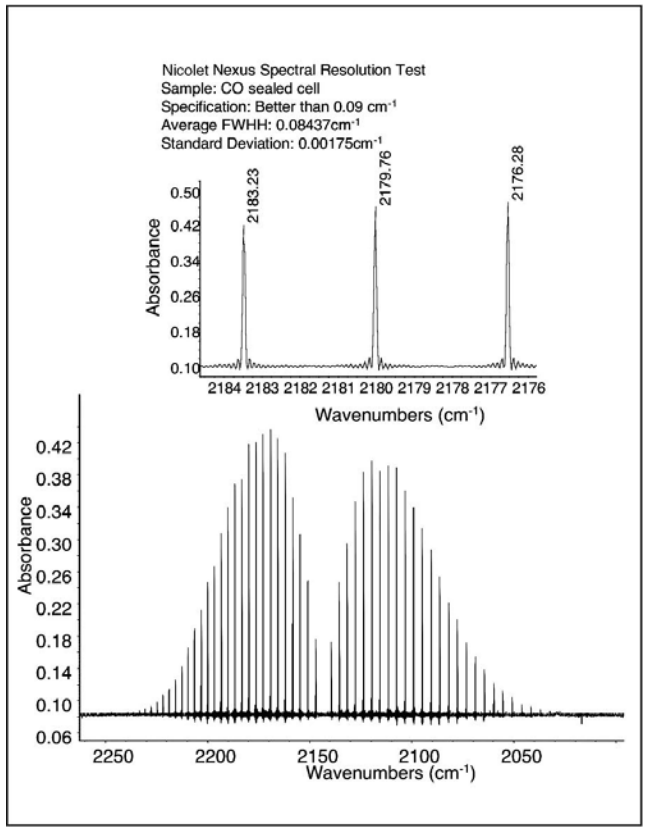

Figure 2.1. High-resolution spectrum from 2250 – 2025 cm^{-1} (bottom) and expanded view from 2184-2176 cm^{-1} (top) of a standard CO sealed gas cell indicate an average FWHH (or approximately, spectral resolution) 0.084 cm^{-1}.

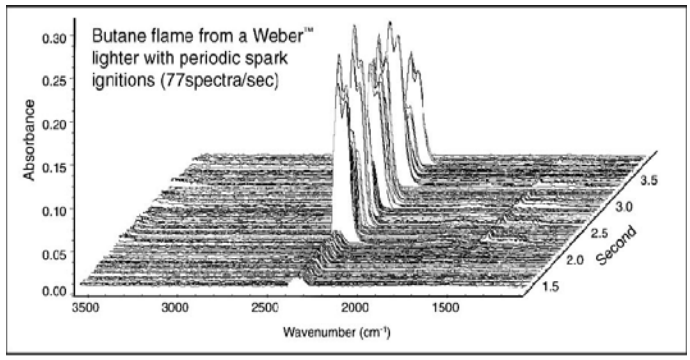

Figure 2.2. Monitoring ignition process of butane flame using rapid-scan FTIR with an MCT detector at a data collection speed of 77 spectra/sec.[1]

*FWHH is a classic (less strict) definition of spectral resolution, known as Houston criterion, which applies more appropriately to line spectra.

2.3 Spectral range extension of FTIR spectroscopy

Research-grade iS50R FTIR spectrometers facilitate spectroscopic measurements over a wide range from far-IR to near-ultraviolet. Since mid-IR and near-IR spectroscopies have been addressed elsewhere in our literature, only the far-IR, and UV-Vis spectroscopic regions are discussed in this section.

2.3.1 FT-far-IR spectroscopy

The far-IR spectral region is generally considered below 600 cm^{-1}. Although many organic compounds are far-IR active, this spectral region is particularly useful for inorganic studies. Absorption due to the stretching and bending vibrations of bonds between metal atoms and inorganic/organic ligands generally occurs at frequencies lower than 600 cm^{-1} (>17 µm). In the basic far-IR configuration on a research-grade iS50R FTIR Spectrometer, a standard Thermo Scientific Ever-Glo™ IR source and a Thermo Scientific Solid-Substrate™ beamsplitter are combined with a polyethylene-windowed deuterated lanthanum doped triglycine sulfate (DLaTGS) detector. The Thermo Scientific patented Solid-Substrate beamsplitter provides coverage for the full far-IR spectral region. This single optical element eliminates the need to use multiple beamsplitters to cover the whole far-IR region (by comparison, three mylar beamsplitters of differing thickness are required to span the far-IR region). The Solid-Substrate beamsplitter is rigid and eliminates problems with beamsplitter flexing during the Michelson interferometer scan cycles, while maintaining a flatness similar to a wire grid beamsplitter. A far-IR water vapor spectrum and a 100% line collected with the basic far-IR configuration are shown in Figure 2.3.[8]

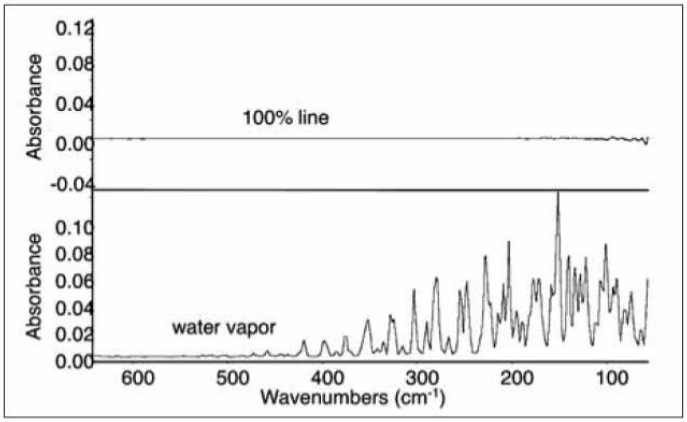

Figure 2.3. 100% line (upper) and water vapor spectrum (lower) in the far-IR region collected from a research-grade Nicolet FTIR Spectrometer with a Solid-Substrate beamsplitter, Ever-Glo IR source and a polyethylene windowed DLaTGS detector.

Atmospheric water vapor exhibits strong spectral features in the far-IR region, particularly below 400 cm^{-1}. Three alternative methods are commonly used to reduce this atmospheric contribution: 1) use of a sample shuttle to alternate background and sample collection; 2) removal of water vapor by purging the instrument with N2 or dry air, and 3) evacuating water vapor under vacuum. The sample shuttle device works well for thin film/pellet-based transmission measurements but is not ideal for other sampling methods, such as attenuated total reflectance (ATR) and diffuse reflectance. Effectively purging the system with N_2 works well for almost all sampling techniques, as partially demonstrated by Figures 2.3-2.4. Evacuating the water vapor with a vacuum system is a mechanically effective approach, but this option is costly and limits your sampling capabilities. It introduces problems with sample outgassing and overheating of

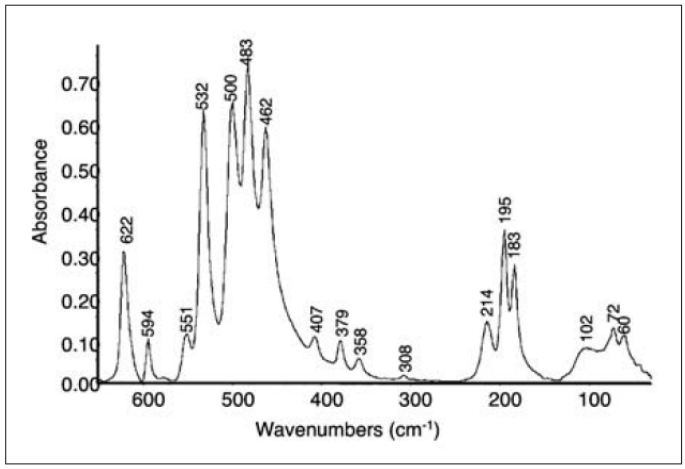

Figure 2.4. Far-IR spectrum of acetylferrocene on a research-grade Nicolet FTIR Spectrometer with a Solid-Substrate beamsplitter, Ever-Glo source and a helium cooled Si bolometer.

the electronic and optical components of the system. Evacuation of the system is only necessary in exceptional circumstances Furthermore the mechanical complexity of vacuum systems limits their popularity.

2.3.2 FT-UV-visible spectroscopy

The UV-Vis spectral regions are classically defined as: far UV, 1,000,000 – 50,000 cm^{-1} (10200 nm); near UV, 50,000 – 26,300 cm^{-1} (200 – 380 nm) and visible, 26,300 – 12,800 cm^{-1} (380780 nm). The absorption of UV-Vis radiation generally results in the excitation of bonding electrons, such as electron transitions involving π, σ, n, d and f electrons as well as charge-transfer electrons. Consequently, the wavelengths of absorption peaks can be correlated with the types of bonds that exist in the species under study. Therefore UV-Vis spectroscopy is valuable for identifying functional groups in a molecule and also quantitative determination of compounds containing absorbing groups.

Dedicated monochromator-based UV-Vis spectrometers, such as the Thermo Scientific Evolution™ series,[9] are widely used for UV-Visible spectroscopic measurements. Research-grade iS50R FTIR spectrometers can be optionally configured to cover the

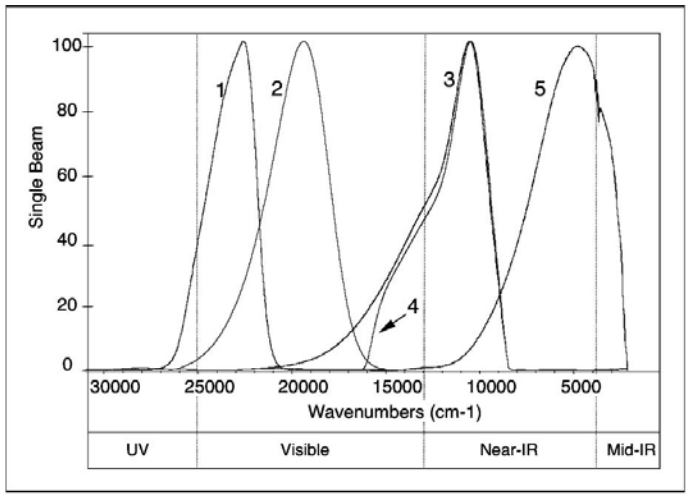

Figure 2.5. Single-beam spectra of quartz-halogen source over the range 28,000 – 2,000 cm^{-1} with different combinations of detectors, beamsplitters, and optical filters. 1) Quartz beamsplitter, Si detector and narrow blue filter; 2) Quartz beamsplitter, Si detector and wide blue filter; 3) Quartz beamsplitter, Si detector and no optical filter; 4) Quartz beamsplitter, Si detector and red filter; 5) CaF_2 beamsplitter, PbSe detector and no optical filter.

near-UV and nearly full range of visible spectroscopic regions (27000 – 12800 cm^{-1}). This configuration contains a quartz-halogen light source (28000 – 2000 cm^{-1}), a quartz beamsplitter (28,000 – 2,800 cm^{-1}), a silicon detector (2,700 – 8,600 cm^{-1}), and wide and narrow blue filters. Blue filters are used to optimize the spectral result, to block any unwanted energy from reaching the detector (such as interference from the HeNe laser at 15798 cm^{-1} or energy at lower wavenumbers), and to prevent folding of adjacent spectral regions into the desired region. Single-beam spectra of the quartz-halogen source from 28,000 to 2,000 cm^{-1} with different combinations of detector (Si or PbSe), beamsplitter (Quartz or CaF_2) and optical filter (narrow blue, wide blue or red) are shown in Figure 2.5.

The diffuse reflectance spectrum of yttrium chloride from 25,000 to 2,000 cm^{-1} is shown in Figures 2.6.[10] To optimize the near-IR regions, a red filter was used for spectral region 14,000 – 9,000 cm^{-1}, a CaF_2 beamsplitter, and a PbSe detector were used for spectral region 9,000 – 2,000 cm^{-1}.

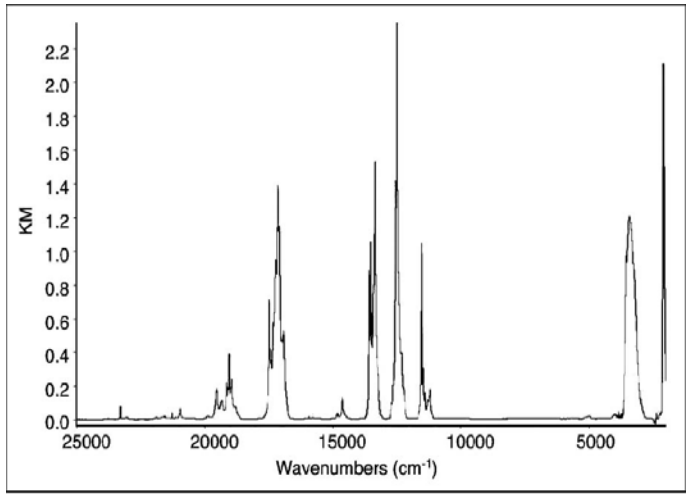

Figure 2.6. Diffuse reflectance spectrum of yttrium chloride from 25,000 – 2,000 cm^{-1}. Different beamsplitters and detectors were used to optimize the entire spectral region.

Chapter 3:
Step-scan Phase-resolved Spectroscopy (S^2PRS) – Modulation Experiments

3.1 Introduction

Step-scan phase-resolved spectroscopy (S^2PRS) includes three types of modulation techniques: **1) amplitude modulation** (IR intensity chopping); **2) phase modulation** (mirror dithering along the retardation direction or path difference modulation); and **3) sample modulation** (sample under an external, usually sinusoidal, physical perturbation). In S^2PRS experiments, the raw detector signal can be demodulated by an external lock-in amplifier,[11] a dedicated demodulator,[12] or an internal DSP circuitry-based demodulator.[13, 15]

In the early 1990's when multiple modulations were applied to the system, multiple lock-in amplifiers were required for sequential demodulations at different modulation frequencies. Today, research-grade iS50R FTIR spectrometers are fully equipped with internal DSP demodulators, and thus experiments requiring lock-in amplifiers have been greatly simplified. The spectrometers also keep the external input channel option when an arbitrary external sinusoidal modulation and a lock-in amplifier are used, as in amplitude modulation (AM) experiments. In a typical DSP-based S^2PRS data collect, two orthogonal outputs at phase angles 0° (I, in-phase) and 90° (Q, quadrature) are generated and recorded simultaneously. The following sections in this chapter will present typical applications for all three modulation techniques.

3.2 Amplitude modulation FTIR– electroluminescence measurement

In a step-scan amplitude modulation (AM) experiment, the intensity of the IR beam is modulated periodically by either chopping, synchronously varying the emission of a sample, or exciting the sample with synchronously varying sources. In all cases, the energy hitting the detector varies at a constant frequency. The raw signal from the detector is first fed externally to a lock-in amplifier referenced to the same modulation frequency. The maximized in-phase output signal is then digitized, recorded and Fourier transformed to obtain a step-scan AM spectrum.*

A typical application of step-scan AM is the characterization of electroluminescence of light-emitting devices in the mid- and near-IR regions, with less restriction on the modulation frequency range. The Fourier frequency is eliminated in step-scan AM, and the modulated electrical or optical excitation with a desired single frequency is applied to the entire spectrum. This allows the device modulation to be tuned in a relatively wide range of frequencies from ~10 to 100 kHz. In contrast, if a continuous-scan mode is chosen, the device frequency should be at least a factor of ten times higher than the fastest Fourier frequency, $f_F = 2v\sigma$, in the spectral region of the measurement, where v is mirror velocity (cm/sec) and σ is IR wavenumber (cm^{-1}). This requirement restricts the range of electrical or optical modulation frequencies that can be used to produce emission output, particularly in the lower modulation frequency range (~10 kHz).

*By maximizing signals in the in-phase channel (I) the AM spectrum is virtually the approximation of the power or magnitude spectrum (M) according to the relationship $M = (I^2 + Q^2)^{1/2}$.

Figure 3.1 shows a step-scan amplitude modulation electro-luminescence spectrum of an iron-doped indium gallium arsenic phosphide (Fe:InGaAsP) LED with spectral resolution of 0.5 cm^{-1}. The phonon sidebands are associated with different acoustic, optic, and localized vibrational modes.[16] Since the emission power is weak, on the order of 10 nW, low-duty cycles or low modulation frequency is required for this measurement. Bands at high wavenumbers around 2825 cm^{-1} are attributed to intra-center transitions within the 5D states of the Fe_2+ ions substituted for indium and isotopic shift ($^{54}Fe/^{56}Fe$). Bands between 2600 and 2500 cm^{-1} are phonon sidebands that are associated with different acoustic, optic, and localized vibrational modes. The advantage of step-scan AM measurements on miniature and low-power output is evident in the quality of the high-resolution spectrum.

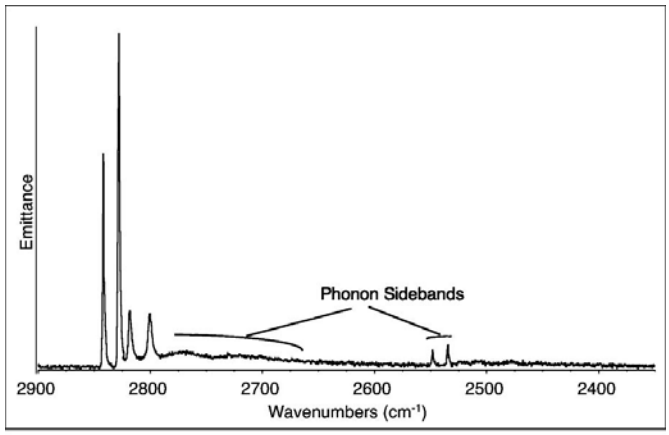

Figure 3.1. Step-scan AM emission spectrum of an iron=doped indium gallium arsenic phosphide (Fe:InGaAsP) light emitting device (LED) with spectral resolution of 0.5 cm^{-1}.

3.3 Phase modulation FTIR – photoacoustic (PA) spectral depth profiling

3.3.1 Introduction

As discussed in Chapter 1, in a research-grade iS50R FTIR interferometer, the step-scan phase modulation (ΦM) is produced by dithering the fixed mirror along the retardation direction at a constant frequency. One of the most significant applications of step-scan ΦM is photoacoustic (PA) spectral depth profiling.[17] Photoacoustic spectroscopy (PAS) has gained much attention and popularity in chemical analysis due to a unique combination of the following features: nondestructive, noncontact measurement; simple sample preparation; depth profiling (resolving) capability; and high signal saturation limit. PAS can be used for analyzing solid samples of almost any form (polymers, rubbers, dyes, and papers, etc.) in any shape (bulky, powdered, or fibroid, etc.), and it is good for spectral measurement of strong absorbers or depth profiling of heterogeneous samples. PA spectral depth profiling takes advantages of two fundamental aspects of the photothermal effect. The first is the variation of thermal probing depth with ΦM

frequency, and the second is the dependence of the PA signal phase on the depth (as well as on absorptivity) of the absorber(s). Both subjects will be discussed in this chapter. In addition, continuous-scan FTIR PAS will be presented for comparison.

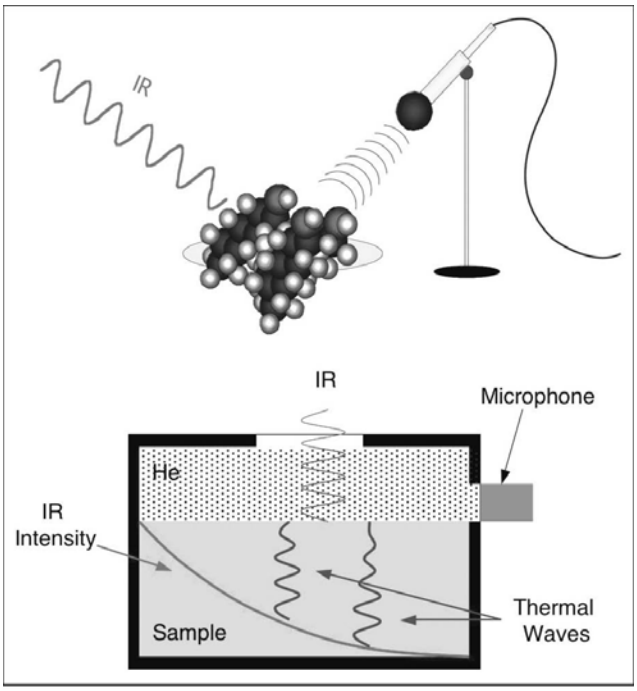

Figure 3.2. Schematics of photoacoustic signal generation and detection, which involve three major steps: absorption of modulated light by the sample; thermal energy diffusion in the medium; and sound intensity detection by the microphone.

3.3.2 PA effect, signal generation and detection

The PA effect was discovered by Alexander Graham Bell in 1880.[18] In a condensed-phase PA experiment, PA signal generation includes absorption of modulated optical illumination (modulation frequency within an acoustic range) by the sample, thermal diffusion from within the sample to adjacent medium (usually helium) and pressure oscillation of helium. The pressure wave (sound) is then detected using a very sensitive microphone. This process is illustrated in Figure 3.2.

The PA signals depend on many factors, including the intensity and modulation frequency of light, thermal, optical and geometric properties of the sample, cell and media. The onedimensional thermal piston model proposed by Rosencwaig and Gersho for the PA effect in condensed-phase matter, i.e. the RG theory,[19, 20] has been most widely referenced in literature. In the RG theory, the PA signal originating from a homogeneous solid sample is described as the pressure variation of the gas in the PA cell, ΔP(t), i.e.

$$\Delta P(t) = \left(\gamma P_0 \mu_g T_s(0,\omega)/\sqrt{2} l_g T_0\right) exp\left[i(\omega t - \pi/4)\right]$$

$$= \left(\gamma P_0 \mu_g T_{s0}/\sqrt{2} l_g T_0\right) exp\left(i(\omega t - \pi/4 - \Phi\right)$$

where ω is the angular modulation frequency of the incident light, γ is the ratio of the specific heats (Cp/Cv) of the sample, P0 and T0 are the static pressure and the average temperature of the PA cell gas respectively, Ts(0,ω) is the complex temperature at the solid-gas boundary (surface), lg is the distance from the surface of the sample to the cell window, and μg the thermal diffusion depth of the cell gas. It can be seen that the PA signal has both magnitude and phase, and it depends primarily on the temperature of the surface of the sample. The magnitude represents the strength of a PA signal and the phase is a signature of its spatial origin. Simplifications of Equation (3-1) can be made on different optical and thermal conditions of a sample under study. In general, as a conceptual understanding of the relationship, the PA signal is approximately proportional to log10(βμ), over the region of 1 < log10(βμ) < +1, where β is optical absorptivity and μ is thermal diffusion depth.[21] Since thermal diffusion is relatively slow and thermal waves damp out quickly, only those generated within a certain sampling depth will be primarily detected. Thus, the thermal diffusion length (μ) also represents the sampling depth and is given by,

$$\mu = \left(\alpha/\pi f\right)^{(1/2)} \quad (3\text{-}2)$$

here f is the modulation frequency (or Fourier frequency in continuous-scan mode) and α is the thermal diffusivity [$\alpha = \kappa/(\rho C_p)$, where κ, ς and C_p are thermal conductivity, density and specific heat of the sample, respectively].

3.3.3 PA signal phase and phase difference models

As briefly mentioned above, the PA signal phase directly contains spatial information about the signal origin, and thus it is of great importance in spectral depth profiling analysis. Even for homogeneous samples, PA signals would exhibit phase lags with respect to the optical modulation because thermal diffusion is much slower (on the order of 10^6 – 10^3 second) than optical penetration (absorption) (10^{15} – 10^{13} second). The phase lags depend on the modulation frequency, the instrument, and the spatial origin of the signals. A finite time delay (Δt) for a PA signal generated from a deeper layer of a sample to reach the microphone with respect to the surface PA signal can be related to the phase difference by Equation (3-3):

$$\Delta\Phi = 2\pi f(\Delta t) \quad (3\text{-}3)$$

In general, as depicted in Figure 3.3, PA signals originating from deeper parts of a sample have greater phase lags than those from the shallower parts, and vice versa. In addition, smaller phase lags are associated with stronger bands from the same layer when this layer is thermally thick (the layer is thicker than the thermal diffusion depth) or optically opaque (the layer is thicker than the optical penetration depth).

A quantitative expression of PA signal phase for multilayered materials, as an extension to the classic RG theory for homogeneous solids, has been developed.[22] For layer j of any thermally thick or optically opaque material, the total PA signal phase lag Φj,total relative to the phase of the light modulation can be expressed by Equation (3-4):

$$\Phi_{(j,total)}\left(\sigma_j\right) = \Phi_0 + \pi + \sum_{n=0}^{j-1}\left(d_n/\mu_n\right) - tan^{-1}\left[B_j\mu_j + 1\right] \left(j = 1,2,\ldots m\right) \quad (3\text{-}4)$$

where d, β, μ are the thickness, optical absorption coefficient, and thermal diffusion depth for layer j or n, respectively*. It can be seen from Equation (3-4) that this total PA phase lag is due to the thermal transport within this absorbing layer, the thermal transport within all above transparent layers (from 1 to j1) and the

*The assumptions d0 = 0 and μ0 not equal to 0 are used for mathematical convenience in deriving PA phases for all layers, and thus d0 is not defined as the "thickness" of the PA cell gas.[22]

total relative phase angle shift due to all external factors (positioning of the sample, PA cell resonance, spectrometer, etc.), Φ0 (constant for a given sample at a particular modulation frequency of a given instrument). When layer j is both thermally thin and optically transparent, Equation (3-4) becomes:

$$\Phi_{(j,total)}\left(\sigma_j\right) = \Phi_0 + \pi/2 + \sum_{n=0}^{j-1}\left(d_n/\mu_n\right)\left(j = 1,2,\ldots m\right) \quad \text{(3-5)}$$

Using Equations (3-4) and (3-5), phase difference models for various scenarios can be derived. Assuming a multilayer sample with layer j above layer k, Equation (3-6) and (3-7) show two useful cases for practical PA phase analysis of multi-layered samples. Equation (3-6) holds for the case in which both layers j and k are thermally thin (with respect to μ_j and μ_k) and optically transparent (with respect to $\beta_j(\sigma_j)$ and $\beta_k(\sigma_k)$). Equation (3-7) describes the case in which layer j is thermally thin (with respect to respect to μ_j) and optically transparent (with respect to $\beta_j(\sigma_j)$) and layer k is thermally thick (with respect to μ_k) or optically opaque (with respect to $\beta_k(\sigma_k)$):

$$\Delta\Phi_{(j,k)} = \sum_{n=j}^{k-1}\left(d_n/\mu_n\right) \quad \text{(3-6)}$$

$$\Delta\Phi_{(j,k)} = \pi/2 + \sum_{n=j}^{k-1}\left(d_n/\mu_n\right) - tan^{-1}\left(\beta_k\mu_k + 1\right) \quad \text{(3-7)}$$

Further simplification can be made when dealing with two-layer samples. Applications of these models for thickness determination will be further demonstrated in **Section 3.3.8**.

3.3.4 Continuous-scan FTIR PAS

The coupling of a PA detector to a continuous-scan FTIR, as first demonstrated in the late 1970's[23,24] and early 1980's[25,26] combines all the interferometric advantages (throughput, multiplexing and registration) with those unique features of PAS as described in **Section 3.3.1**. Thus FTIR PAS can be used for convenient qualitative identification or nondestructive depth profiling of a variety of samples. Although PAS can be used in any region of the electromagnetic spectrum, it is particularly effective in the infrared. Especially for organic materials, distinctive infrared functional group absorption bands afford layer, and/or component identification not often possible in the UV/Vis region. In the infrared, the broad spectral range and high throughput of FTIR make it the most versatile spectral technique for use with PA detection.

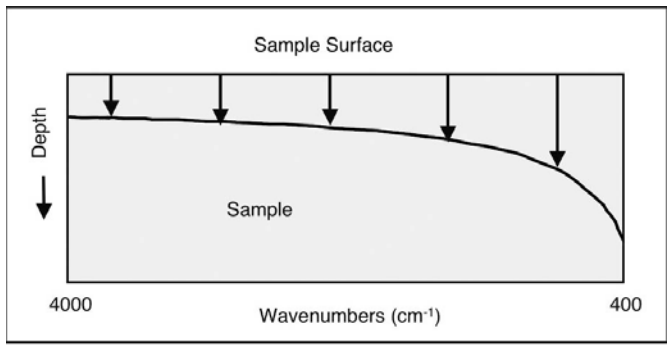

Figure 3.4. Probing depth varies as a function of wavenumber (σ) in continuous-scan FTIR PAS.

Continuous-scan FTIR PAS is widely used for measuring spectra of homogeneous samples as a routine sampling method for samples that can be challenging using other techniques. In continuous-scan FTIR, the Fourier frequency, $f_F = 2v\sigma$ [where v is mirror velocity (cm/sec) and σ is IR wavenumber (cm^{-1})], is the actual modulation frequency of IR light. According to Equation (3-2), PAS sampling depth in the continuous-scan mode depends on both the mirror velocity and IR wavenumber. Modulation frequencies for different wavenumbers at different optical velocities (twice the mirror velocity) on the iS50R FTIR research spectrometers are listed in Table 3-1. Since the modulation frequency varies with wavenumber in continuous-scan PAS sampling, the probing depth (μ) varies across the entire spectrum as illustrated by Figure 3.4. According to Equation (3-2), the probing depth at 400 cm^{-1} is about three times deeper than that at 4000 cm^{-1} in a continuous-scan PAS spectrum:

$$\mu_{400}/\mu_{4000} = \left(f_{4000}/f_{400}\right)^{(1/2)} = 3.16$$

Optical Velocity (cm/s)	He-Ne Laser Modulation (kHz)	4000 cm^{-1} (Hz)	2000 cm^{-1} (Hz)	1000 cm^{-1} (Hz)	400 cm^{-1} (Hz)
8.22	130.0	32,880	16,440	8,220	3,288
0.63	10.0	2,520	1,260	630	252
0.47	7.5	1,880	940	470	188
0.32	5.0	1,280	640	320	128
0.16	2.5	640	320	160	64
0.063	1.0	252	126	63	25
0.047	0.75	188	94	47	19
0.032	0.50	128	64	32	13
0.016	0.25	64	32	16	8

Table 3.1. IR and He-Ne laser modulation frequencies (Hz) at different optical velocities and wavenumbers.

For heterogeneous or layered samples, the variation in sampling depth across the entire spectral region makes the interpretation of a continuous-scan PAS spectrum somewhat ambiguous, because the spectral features in different regions could come from different layers. In order to simplify continuous-scan PAS spectral depth profiling analysis, a small portion of the spectrum, or a distinctive band is often monitored across all spectra taken at different velocities. In addition, the lack of a discrete modulation frequency in the continuous-scan mode makes extraction of PA signal phase difficult. As discussed earlier in **Section 3.3.3**. and further elucidated later in **Sections 3.5.5**. and **3.5.6**., the PA phase information is a signature of PA signal origin and can be used to enhance spatial resolution and determine layer thickness of samples. These two problems limit the use of continuous-scan FTIR PAS for spectral depth profiling of heterogeneous materials. Finally, at a constant velocity of the moving mirror, the PA signal becomes much weaker at higher wavenumbers (shorter wavelengths) because the Fourier frequency (f_F) depends on the wavenumber (σ) of the light and the velocity of the moving mirror (v), i.e. $fF = 2v\sigma$. As a consequence, FT PAS in the visible spectral region is not feasible in the continuous-scan mode.

3.3.5 Step-scan phase modulation ($S^2\Phi M$) FTIR PAS: Principles

The limitation of continuous-scan PAS can be overcome by coupling the photoacoustic cell with a step-scan phase modulation ($S^2\Phi M$) FTIR spectrometer. First, $S^2\Phi M$ operation removes the spectral multiplexing of the interferometer from the time domain; there are effectively no (temporal) Fourier frequencies. A single-frequency phase (path difference) modulation applied to the fixed mirror is therefore used to modulate all wavelengths of the radiation to generate the PA signal, resulting in a uniform probing depth across the entire spectrum as shown in Figure 3.5.

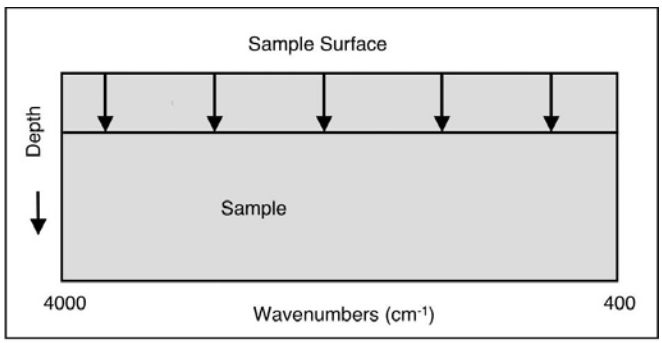

Figure 3.5. Uniform probing depth achieved with step-scan phase modulation FTIR PAS.

Secondly, the use of a discrete phase modulation frequency (or several frequencies) offers the convenience of using digital signal processing (DSP)[13-15] techniques to demodulate the PA signal and extract the signal phase from the simultaneously generated in-phase, I(σ), and quadrature, Q(σ), components of the signal. Thus the elimination of the wavelength-dependent instrument phase in the calculation of the PA signal phase, $\Phi(\sigma)$, and magnitude, M(σ), spectra is made possible,[27] as illustrated by Equations (3-8) and (3-9):

$$\Phi(\sigma) = tan^{(-1)}\left[Q(\sigma)/I(\sigma)\right] \quad (3\text{-}8)$$

$$M(\sigma) = \left[I(\sigma)^2 + Q(\sigma)^2\right]^{(1/2)} \quad (3\text{-}9)$$

In $S^2\Phi M$ FTIR PAS, the probing depths can be calculated from Equation (3-2) if the properties of the sample are known. For most organic polymeric materials, their thermal diffusivity values $\alpha \cong 0.001$ cm^2/s, thus the sampling depth at different ΦM frequencies can be calculated using this simplified equation:

$$\mu = 180/\left(f^{(1/2)}\right)\mu m \quad (3\text{-}10)$$

Some representative data based on Equation (3-10) are listed in Table 3-2. For example, under a typical parameter setting of ΦM frequency 100 Hz, and ΦM amplitude 3.5 λHeNe, the probing depth (μ) for most homogeneous organic polymers is about 18 μm and the energy profile optimizes mid-IR spectral measurements. When heterogeneous/layered samples are involved, the actual probing depth can be as deep as 2μ if the surface layer(s) is (are) acting as an IR transparent window over the absorption region of the base layer.[28] By changing phase modulation frequency, one is able to obtain frequency-resolved spectral depth profiling results. Thus $S^2\Phi M$ FTIR is a preferred choice for PA spectral depth profiling. Furthermore, $S^2\Phi M$ technique not only offers an advantageous choice for FT PAS in mid-IR region but extends FT PAS to ultraviolet/visible/near-infrared (UV/Vis/NIR) spectral regions with reasonable signal strength (by using a single, low-frequency modulation).

The use of PA signal phase, either alone or in combination with the variation of the modulation frequency, usually offers the prospect of much greater detail in depth profiling than use of the modulation frequency alone.[29-35] To properly generate PA phase data, a PA phase calibration is required. This calibration is performed by using a strongly absorbing material such as carbon black-filled rubber or glassy carbon to establish a “surface phase” reference.

There have been several ways of using PA phase for depth profiling analysis. The first approach[36] is simply the direct use of in-phase (I) and quadrature (Q) spectra. By using the surface phase reference, the in-phase spectrum enhances the surface absorption features and quadrature will enhance those of the substrate. The second approach is to rotate the detection phase either in a trial-and-error approach[28,37] or by systematic, continuous rotation,[30, 32-36] to eliminate certain bands from the spectrum or to illustrate the variation of intensity of relevant bands as a function of detection phase angle. By comparing the

f(Hz)	μ (μm)
5	80
10	56
20	40
50	25
100	18
200	12
400	9
600	7
800	6
1000	5.6

Table 3.2. Sampling depths at different ΦM frequencies with $\alpha \cong 0.001$ cm^2/s

"extinction" angles (nodes) of selected bands from the phase rotation plot, qualitative results can be obtained. Mathematically, the phase rotation uses the simple vector algorithm:

$$e^{(i\alpha)}M(\sigma)e^{(i\theta)} = M(\sigma)e^{(i(\alpha+\theta))} = M(\sigma)cos(\alpha+\theta) + iM(\sigma)sin(\alpha+\theta) \quad (3\text{-}11)$$

where θ is the original "detection" phase angle and α is the phase angle used in the spectral (or interferogram) rotation. The new "in-phase" [M(σ)cos(α+θ)] and "quadrature" [M(σ)sin(α+θ)] spectra from the phase rotation enhance signals from different depths of the sample depending on the values of α. The third approach to depth profiling analysis using the phase data is to calculate the phase spectrum θ(σ) from the simultaneously collected in-phase and quadrature spectra by using Equation (3-8).[22,29-33,36] The phase difference obtained from the comparison of extinction angles in the continuous phase rotation plot method can be also obtained more directly and with less manipulation from the phase spectrum.

The measurement of the absolute PA phase is limited by the ability to reproduce the instrument phase from reference to sample. Nevertheless, the phase differences between different bands in a spectrum are highly reproducible.[22] For this reason, the phase difference ΔΦ has been made the focus of conceptually simple, general theoretical models, which are particularly applicable to discretely laminar materials with distinctive marker bands for each layer as mathematically described by Equations (3-6) and (3-7) for the two specific cases in **Section 3.3.3**. In the phase difference models, the relevant variables (thickness, optical absorptivity, thermal diffusivity, modulation frequency, etc.) are related to each other by the PA phase information. Thus quantitative determination of these physical parameters is also made possible through the use of the models and the S²ΦM FTIR PAS technique.[22, 33]

3.3.6 Step-scan phase modulation (S²ΦM) FTIR PAS: Experimental

PAS Reference. Since only the absorbed IR light generates thermal waves and contributes to PA detector signals, the PA single-beam spectrum is an uncorrected "absorption" spectrum of the sample. The variations over the spectral region in source intensity, beam splitter efficiency, and detector response must be corrected using a reference sample that absorbs strongly at all wavenumbers.

A common practice in both continuous- and step-scan PAS depth profiling is to use a strongly absorbing glassy carbon (or a highly concentrated carbon black-filled rubber, minimum carbon content 60%) as a reference. Since the reference absorbs strongly at all wavenumbers in the mid-IR region, its magnitude spectrum can be used as a reference to normalize PA spectra, correcting all those variations mentioned above. In addition, since almost all absorption occurs at the surface of the strong absorber, it can be used as a surface reference for calibrating the phase of a step-scan phase modulation depth profiling experiment.

When this reference is in place, the relative ΦM phase setting button, as shown in Figure 3.6, is pressed to maximize PA signals in the in-phase (I) channel and subsequently the quadrature (Q) channel is minimized. After this phase angle calibration is done, the ΦM phase setting will be kept unchanged for running a sample under the same modulation frequency. The resulting in-phase spectrum of the sample will therefore enhance the surface absorption features and the quadrature spectrum will enhance those from the substrate or deeper part of the sample.

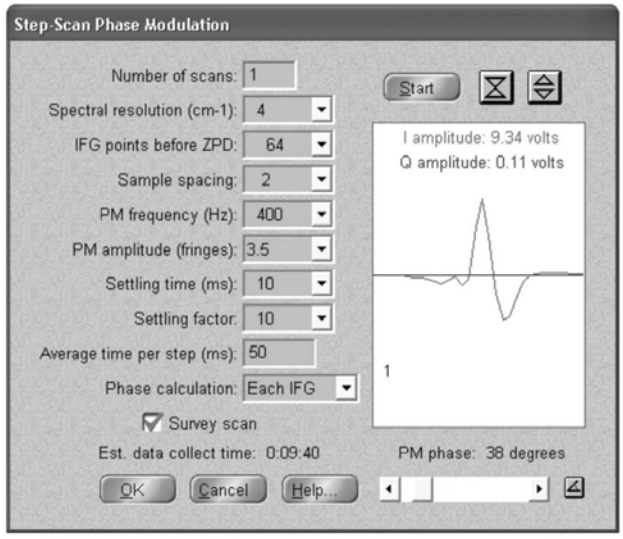

Figure 3.6. OMNIC SST setup screen for S²ΦM experiments.

Software Setup Screen. The OMNIC SST setup screen for a S²ΦM experiment is shown in Figure 3.6. All the S²ΦM related experimental parameters can be set in this window. The Start button allows a short setup scan (64 points around the ZPD or centerburst) using the setup parameters and displays the result in this window. The phase angle calibration button is located on the bottom right corner and must be pressed when the glassy carbon black reference is placed in the PA cell. This setup screen also allows users to adjust PA gain setting on top of the PA cell to optimize the signal before collecting data.

3.3.7 FTIR PA depth profiling examples

The theory, experimental, and spectral analysis approaches for FTIR PA depth profiling have been discussed in previous sections. In this section, applications of these approaches will be demonstrated in depth profiling analysis of some multilayered samples. Modulation frequency-resolved and phase-resolved S²ΦM FTIR PAS will be emphasized as they are presently the most popular approaches in practical applications. In addition, continuous-scan PAS will also be demonstrated as a very valuable diagnostic tool despite the ambiguity with spectral interpretation because of its simplicity and speed of data acquisition. By monitoring characteristic band intensity variation over a range of mirror velocities, it is also possible to achieve some useful spectral depth profiling results. A few other depth profiling approaches used in FTIR PAS, as reported in literature, such as time-resolved FTIR PAS,[36,38-39] 2D FTIR PAS[32, 36, 40] and PAS linearization[36, 41-43] are not covered in this chapter. Generalized 2D FTIR PAS will be briefly discussed in **Chapter 6**.

PMMA on ABS. This sample consists of a 0.9 μm layer of poly(methylmethacrylate) (PMMA) on a thicker layer of poly(acrylonitrile:butadiene:styrene) (ABS). Continuous-scan PAS spectra taken at a series of optical velocities (0.0158 – 0.63 cm/sec) are shown in Figure 3.7. It can be seen that at high optical velocities, modulation frequencies are high, the sampling depths are subsequently shallower, and therefore PAS spectra are dominated by the surface PMMA layer. The picture is reversed as the velocities and the corresponding modulation frequencies decrease. At low velocities, the sampling depth is deep and the

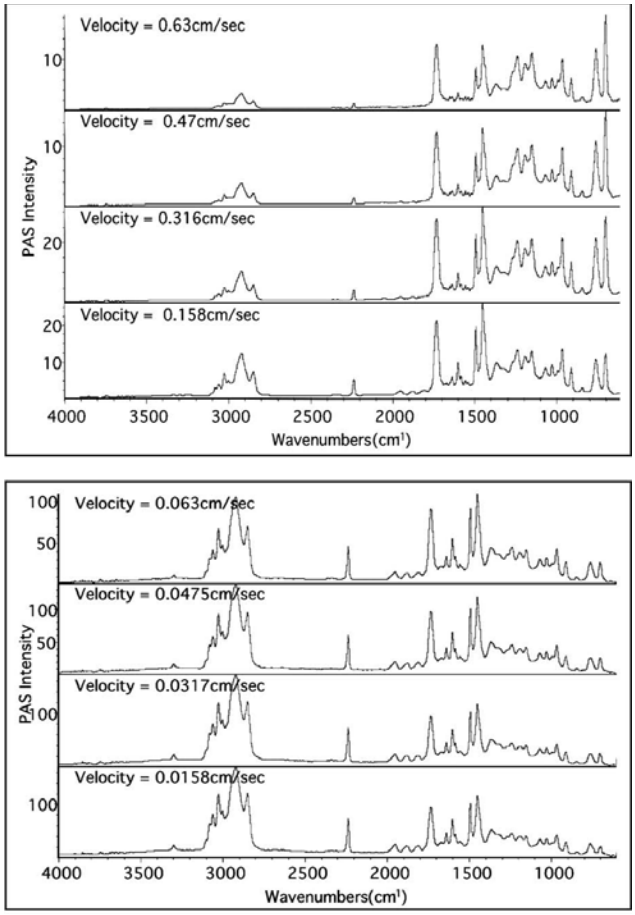

Figure 3.7. Continuous-scan PA spectra of PMMA on ABS at various optical velocities.

relative contribution from the thin surface layer is minor, thus the spectra are dominated by the bands of the bulk ABS layer.

The step-scan experiment on the same PMMA/ABS sample was conducted with a ΦM frequency of 1,000 Hz. A uniform probing depth of about 5.6 μm across the spectrum is expected from this measurement. Since ΦM calibration phase was set to maximize the surface absorption in the in-phase (I) channel, as shown in Figure 3.8, the I spectrum is dominated by spectral features of the surface layer PMMA, and subsequently minimal contribution of PMMA and maximum contribution of ABS can be found from the Q spectrum.

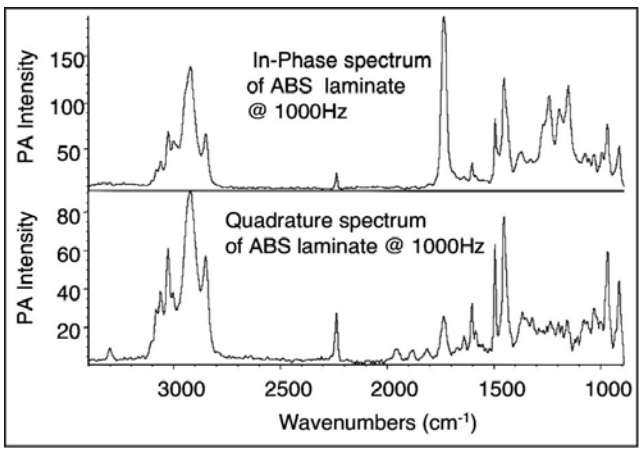

Figure 3.8. Comparison of I and Q spectra of PMMA/ABS collected at a phase modulation frequency of 1,000 Hz.

Kapton™ film. The three-layer Kapton film consists of a 50 μm polyimide layer sandwiched between two 12 μm Teflon® layers. Figure 3.9 shows frequency-resolved PA magnitude spectra of this sample collected in S^2ΦM mode at frequencies from 50 – 800 Hz. At 50 Hz, the probing depth is about 25 μm, thus polyimide bands over the spectral region of 1800 – 1350 cm^{-1} are clearly detected. As the modulation frequency increases to 800 Hz, the probing depth decreases to 6 μm and the spectrum only shows a broad Teflon band around 1225 cm^{-1} (CF stretch).

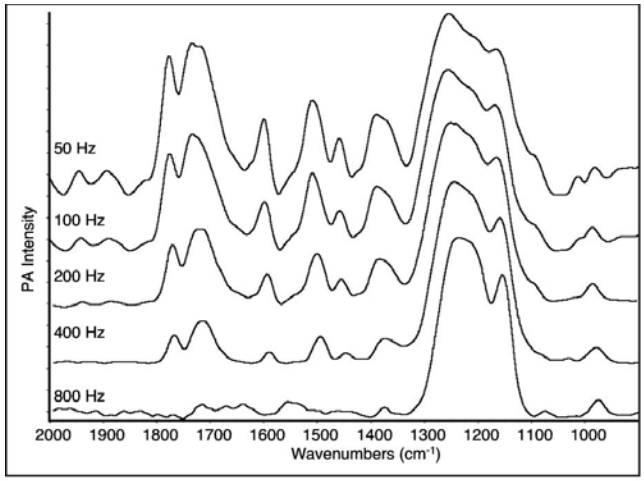

Figure 3.9. Step-scan frequency-resolved PA magnitude spectra of Kapton collected at phsde modulation frequencies from 50 - 800 Hz.

The I and Q spectra of the Kapton sample obtained with a ΦM frequency of 400 Hz are shown in Figure 3.10. The surface reference phase calibration was performed using the glassy carbon as described earlier. It can be seen that the I spectrum contains contributions mainly from the top Teflon layer and Q spectrum contains contributions mainly from the intermediate polyimide layer.

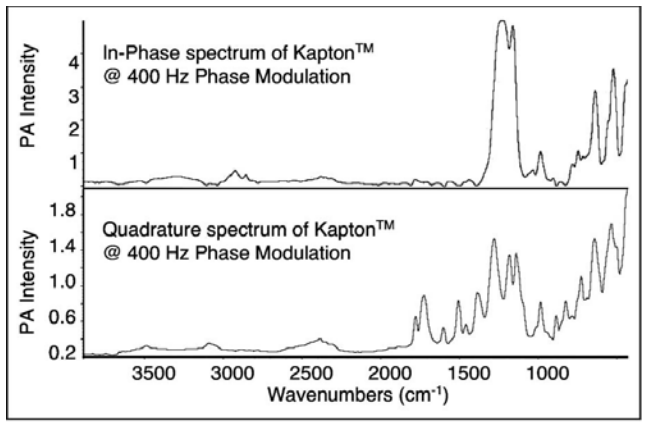

Figure 3.10. Normalized I and Q spectra of Kapton film collected at a ΦM frequency of 400 Hz.

The PA spectra of the Kapton film over a 180° range of phase angles are calculated and displayed using the OMNIC SST phase rotation and 3D display routine and the results are shown in Figure 3.11. As the phase rotation angle increases from 0 to 90°, the spectral features associated with the deeper polyimide layer replace those from the surface Teflon layer.

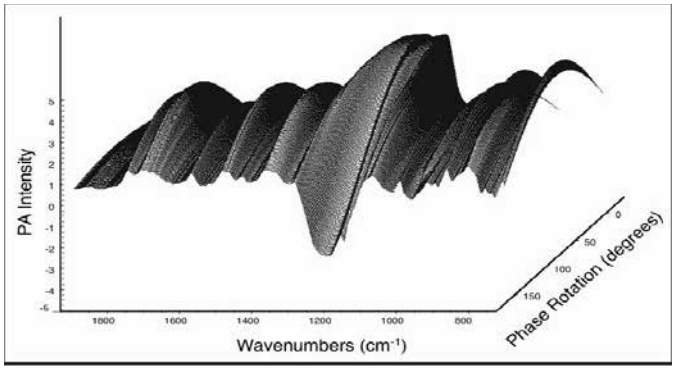

Figure 3.11. Phase rotation 3D view of PA spectra of Kapton collected at a phase modulation frequency of 400 Hz.

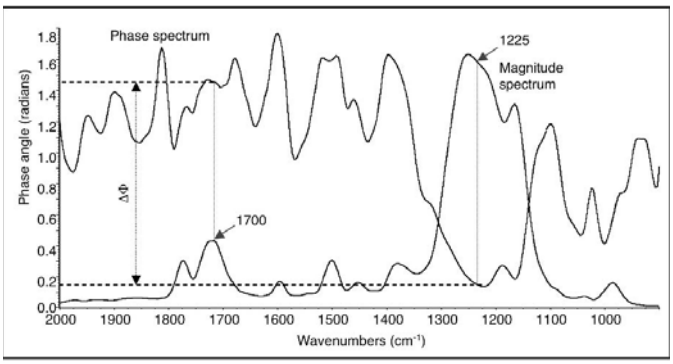

Figure 3.12. PA magnitude and phase spectra of Kapton film collected at a ΦM frequency of 400 Hz.

As discussed earlier, the phase spectra can be used directly for both qualitative and quantitative analysis. Figure 3.12 shows both the magnitude and phase spectra of the Kapton sample collected at a ΦM frequency of 400 Hz. The phase angles at all bands on the magnitude spectrum can be read directly from the phase spectrum. It can be seen that the Teflon band at 1225 cm^{-1} has the smallest phase lag whereas all polyimide bands between 1800 – 1350 cm^{-1} have much larger phase lags. Among these polyimide bands, the strongest one at 1700 cm^{-1} has the smallest phase lag, thus it is a more "surface" representative for the polyimide layer. By using a simplified version of Equation (3-6), the thickness of the top layer can be calculated as follows:

$$d_{(Teflon)} = \Delta\Phi_{(1700-1225)}\mu_{(400Hz)} = (1.475 - 0.150)8.08\mu m = 10.71\mu m$$

In this calculation, the thermal diffusivity of the Teflon layer, α = 0.82 x 10^3 cm^2/sec,[44] was used in Equation (3-2) to determine µ400Hz. This result is in close agreement with the real thickness of 12 µm for the Teflon layer.

PMMA on PS on PP. An important advantage of using PA signal phase in depth profiling is the enhancement of spatial resolution (as high as on the submicron level, beating the IR diffraction limit) within a given probing depth defined by the modulation frequency and material properties. Figure 3.13 illustrates the PA magnitude (top) and phase spectrum (bottom) of a three-layer sample: 0.5 µm poly(methyl methacrylate) (PMMA), on 0.5 µm polystyrene (PS), on 2 mm polypropylene (PP), collected at a ΦM frequency of 200 Hz and amplitude of 3.5 λHeNe. The phase spectrum, as shown in Figure 3.13, clearly distinguishes characteristic bands from different layers by phase angle. The relative phase lags of 0.1°, 3° and 18° correspond to distinctive bands of PMMA (1727 cm^{-1}, C=O stretch), PS (748 cm^{-1}, aromatic CH deformation) and PP (1376 cm^{-1}, CH deformation), respectively. In addition, the top two layers agree with the phase difference model for thermally thin or optically transparent layers,[22] as shown by Equation (3-6). Thus the thickness of the PMMA layer, dPMMA, can then be also determined by the phase difference model:

$$d_{(PMMA)} = \Delta\Phi_{(1727-1370)}\mu_{(200Hz)} = (3 - 0.1)(p/180)x12.7 = 0.6\mu m$$

Again, this result is very close to the actual thickness of about 0.5 µm. The ability of PAS to discriminate between submicron layers using the phase information is clearly demonstrated. This detection capability is certainly beyond the diffraction limit encountered in IR microscopy.

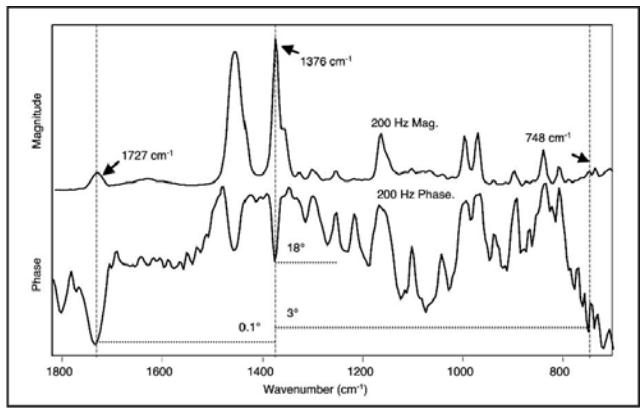

Figure 3.13. S²FTIR magnitude and phase spectra at a ΦM frequency of 200 Hz. fro a three-layer sample PMMA/PS/PP, the top two layers of which are sub-micron thick.

3.4 Photoacoustic spectroscopy saturation correction

3.4.1 Introduction

One of the complications that occurs in infrared photoacoustic spectroscopy for depth profiling analysis, for both continuous-scan and step-scan operation, is saturation of the photoacoustic signal for strongly absorbing bands. A correction for photoacoustic saturation has been developed by Jones and McClelland[45], who extended Rosencwaig and Gersho's expression for the photoacoustic signal[19] to correct the signal for saturation effects, and their method will be summarized here.

The photoacoustic signal is considered to be saturated when the signal intensity loses its dependence on the sample absorption coefficient, β, but in PAS the signal intensity is also dependent on the sampling depth, µ. For homogeneous thermally thick samples, the PA signal intensity is proportional to βµ2 for µ<1/β. When µ>1/β the signal saturates and it becomes proportional to µ and loses its dependence on β. Saturation of the photoacoustic signal occurs for homogeneous samples as µ approaches 1/β, and also since β varies from peak to peak, different peaks show different levels of saturation as the modulation frequency or mirror velocity is decreased. Even qualitative interpretation of a set of spectra with different mirror velocities will thus be difficult.

3.4.2 PAS saturation correction method

The mathematical solution that has been developed to determine the depth profile from a set of photoacoustic spectra is considered to be ill conditioned, meaning that the result is highly sensitive to small errors in the initial data. The method that will be described below avoids the ill conditioned problem by making use of a priori knowledge of the sample structure to limit the

depth profile solutions. This method reduces the level of saturation in a low mirror velocity spectrum to that in a reference high mirror velocity spectrum, where the level of PA signal saturation is non-existent or very low. The method uses only magnitude spectra, so it is equally applicable to a set of spectra collected in continuous scan or step-scan phase modulation ($S^2\Phi M$) PAS. The method develops a band intensity scaling factor, Q_{sc} , based on a peak height ratio, R_n, between a low speed and high speed normalized spectra from a peak representative of a homogeneous component in the sample.

Q_{sc} and R_n are related to each other by

$$R_n = 1/\left[N^{(1/2)} + Q_{sc}\left(1 - N^{(1/2)}\right)\right] \quad \text{(3-12)}$$

and

$$Q_{sc} = \left(N^{(1/2)}R_n - 1\right)/\left[R_n\left(N^{(1/2)} - 1\right)\right] \quad \text{(3-13)}$$

where N is the ratio of scan speeds between the high speed and low speed spectra. R_n and Q_{sc} are vectors having both magnitude and phase. However, only the magnitudes of these vectors can be obtained from magnitude PAS spectra, and the magnitude of Equations (3-12) and (3-13) can be obtained from

$$R_n = 1/\left[N + 2N^{(1/2)}\left(1 - N^{(1/2)}\right)q_r + \left(1 - N^{(1/2)}\right)^2 Q_{sc}^2\right]^{(1/2)} \quad \text{(3-14)}$$

$$Q_{sc} = \left[NR_n^2 - 2N^{(1/2)}\left(1 - N^{(1/2)}\right)\rho_r + 1\right]^{(1/2)}/\left[R_n\left(N^{(1/2)} - 1\right)\right] \quad \text{(3-15)}$$

where q_r and ρ_r are the real components of vectors Q_{sc} and R_n, respectively.

3.4.3 PAS saturation correction examples

The procedure to correct a low-speed spectrum for photoacoustic saturation is demonstrated with the spectra displayed in Figure 3.14, for a thermally thick layer of poly methyl methacrylate (PMMA).

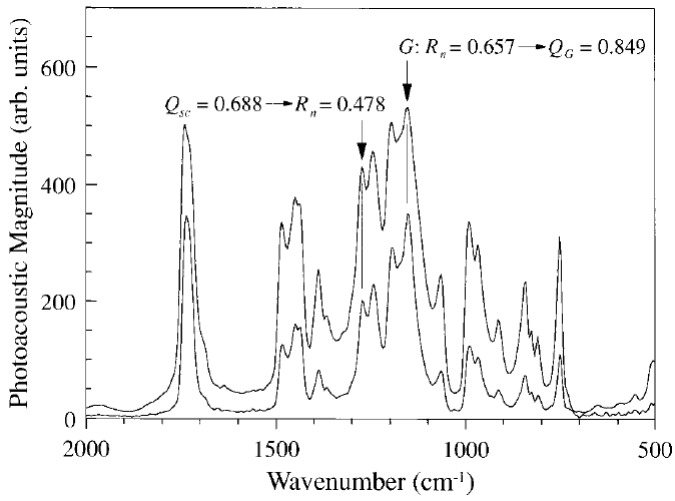

Figure 3.14. Spectra of a thick sample of PMMA taken at mirror velocities of 0.1565 cm/sec (top) and 2.532 cm/sec (bottom). respectively, and the conversion-parameter values for the guide peak, G, and an example peak. *Example courtesy of Jones and McClelland[45], with permission.*

A guide peak, G, is selected in the spectrum for a homogeneous component, and the peak height ratio between the low speed and high-speed spectrum for that band, R_n, is used to calculate QG for that band from Equation (3-15). With the spectra displayed in Figure 3.14, the ratio of scan speeds between the high speed and low speed spectra, N, is 16, and the peak at 1153 cm^{-1} has been selected as the guide peak, G. The peak height ratio for that peak is 0.657, determining the value R for that peak, from which QG can be calculated from Equation (3-15) with a value of 0.849.

With QG now known, the scaling for the rest of the spectrum is simple because the scaling is linear with the scaling factor QG/hr. For a point in the low-speed spectrum with a value Y, so that it is y times the value of peak G, its value can then be expressed as yQG in the scaled spectrum; Qsc = yQG = YQG/hl for that point. If we select the peak at 1273 cm^{-1}, its magnitude is 81% of the magnitude of peak G, leading to a value Q_{sc} for that peak of 0.688, which allows R_n for that point to be calculated from Equation (3-14). The whole spectrum is scaled in this manner determining a set of Q_{sc} values, which allows the value R_n to be calculated for each point. The high-speed equivalent spectrum is then produced by multiplying each point in the original low-speed spectrum by the array of values R_n for that spectrum.

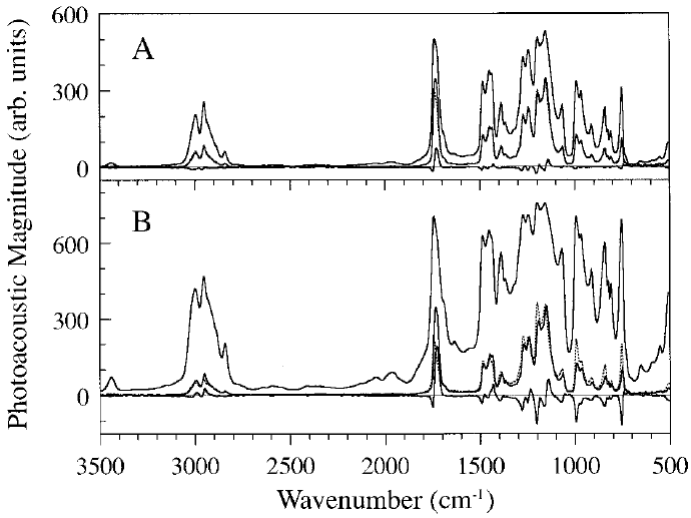

Figure 3.15. Conversion of two low-speed spectra of PMMA to high-speed equivalents. (A) The 0.1565 and 2.532 cm/sec spectra from Figure 3-14, the 0.1565 cm/sec spectrum after conversion to 2.532 cm/sec equivalence (dotted line), and the difference spectrum between the true 2.532 cm/sec spectrum and the 2.532 cm/sec equivalent spectrum. (B) As in A, except using starting spectra at 0.0127 cm/sec and 2.532 cm/sec. *Example courtesy of Jones and McClelland[45], with permission.*

The result of the saturation correction is demonstrated in Figure 3.15. The two original spectra from Figure 3.14 are shown in panel A, along with the high-speed equivalent of the low-speed spectrum (dotted line), and the difference (error) between the high-speed equivalent and original high-speed spectrum. Since this sample is homogeneous, the high-speed equivalent spectrum should be identical to the high-speed spectrum, which is nearly true in this case since the dotted line spectrum is difficult to distinguish from the true high-speed spectrum, and the difference spectrum is very low. The difference spectra in Figure 3.15 show two types of errors in the correction; the carbonyl band at 1736 cm^{-1} is under-corrected, leaving a small positive residual peak in difference spectrum, and the errors have a derivative-like shape, indicating a band shift in the

low-speed spectrum compared to the high-speed spectrum. As the amount of saturation grows in the low-speed spectrum, the apparent peak positions shift to higher wavenumber. This effect is exacerbated in the lower set of spectra in Figure 3.15, where low-speed spectrum scan speed is 200 times lower than the high-speed spectrum.

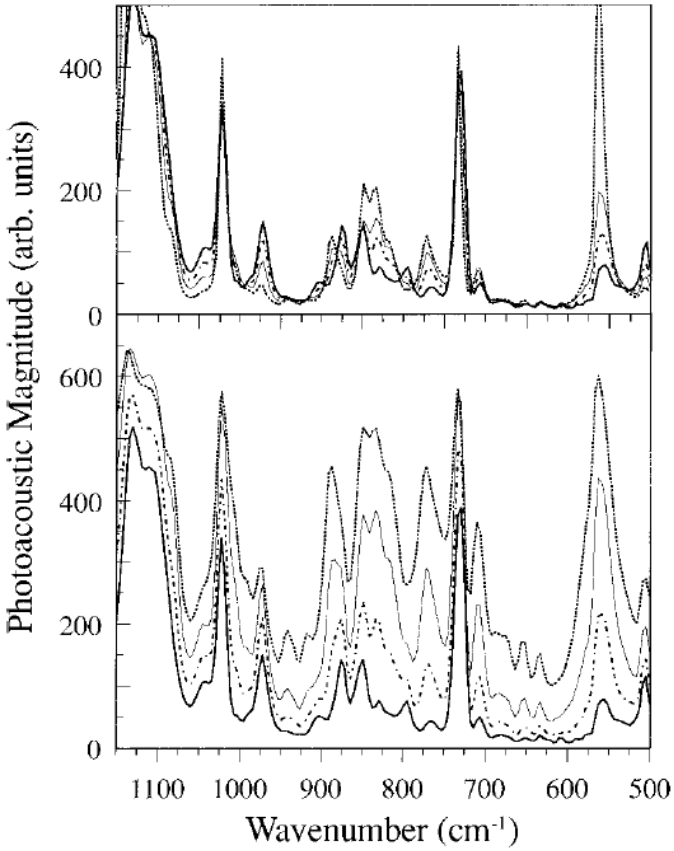

Figure 3.16. Spectra of a sample consisting of a 6-µm layer of PET on a thick polycarbonate substrate taken at 2.532 cm/sec (thick line), 0.6330 cm/sec (dot-dash line), 0.1565 cm/sec (thick line), and 0.0253 cm/sec (dotted line). Lower panel; spectra as acquired. Upper panel; the same spectra as in the lower panel after conversion to 2.532 cm/sec equivalence.
Example courtesy of Jones and McClelland[45], with permission.

Jones and McClelland extended this treatment to a laminated film sample, consisting of 6 µm of poly ethylene terephthalate (PET) on a 1.7 mm thick polycarbonate (PC) substrate, as shown in Figure 3.16. The bottom panel shows normalized photoacoustic spectra acquired at scanning speeds of 2.532 cm/sec (thick solid line), 0.6330 cm/sec (dot-dash line), 0.1565 cm/sec (thin solid line), and 0.0253 cm/sec (dotted line). The raw original spectra generally show increasing peak intensity as the scan speed is lowered, indicating deeper penetration into the sample, past the PET layer into the PC substrate, but quantitative comparison is difficult because of increasing saturation of the peak intensities in the slower scan speeds.

Speed conversion allows for a better qualitative comparison of the spectra, with each peak showing its own trend as a function of sampling depth. The strongest bands in the 2.532 cm/sec spectra (730, 1020, and 1130 cm^{-1}) change only a little after high-speed conversion, indicating that they are due to strongly absorbing PET bands and almost all of the infrared beam intensity is absorbed in the PET layer at those frequencies. The peak at 560 cm^{-1} is over-corrected in the high-speed conversion, especially at the lowest scanning speeds. This band is due to the PC substrate. The speed correction algorithm properly corrects for the growth of peaks in a homogeneous sample, but it can distort strong peaks whose growth is due to sample structure. This is why it is important that an a priori knowledge of the sample structure is known for proper application of this method. The reader is referred to Jones and McClelland's paper[45] for a detailed development and explanation of the method, and additional examples of its use.

3.4.4 Attaching the photoacoustic saturation correction DDE command to an OMNIC menu

The Photoacoustic Saturation Correction method described here is available in OMNIC as a DDE command, but it may be more convenient for the user to attach the command to an OMNIC menu. The procedure to attach a DDE command to a menu is as follows:

1. In OMNIC, click on Edit, then select Edit Menu, as shown below.

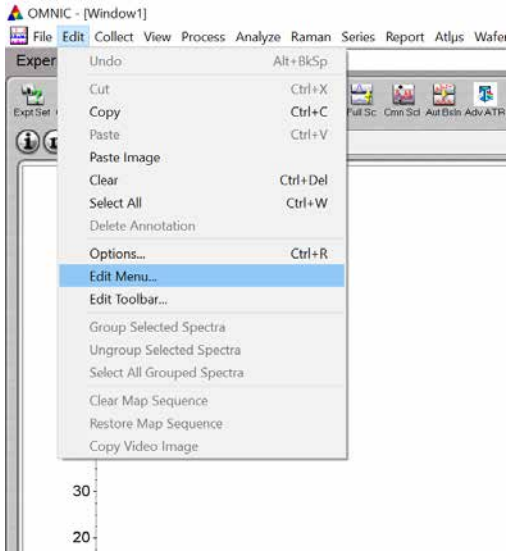

2. In the Edit Menu dialog, click on Add Item, and a Menu Item dialog appears.

3. Select the menu item to which the command will be attached in the Menu pull down box, the text for the menu as it will appear in the menu in the Menu text box, and the name of the DDE command, which in this case is *PASSaturationCorrection*.

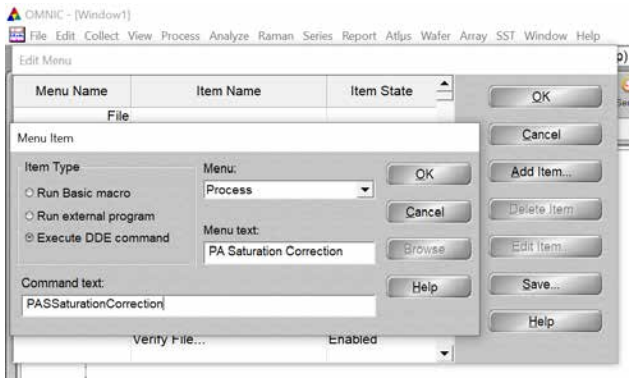

In this example, the command will be attached to the Process Menu item and the menu text will be PA Saturation Correction.

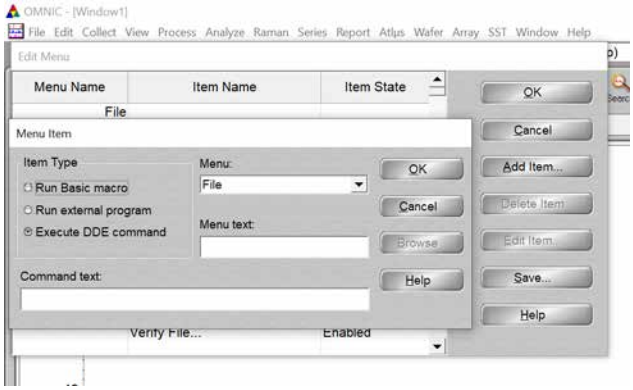

4. Click on OK, and the item PA Saturation Correction will be added to the bottom of the Process menu items.

To use the command, first select the low-speed spectrum in OMNIC for processing, then select the PA Saturation Correction item from the Process menu. A dialog box will appear with an entry for the wavenumber of the guide band, and an option for a local baseline point if baseline correction is desired. After this entry a dialog box will appear to select the reference high-speed spectrum. After its selection, the corrected spectrum will be displayed with the original low-speed spectrum for comparison.

Chapter 4:
Step-scan Time-resolved FTIR Spectroscopy (S^2TRS)

4.1 Introduction

Step-scan time-resolved FTIR spectroscopy (S^2TRS) is well suited to obtain spectral and kinetic information on fast, repeatable chemical reactions or physical processes with time resolutions from microseconds to nanoseconds. In S^2TRS, data are collected as an explicit function of time at each mirror position when both mirrors are stopped completely, as illustrated in Figure 1.4 in **Chapter 1**. This time profile is repeated and recorded at all mirror positions. After the experiment finishes, the data are sorted into individual interferograms which are then Fourier transformed into IR spectra at different times. The meaningful time resolution of step-scan TRS is determined by both the speed of the digitizer and the rise time of the detector, rather than by the scanning (stepping) speed.

Multiple triggers and coadditions at each mirror step with data collection are often used to improve signal-to-noise ratio. The S^2TRS spectrometer can be operated either in master (where the spectrometer triggers the excitation system of the sample) or slave operation mode (where the excitation system is used to trigger the digitizer of the spectrometer). An external perturbation-induced reversible or repeatable system can be readily studied by S^2TRS.

The repeatable reactions or processes are often initiated with an external perturbation that varies in different application areas. The most common perturbations include the following:

- Electrical perturbation.[46] electric pulses used in studying materials such as liquid crystals and light emitting devices (LED's).
- Optical perturbation.[47-49] laser or flash lamp pulses used in photochemical reaction studies such as excited states of metal complexes, photochemical reactions in condensed or gaseous phase, and biophysics such as photocycles of bacteriorhodopsin;
- Thermal perturbation.[50-52] temperature jump used in biochemical and biophysical studies (protein conformational changes).
- Irreversible systems can be also investigated by S^2TRS if the process can be regenerated by repetitively providing fresh sample into the beam for each mirror position (step) with a stop-and-flow cell5[3-54] or motorized stage.[55]

The dynamically aligned, DSP-controlled, highly integrated, research-grade iS50R FTIR spectrometers with mirror positioning control better than ±0.2 nm are virtually immune to acoustic noise and environmental vibrations and are easy to interface with external devices such as lasers and pulse generators, ensuring reliable performance for highly demanding TRS applications.

4.2 S^2TRS data collection and process

The timing scheme for step-scan TRS data collection are illustrated in Figures 4.1 and 4.2 for master and slave operation modes respectively. Both figures show details of mirror stepping, mirror settling, static sampling, trigger signal and dynamic time-resolved sampling. The sequence of a typical step-scan TRS experiment in master operation mode includes the following steps:

1. The moving mirror of the interferometer steps to a predetermined position and then holds stationary to settle down and stabilize for the amount of time set by Settling Time.
2. The static interferogram is recorded from the DC output of the detector preamplifier. The signal is averaged over the amount of time set by Static Average Time.
3. A synchronized TTL pulse is provided as a trigger signal for the external excitation source such as a laser or a pulse generator that initiates the time-dependent process under study.
4. The AC output from the preamplifier of the detector measures the change in spectral intensity. The dynamic interferograms are collected over a given period of time at intervals set by users. Data are averaged in multiple trigger mode for each mirror step to improve SNR.
5. The moving mirror then travels to the next position and the above steps are repeated.
6. Finally, interferogram data files are reconstructed along the time scale.

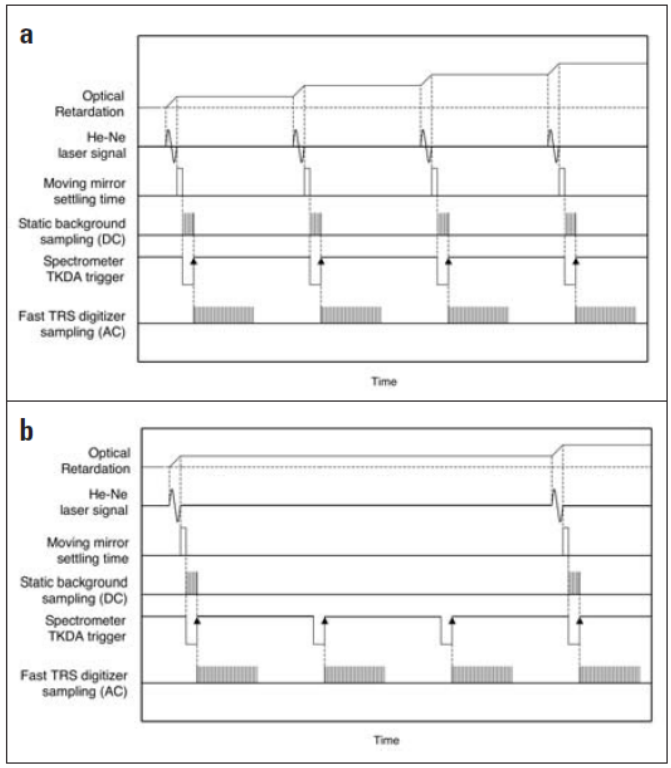

Figure 4.1. Schematics of time sequence for S^2TRS master operation mode in which the digitizer trigger input is from the spectrometer internal clock:
a) Time sequence for experiments with single trigger per mirror step;
b) Time sequence for experiments with 3 triggers per mirror step.

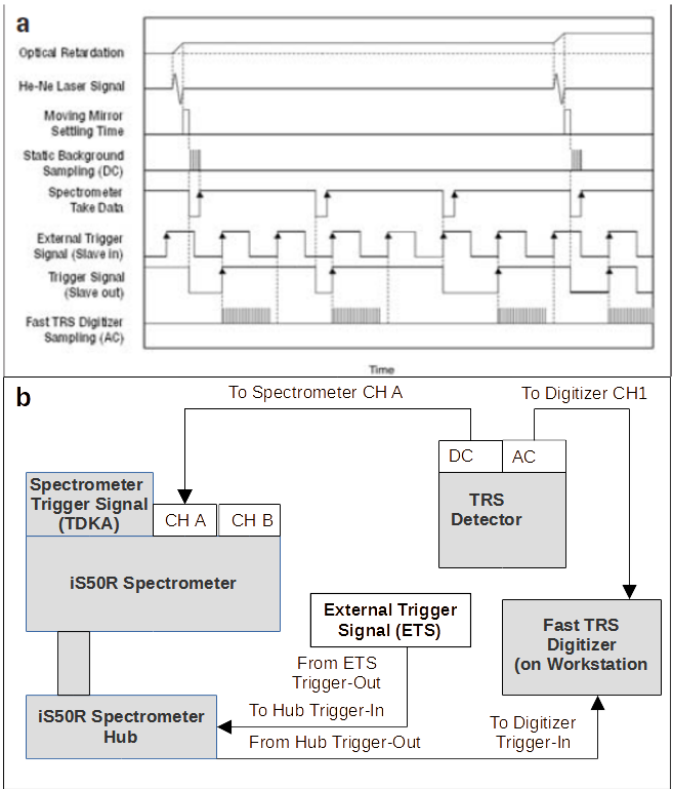

Figure 4.2. Schematics of time sequence and electronic diagram for step-scan TRS slave operation mode in which the trigger signal is from an external "pulse generator" or an equivalent. a) Time sequence for experiments with multiple triggers per mirror step, which indicates that only the first rising edge of an external trigger after the spectrometer TKDA signal triggers the fast TRS digitizer; b) Block diagram showing connections for trigger and detector signals.

In the spectrometer slave operation mode, an external perturbation / excitation pulse is used to trigger the TRS digitizer via the spectrometer remote signal accessory, as shown in Figure 4.2. Other time sequences in the TRS slave mode are similar to those of the master operation mode. The relationship between optical retardation, time, and detector signal intensity is illustrated in Figure 4.3.

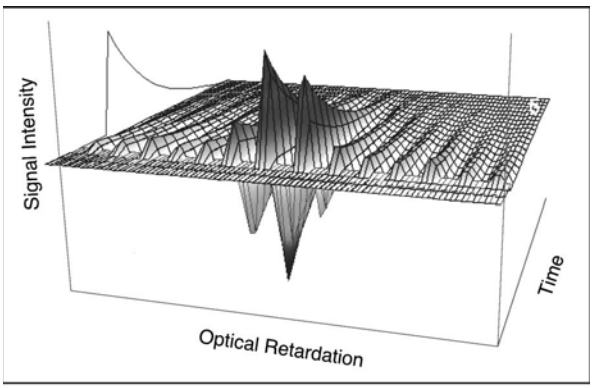

Figure 4.3. Schematic of optical retardation, time resolution, and detector signal intensity in S²TRS.

The S²TRS Static Interferogram is similar to the conventional continuous-scan interferogram. Fourier transformation of this interferogram gives the reference single-beam spectrum and the phase array. This phase array is used in the Fourier transform of Dynamic AC Interferograms to produce dynamic single-beam spectra. The absorbance difference spectra can be then obtained by normalizing dynamic spectra over the reference spectrum. The Research OMNIC software allows differential absorbance spectra as direct output of a S²TRS experiment if parameters are set properly prior to the experiments. The differential absorbance spectra are calculated based on Equation (4-1):

$$\Delta A = A_{(AC+DC)} - A_{(DC)} = -log_{(10)}\left(1 + \Delta I_{(AC)}/I_{(DC)}\right) \quad (4\text{-}1)$$

where I_{DC} and ΔI_{AC} are single-beam intensity spectra corresponding to static (DC) and dynamic (AC) channels. When a different gain is applied to the AC channel, ΔI_{AC} must be calibrated before being used in Equation (4-1). This calibration can be conveniently done by using OMNIC TRS factor setting in the OMNIC32.ini file where the TRS factor = g_{DC}/g_{AC}.*

4.3 S²TRS options on research-grade iS50R FTIR spectrometers

Research-grade iS50R FTIR spectrometers offer TRS measurements on different time scales, with two different digitizers. The standard 1 MHz digitizer in the iS50R is an inexpensive option for monitoring repeatable processes slower than 1µs. An optional 200 MHz (5 nsec) digitizer can be installed externally on the workstation and used for more demanding TRS experiments with time. TRS detector options for the research-grade iS50R FTIR spectrometer are listed in Table 4.1.

Detector	Detector Element Size	Bandwidth	Preamplifier Output
Photovoltaic TRS MCT	0.5 x 0.5 mm2	50 MHz	DC/AC
Photovoltaic TRS MCT	1 x 1 mm2	20 MHz	DC/AC
Photoconductive TRS MCT	1 x 1 mm2	175 kHz	DC/AC
Photovoltaic TRS InSb	2 x 2 mm2	25 MHz	DC/AC

Table 4.1. TRS Detector options on the research-grade iS50R FTIR Spectrometer

The photovoltaic TRS MCT and InSb detectors are used for fast TRS experiments over the mid-IR and near-IR ranges respectively. The Photoconductive TRS MCT is used for relatively slower processes and is often coupled with a standard 1 MHz (1 µs) internal TRS digitizer.

The maximum achievable time resolution for a measurement is determined by the slower of the detector rise time and the digitizer time resolution. Detector rise time is considered to be the time it takes for a detector to respond from 10% to 90% of the signal level for a step function input, and can be estimated from the detector bandwidth as:

$$\tau_r = 0.35/f_{(bandwidth)}$$

For example, the photoconductive MCT detector has a bandwidth of 175 kHz, leading to rise time of 2 µs, and an achievable time resolution 2 µs when combined with the internal 1 MHz (1 µs) digitizer. For faster operation, the rise time of the 50 MHz photovoltaic MCT has a rise time of 7 nsec, and the detector will be the limiting component when combined with the optional 200 MHz (5 nsec) digitizer.

*Note: newer versions of OMNIC™ may have incorporated the TRS factor on the TRS setup screen.

4.4 Application of S²TRS

4.4.1 Introduction

The applications of S²TRS have expanded into many fields over the last decade particularly due to the availability of commercial step-scan systems. Active research work using S²TRS has been conducted in fields of photochemistry, material science, biology and biophysics and so forth. These studies have covered a wide range of systems where S²TRS provides a key solution to understanding the kinetic mechanisms.

Listed below are a few specific systems that have been studied by S²TRS:

1. Kinetics of excited states of metal complexes[56-58]
2. Photochemical reactions in condensed or gaseous phase;[49, 59]
3. Liquid crystals and polymerdispersed liquid crystals[45, 60]
4. Protein conformational changes induced photochemically or by temperature-jump[51-52,61]
5. Photocycles of bacteriorhodopsin[62-64]

A few representative examples are reviewed in this chapter to illustrate various aspects of the TRS technique and the performance of the research-grade Thermo Scientific FTIR spectrometers.

4.4.2 Photochemical reactions of trans[CpMo(CO)$_3$]$_2$.

The examples chosen here illustrate the utility of step-scan TRS as a technique for both spectral and kinetic studies on nanosecond or longer time scales. The first example is on the photochemical reactions of transcyclopentadienyl molybdenum tricarbonyl, i.e. trans[CpMo(CO)$_3$]$_2$ (Cp = cyclopentadienyl) in supercritical CO_2 fluid at 35°C.

The reaction schemes are shown below:

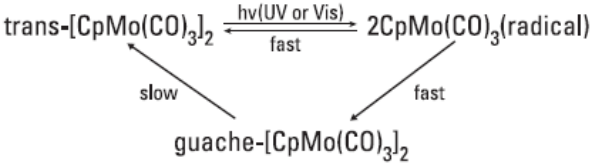

Irradiation of the sample solution with a laser pulse (532 nm, 10 ns pulse width) causes a dissociation of the dimeric trans[CpMo(CO)3]2 into two monomeric radicals, 2CpMo(CO)3, which then undergo recombination to form either the trans- or gauche-isomers. The gauche-isomer is less stable and will isomerize back to the more stable trans-isomer on a slower time scale.

A 3D stack plot of TR differential absorbance spectra of this sample over a 40 µs time window are shown in Figure 4.4. This set of data was collected with a total data collection time of < 2 hrs. The time resolution (time interval between two adjacent spectra) is 500 ns. These TRS spectra contain both spectral and kinetic information through the course of the reaction. A spectrum at a given time gives the structural information about the chemical species at that time. The kinetic plot of a given band shows the time evolution of the species associated with that particular band from which the rate constants of the reactions can be calculated.

Figure 4.5 shows the time-resolved spectrum at 500 ns after the laser pulse and the kinetic plot of the free radical CpMo(CO)$_3$. The TR spectra with a time resolution of 500 ns capture the early time evolution of the system after laser excitation. The slower isomerization can be measured over a longer time scale of 2 ms as shown in Figure 4.6.

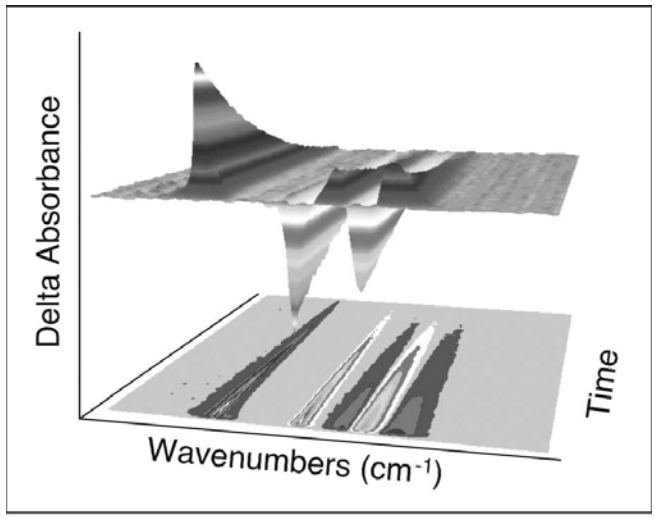

Figure 4.4. 3D stack plot of TRS spectra (differential absorbance spectra) over 40 µs time for photochemical reactions of trans-[CpMo(CO)$_3$]$_2$. *Data courtesy of Michael George of the University of Nottingham, UK.*

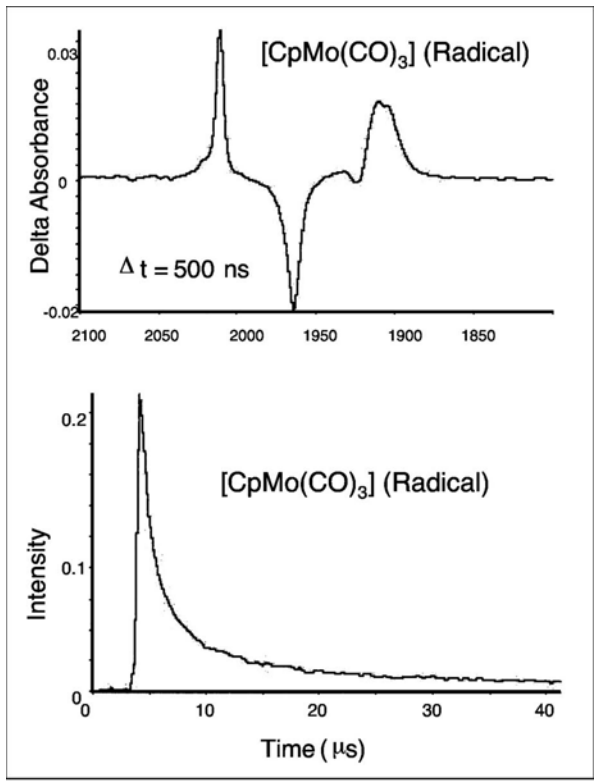

Figure 4.5. TR spectrum for the free radical [CpMo(CO)$_3$] measured at 500 ns after the laser pulse (top) and kinetic plot of the IR band intensity at 2011 cm^{-1} over the 40 µs time evolution of the free radical (bottom). *Data courtesy of Michael George of the University of Nottingham, UK.*

Fast Kinetics of W(CO)5(Xe). TRS measurement on nanosecond (ns) time scales has also been successfully conducted on a research-grade Thermo Scientific FTIR spectrometer. As illustrated in Figure 4.7, W(CO)5(Xe) was generated in situ from W(CO)6 by a 308 nm laser pulse in a supercritical Xe and CO solution49 at room temperature. The lifetime of this reaction is ~100 ns, thus the spectra can be measured by FTIR only in step-scan mode. The difference

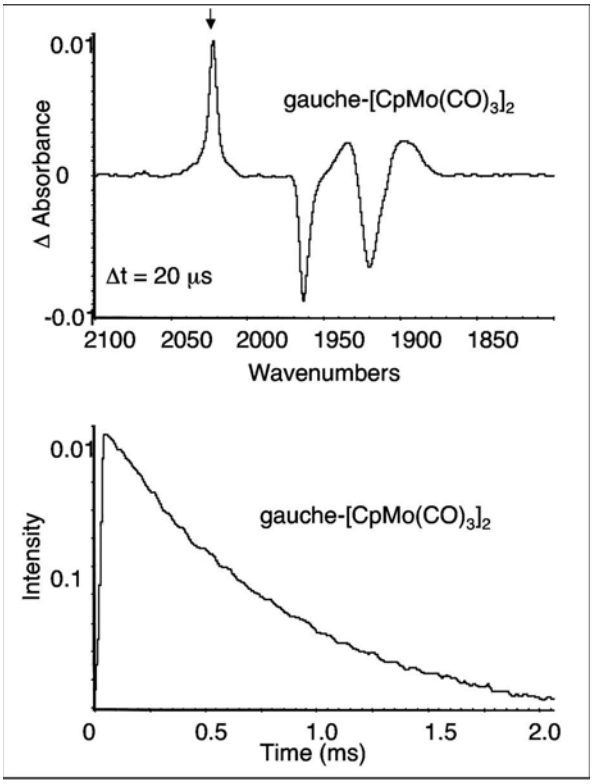

Figure 4.6. TR spectrum for the gauche-isomer, measured at 20 μs after the laser pulse (top) and kinetic plot of the IR band intensity at 2022 cm^{-1} over the first 2 ms time window (bottom) for the process of the trans- to the gauche-isomerization. *Data courtesy of Michael George of the University of Nottingham, UK.*

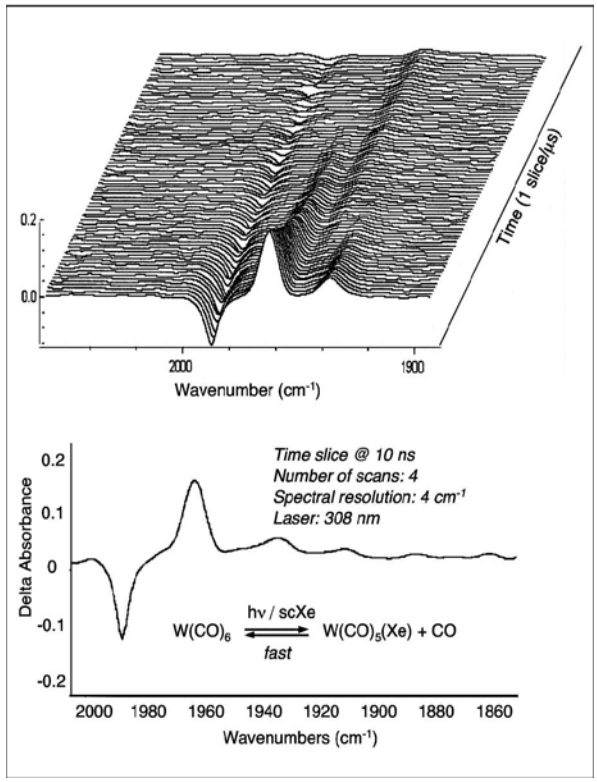

Figure 4.7. Absorbance difference spectra for time resolution of 10 ns (bottom) and 500 ns (top) of $W(CO)_5Xe$ generated in situ from $W(CO)_6$ in supercritical Xe/CO solutions. *Data courtesy of Michael George of the University of Nottingham, UK.*

spectrum is a 10 ns time slice of the TRS spectra from a 4-scan data collection, clearly indicating a decrease and increase in concentration of the reactant and product, respectively.

$$W(CO)_6 \underset{}{\overset{h\nu/scXe}{\rightleftharpoons}} W(CO)_5(Xe) + CO$$

4.4.3 Liquid Crystal Dynamics

Liquid crystal (LC) dynamics can be studied by using either the sample modulation technique where an alternating electric field is the source of perturbation, or TRS where molecular responses to the change of electric field can be monitored over time. In the sample modulation LC experiment, ideally an instantly responding reference sample should be used to set the experimental phases. In TRS LC experiment, such reference is not required as the sequence of events is recorded precisely as a function of time. As its name implies, LC's possess some of the characteristics of both liquids (mobility) and crystals (molecular orientations). A typical molecular structure of a LC contains a rigid part and a long flexible tail such as 4cyano4pentylbiphenyl (5CB) shown below:

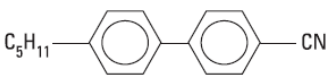

LC molecules align themselves along the appropriately treated electrode surfaces. A typical LC cell structure is shown in Figure 4.8. The sample preparation follows these procedures: 1) Apply 0.1% aqueous PVA solution to the Ge windows; 2) Rub residual PVA in a uniaxial direction; 3) Place and align Ge windows face to face; and 4) Inject LC sample from the top gap between the two windows spaced by the Teflon.

The orientation of the LC changes when an electric field is applied across the material. This is the basis for LC displays used in devices such as watches, cars, and notebook computers, and flat screen TVs.

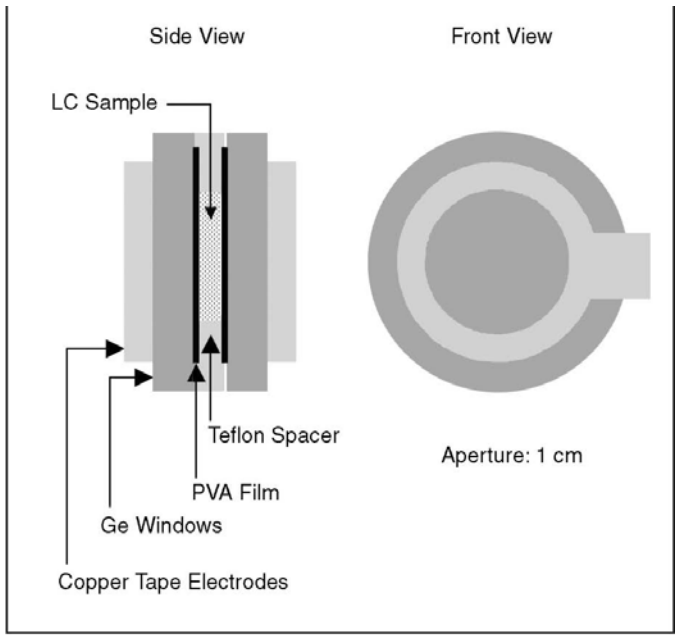

Figure 4.8. Schematic of an LC cell with its major components: two circular Ge windows (25 mm x 2 mm, diamter x thickness), two teflon spacers (10 μm thickness), and copper tape electrode rings.

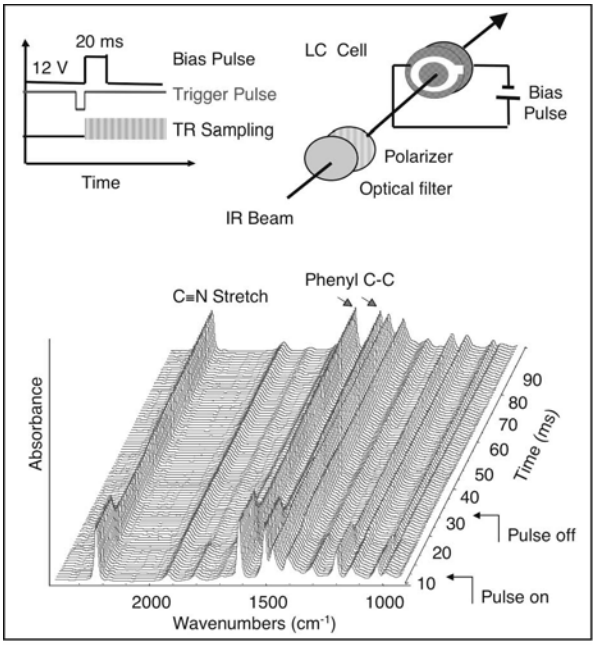

Figure 4.9. Experimental setup for LC TRS and representative TRS data of 5-CB.

Studies of the reorientation dynamics of LCs were among the first step-scan TRS applications because of the ability to monitor the reorientation dynamics of different parts of the molecule. For most nematic LCs, the molecular orientation change (switching) typically occurs on millisecond (ms) time scales. The actual dynamics depends on the experimental conditions such as the strength of the electric field, sample thickness, and temperature. For some ferroelectric LC's, the dynamics can occur on the microsecond time scale. As stated earlier, these relatively slow experiments that occur on ms to μs time scales can be conducted with the internal digitizer of the spectrometer. The time sequence, experimental setup, and some TRS data for 5CB are presented in Figure 4.9.

Chapter 5:
Polarization Modulation FTIR Spectroscopy

5.1 Introduction

Polarized IR spectroscopy provides a means to study molecular orientations and chiro-optical properties. Static polarized IR spectroscopy has been utilized to determine molecular orientations of polymeric materials in vibrational linear dichroic (VLD) measurements, as well as those of thin films on reflective surfaces in infrared reflection absorption spectroscopic measurements (IRRAS). In the static measurement, the dichroic difference is obtained from sequentially recorded absorbance spectra corresponding to parallel and perpendicular polarization directions, A|| and A⊥. However, the static approach is subject to instrumental and sample fluctuations during the experiment and therefore lacks the sensitivity for the determination of small dichroic effects. In addition, the sequential measurement is relatively time consuming. To overcome these problems, the polarization modulation technique is used to measure spectral dichroism with high sensitivity. The sensitivity improvement comes from the fact that the dichroic difference spectrum is measured directly by modulating the polarization of the incident IR beam at high frequency with a photo-elastic modulator (PEM). The modulation approach is essential for highly demanding experiments such as vibrational circular dichroism (VCD) where the dichroic difference is usually on the level of 10^4 to 10^5 absorbance unit. In this chapter, we focus on polarization modulation-based techniques for IRRAS, VLD and VCD measurements.

5.2 Photoelastic modulator (PEM)

The PEM is a device used for modulating or varying (at a fixed frequency) the polarization of a beam of light. The polarization of IR light can be modulated using a PEM with a ZnSe crystal. This crystal is periodically stressed by compression and stretch during operation, producing a birefringence that changes the polarization of IR light. Using a PEM90™ photoelastic modulator (Hinds Instruments, Hillsboro, OR) operating at 50 kHz, as an example, the polarization directions of the IR light at different phases of the mechanical stress are illustrated in Figure 5.1. The linear polarization modulation of this modulator, used for IRRAS and VLD, is produced at twice the frequency of the mechanical stress, i.e. 100 KHz, whereas its circular polarization modulation, used for VCD, is produced at the same frequency of the mechanical stress.

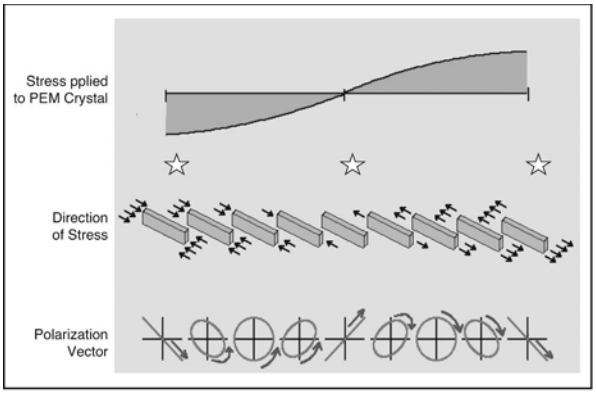

Figure 5.1. Polarization direction variation as a function of periodical stress in PEM-90.

5.3 Dual-channel synchronous sampling sechnique (SST™)

Research-grade iS50R FTIR spectrometers contain two independent, electronically matched digitizers on the SST module. Each digitizer has an associated software-controlled amplifier and electronic filters. The two digitizers can be used either independently or simultaneously. This dual-channel digitization capability allows simultaneous acquisition of two signals that are generated in double modulation experiments such as polarization modulation-based IRRAS, VLD and VCD. The Fourier modulation by the interferometer* gives the "static" sum reference or background spectrum, and the polarization modulation by a PEM produces the differential spectrum between different polarization directions. The dual-channel capability allows both spectra to be recorded simultaneously. Figure 5.2 illustrates a generic dual-channel electronic setup on the PEM module for polarization modulation experiments. Channels A and B of the spectrometer digitize the sum and difference signals from the demodulator, respectively.

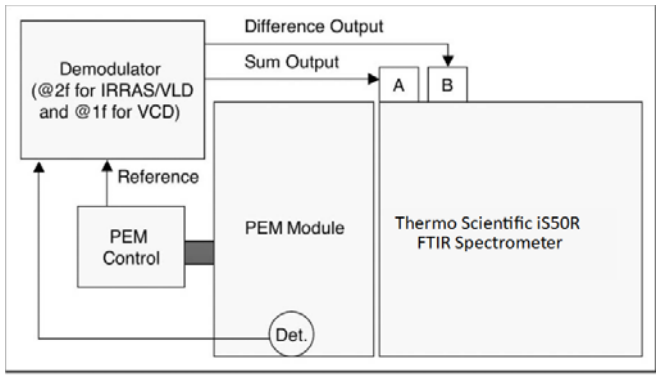

Figure 5.2. Dual-channel electronics setup on the PEM module for polarization modulation-based experiments: IRRAS, VLD and VCD. Demodulation frequencies are set at 2f (e.g. 100kHz) for IRRAS and VLF and 1f (e.g. 50 kHz) for VCD.

In principle, a polarization modulation experiment (IRRAS, VLD or VCD) can be conducted sequentially in two separate experiments on a spectrometer with just one digitizer. However, since the differential absorption signals are typically very weak, the de-modulated dichroic difference signals can be masked by any instant changes in the environment such as water vapor and CO2 in the system or any change in the spectrometer between the two measurements.

The advantages of polarization modulation over the static approach can only be fully realized by using simultaneous dual-channel data collection with two digitizers. In this case, both the static background and the differential absorption are recorded simultaneously in a single experiment. With dual-channel capability, any spectral features other than the differential absorption by the sample will be almost completely canceled out after the differential signal is normalized over the static reference collected simultaneously. In addition, dual-channel collection reduces the experiment time by half

*The Fourier frequencies exist in dual channel polarization modulation experiments due to the use of the continuous scan mode. The use of step-scan is not necessary for the high frequency polarization modulation experiments. The polarization modulation frequency at 50 kHz is well above the Fourier frequency range for the mid-infrared continuous scan mode with a relatively slow scan speed.

compared to single-channel spectroscopy. The dual-channel advantage is demonstrated by an IRRAS experiment with a sample of $C_{16}H_{33}SH$ sub-monolayer on gold substrate. The experiment was conducted with a Thermo Scientific Research Module in a PM-IRRAS configuration. The external Research Module was opened and then closed right before each data collection was started. During the data collection, the amount of water vapor and CO_2 was changing because of the purge. With dual-channel data collection, the water vapor and CO2 bands are almost completely removed from the PM-IRRAS spectrum, as illustrated in Figure 5.3. However, there was a considerable amount of water vapor and CO_2 features on the ratioed PM-IRRAS spectrum obtained by the single channel, sequential measurements, despite the fact that the conditions for all measurements were carefully reproduced.

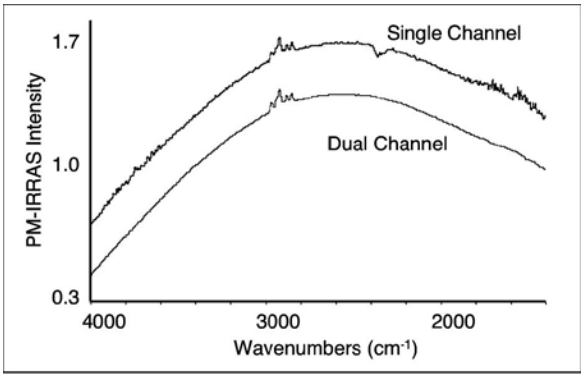

Figure 5.3. Unnormalized PM-IRRAS spectra of $C_{16}H_{33}SH$ self-assembled mono-layer on gold measured by sequential single-channel and simultaneous dual-channel data collection. Water vapor and CO2 bands are nearly completely removed on the dual-channel spectrum.

5.4 Polarization modulation infrared reflection absorption spectroscopy (PM-IRRAS)

5.4.1 Introduction

Infrared reflection absorption spectroscopy (IRRAS) is a useful technique for studying thin films on reflective substrates. While optically reflective substrates can be formed from different kinds of condensed phase (solid or liquid) substances, metallic (or electrically conductive) substrates are mainly discussed in this section. Molecular orientations of a thin film on a metallic substrate can be determined based on the selective absorption of sand p-polarized light by the adsorbed molecules when the incident angle is in the grazing angle range.

5.4.2 Surface Selection Rule

When a beam of light is reflected from a metallic substrate, the phase of the reflected beam shifts by an amount determined by the angle of incidence, the state of polarization and the wavenumber of the light. As illustrated in Figure 5.4, the phase shift for the s-polarized beam (with electric field vector, E, perpendicular to the plane of incidence, or parallel to the surface of the sample) is close to 180°, irrespective of the angle of incidence and wavenumber.[65] Thus the electric field vectors of the incident and reflected beams for s-polarized light nearly cancel out at the surface. Since the IR absorption is proportional to $(\mu E)^2$, where μ and E refer to the transition dipole moment of the sample and the electric field intensity of IR light, this cancellation of the E vector at surface ($E \geq 0$) means that little absorption is to be expected from a thin film on a metallic substrate for s-polarized IR light, regardless of the orientation of the transition dipole. The phase shift for a p-polarized beam (with E parallel to the plane of incidence, or perpendicular to the surface of the sample) increases rapidly from as small as a few degrees to the extreme 180° as the angle of beam incidence increases from 80 – 90°. When the phase shift is in the range of 0 – 90°, as it is the most common case for grazing angle incidence over large mid-IR wavenumber region, the incident and reflected beams usually produce a finite E perpendicular to the metal surface. Therefore, the p-polarized beam is strongly absorbed by molecules with transition moments oriented perpendicularly to the film surface. Figure 5.4 graphically illustrates the surface selection rule. In the figure, the directions of polarization and transition dipole of the adsorbed molecules are labeled. The shortening of the bar representing the reflected p-polarized light indicates absorption by the surface molecules oriented perpendicular to the surface.

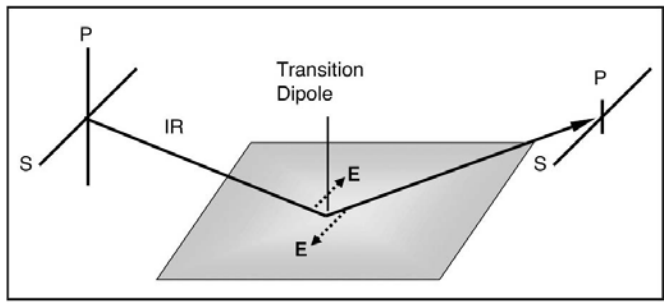

Figure 5.4. Schematic illustration of the surface selection rule in IRRAS. The phase shift of electric field vector E, between incident and reflected beams for s- and p-polarized light are the theoretical basis of IRRAS for molecular orientation measurements.

5.4.3 PM-IRRAS optical setup on the PEM module

The PEM Module for IRRAS has an integrated pin-in-place design for all optical components which are preinstalled and pre-aligned in factory. This PEM module has a variable reflection geometry to allow the user to easily change typical reflection angles of 83°, 72°, and 67° for samples with metallic, glass, and

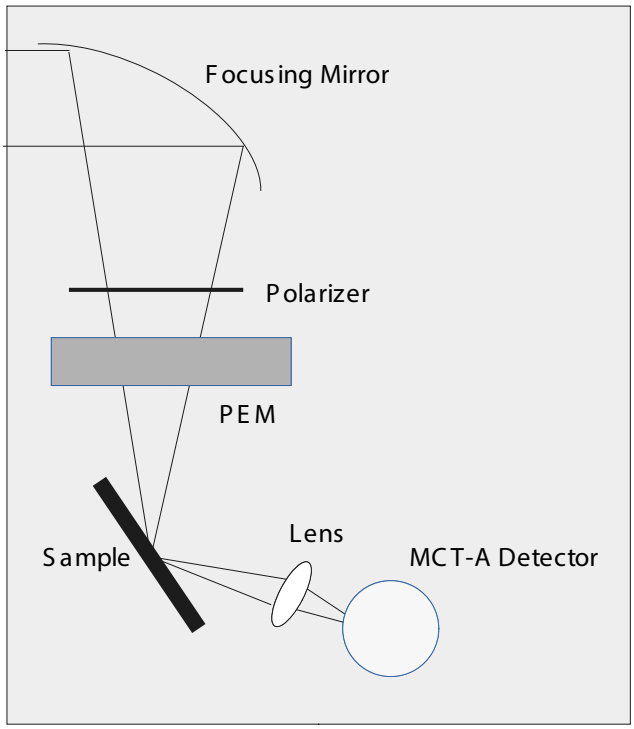

Figure 5.5. Schematic of the optical setup of the external Research Module for IRRAS.

dielectric substrates, respectively, by placing the detector in the corresponding locations. Figure 5.5 shows the optical setup of the PEM module. The parallel IR beam from the spectrometer is reflected twice by two flat mirrors and then focused onto the sample surface by a parabolic mirror. Between the focusing mirror and the sample are a wire-grid polarizer, oriented parallel to the p-polarized IR light, and a photo-elastic modulator that modulates (rotates) the electric field vector of the IR light between p- and s-polarizations. The polarization modulated IR light impinges onto the surface of the sample at an angle that is suitable for the substrate. The reflected light from the sample surface is then collected by the detector assembly equipped with a focusing lens. Note that reflective focusing optics may scramble part of the polarized light and introduce artifacts in polarization modulation experiments (IRRAS, VLD and VCD) if they are used after the photo-elastic modulator. Thus, it is critical to focus the light onto the detector element using a lens instead of a mirror.

5.4.4 PM-IRRAS signal demodulation and data process

In a typical PM-IRRAS experiment, two modulations are applied simultaneously: the Fourier modulation produced by the interferometer and the polarization modulation by the PEM. Thus the raw detector signal contains contributions from both modulations if proper electronic filtering is used. Figure 5.6 shows interferograms of the detector signal with the PEM turned on and off, respectively. It can be seen that when the PEM is turned on, the interferogram has both a high frequency contribution from the polarization modulation and a low frequency signal associated with the normal interferometric modulation.

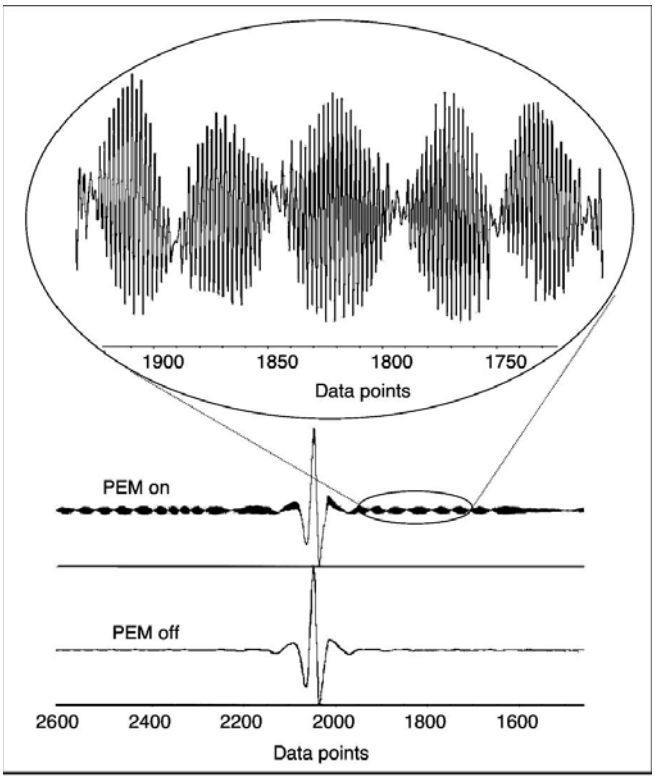

Figure 5.6. Raw PM-IRRAS interferograms with PEM turned on and off. Low frequency and high frequency signals correspond to Fourier modulation and photoelastic modulation respectively.

This raw PM-IRRAS signal from the detector can be mathematically expressed as follows:[66]

$$I_d = k(\sigma, f_F, D, \dots)\left[\left(I_p + I_s\right) - 2\left(I_p - I_s\right)J_2(\phi_0)\right]cos(2f\pi_{PEM}t) \quad (5\text{-}1)$$

where k (σ, f_F, D,…) is a coefficient that is primarily related to wavenumber (σ) region, Fourier modulation frequency f_F, D* and the preamplifier of the detector, I_p and I_s are the intensities of reflected p- and s-polarized light, $J_2(\varphi_0)$ is the second-order Bessel function with φ_0 equal to the function of the maximum voltage applied on the PEM. For simplicity we assume that k (σ, f_F, D…) is not polarization dependent, and we neglect the (I_p I_s) $J_0(\varphi_0)$ term since it is much smaller than the DC term (I_p + I_s) for films on metallic substrates.

As illustrated in Figure 5.2, this detector signal is fed into the input channel of a synchronous sampling demodulator (SSD) that has a tuned demodulation frequency of twice the f_{PEM} (e.g. 50 kHz) and a high limit of signal input, usually up to ±10 volts. The demodulator has built-in lowpass and highpass electronic filters that optimize the sum (I_p + I_s) and the difference [$J_2(\varphi_0)$ (I_p- I_s)] PM-IRRAS signal outputs, respectively. The sum and difference outputs are then digitized simultaneously by two electronically balanced digitizers of the spectrometer. Thus an experimental PM-IRRAS spectrum can be calculated by ratioing the difference over the sum as follows:

$$\left(\frac{\Delta I(d)}{\Sigma I(d)}\right)_{exp} = \frac{J_2(\varphi_0)[I_p(d) - I_s(d)]}{I_p(d) + I_s(d)} \quad (5\text{-}2)$$

In Equation (5-2), the difference in signal amplification and filtering between the two channels for overall electric signal process, and the difference in overall optoelectronic setup for p and s linear polarizations are ignored and the notation d refers to the thickness of the film on the metal substrate. When these two factors are considered, Equation (5-2) becomes:

$$\left(\frac{\Delta I(d)}{\Sigma I(d)}\right)_{exp} = \frac{J_2(\varphi_0)g[\gamma I_p(d) - I_s(d)]}{\gamma I_p(d) + I_s(d)} \quad (5\text{-}3)$$

where g = G+/G, the ratio of overall gain for the two channels, and $\gamma = C_p/C_s$, the ratio of overall responses of the opto-electronic setup for p and s linear polarizations. Equation (5-3) indicates that the second order Bessel function envelope with multiple arches and nodes will define the overall spectral shape of the PM-IRRAS spectrum. In order to eliminate the factors $J_2(\varphi_0)$ and g, Equation (5-3) can be divided by the equivalent PM-IRRAS signal from the bare substrate under same experimental conditions to give the normalized PM-IRRAS spectrum:

$$\left(\frac{\Delta I(d)}{\Sigma I(d)}\right)_{norm} = \frac{\left(\frac{\Delta I(d)}{\Sigma I(d)}\right)_{exp}}{\left(\frac{\Delta I(0)}{\Sigma I(0)}\right)_{exp}} = \frac{\frac{J_2(\varphi_0)g[\gamma I_p(d) - I_s(d)]}{\gamma I_p(d) + I_s(d)}}{\frac{J_2(\varphi_0)g[\gamma I_p(0) - I_s(0)]}{\gamma I_p(0) + I_s(0)}} \quad (5\text{-}4)$$

$$= 1 + \frac{2\gamma\rho}{1 - \gamma^2\rho^2} A(d)_{pseu}$$

where $\rho = (I_p(0)/I_s(0)$ and $A(d)_{pseu} = 1\text{-}(I_p(d)/I_p(0)$, is a pseudo absorption spectrum of the film. Based on a first order

approximation of the series expression of ln x, i.e. ln x ≈ 1 – (1/x) for x > ½, the true absorbance spectrum of the film, A(d) can then be approximated as follows:

$$A(d) = log(1/R) = ln(1/R)/ln10 \approx 0.434(1-R)$$

$$A(d) = 0.434\left[1 - \left(I_p(d)/I_p(0)\right)\right] = 0.434A(d)_{pseu} \quad (5\text{-}5)$$

where R is the reflectance. By substituting $A(d)_{pseu}$ solved from Equation (5-4) into Equation (5-5), we obtained:

$$A(d) \approx 0.217\left((1-\gamma^2\rho^2)/\gamma\rho\right)\left[\left(\Delta I_p(d)/\Sigma I_p(d)\right)_{norm} - 1\right] \quad (5\text{-}6)$$

As a first order approximation, it is reasonable to consider ρ as a constant over the entire mid-IR range. For metallic substrates at near grazing incidence, ρ is very close to and less than 1, and in contrast, γ may vary from zero to infinity depending on the preferential polarization of the optical setup. However, if the polarizing effects of all optical parts of the PM-IRRAS setup are minimized, γ can be kept very close to 1. A(d) in general should be positive according to Equation (5-6), since when γρ < 1 the surface bands on an experimental PM-IRRAS spectrum defined by Equation (5-2) are oriented upwards above the $J_2(\varphi_0)$ curve, and subsequently the normalized PM-IRRAS signal is less than 1. For a typical sample, i.e. an organic thin film on a gold-coated substrate, ρ≈0.95 (at σ=1000 cm^{-1}, ρ varies very little across the entire mid-IR spectrum) and γ≈1, Equation (5-6) then reduces to:

$$A(d) \approx 0.0223\left[\left(\Delta I_p(d)/\Sigma I_p(d)\right)_{norm} - 1\right] \quad (5\text{-}7)$$

Equation (5-7) can be utilized to quickly convert a normalized PM-IRRAS spectrum to a conventional absorbance spectrum. Figure 5-7 shows a directly measured absorbance spectrum of poly-l lysine film on a gold-coated glass substrate collected by using a Smart SAGA™ grazing angle accessory (top) and a converted absorbance spectrum of the same sample, collected by using dual-channel PM-IRRAS and processed by Equation (5-7) (bottom). The grazing angle difference between the regular IRRAS (80°) and PM-IRRAS (83°) was also factored in for the calculation of the converted absorbance spectrum. It can be seen that the converted absorbance spectrum matches well the spectrum directly measured by regular IRRAS as illustrated by the band intensity at 1664 cm^{-1}, i.e. 0.00123 vs. 0.00138 absorbance, respectively. The tremendous advantages of dual-channel PM-IRRAS over conventional IRRAS in terms of SNR and clean removal of moisture contamination are also clearly demonstrated.

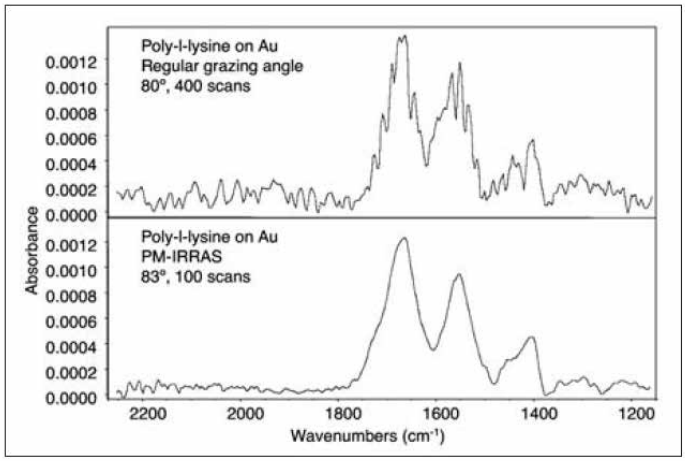

Figure 5.7. Comparison of IRRAS spectra of poly-l-lysine on gold collected by using a conventional grazing angle accessory (top) and a dual-channel PM-IRRAS (bottom). The PM-IRRAS spectrum has been converted to absorbance units using Equation (5-7). The grazing angle difference induced path length difference between conventional IRRAS (80°) and PM-IRRAS (83°) waas also calibrated on the converted spectrum.

5.4.5 Application examples

As a very sensitive technique, PM-IRRAS has been used to characterize thin films on reflective substrates in many fields. Thin films of this kind with thicknesses of < 400 Å are generally well suited for PM-IRRAS. The most common applications are studies of Langmüir Blodgett (LB) (monolayer) organic films on highly reflective metallic substrates such as gold or gold-coated materials. In addition, PM-IRRAS has also been used to study monolayer films on water/air interfaces, a much more challenging environment for conventional IRRAS detection where water absorbs IR very strongly.

Monolayers on metallic substrates. PM-IRRAS spectra of monolayers or sub-monolayers can be obtained easily in less than one minute due to the high sensitivity of the technique and the high reflectivity of metallic substrates. Illustrated in Figure 5.8 is the PM-IRRAS spectrum of cadmium arachidate on gold measured at 4 cm^{-1} resolution in ~20 sec. Figures 5.9 and 5.10 show unnormalized and normalized/converted PM-IRRAS spectra of decanethiol ($C_{10}H_{22}S$) and tetradecanethiol ($C_{14}H_{30}S$) films on gold-coated glass substrates respectively. The PEM

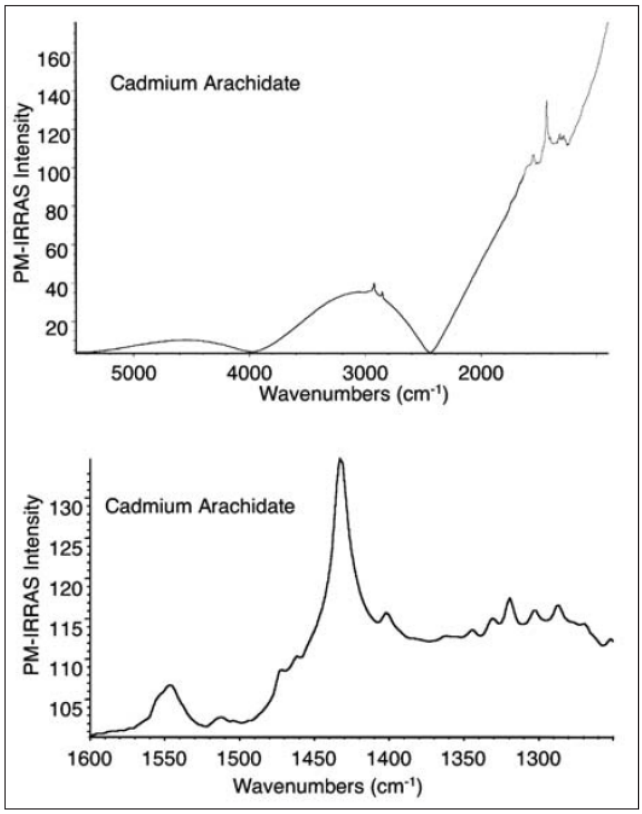

Figure 5.8. Unnormalized PM-IRRAS spectrum of cadmium arachidate on gold measured at 4 cm^{-1} resolution in about 20 sec, showing the bands of the film shown above the $J_2(\varphi_0)$ curve (top) and the enlarged finger print region with good SNR (bottom)

modulation efficiency was adjusted to regions around 1500 cm^{-1} and 3000 cm^{-1} respectively for measuring decanethiol and tetradecanethiol films. The converted absorbance spectra were calculated using Equation (5-7) and absorbance values are on a similar scale to monolayers as obtained with a different and rather tedious approach.[67,68]

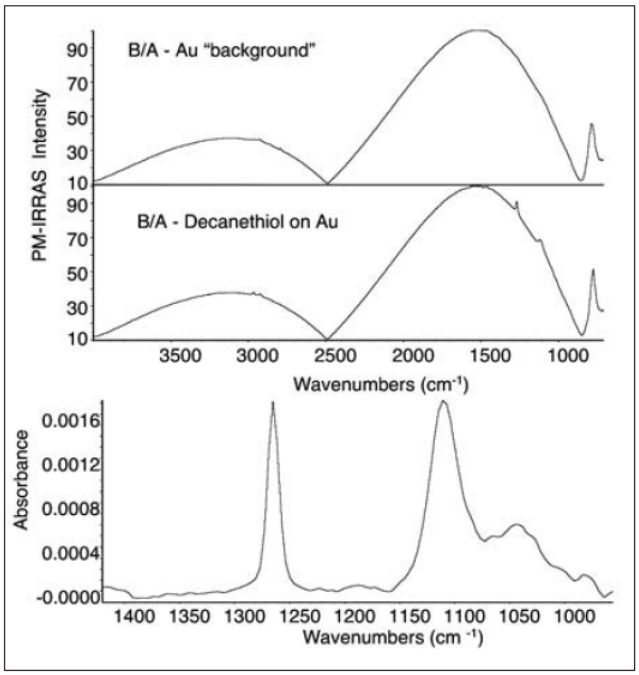

Figure 5.9. Unnormalized PM-IRRAS spectra of gold-coated glass (mirror) and decanethiol ($C_{10}H_{22}S$) monolayer film on the gold-coated glass substrate (top), and normalized and converted PM-IRRAS spectrum of the film sample in absorbance units (bottom).

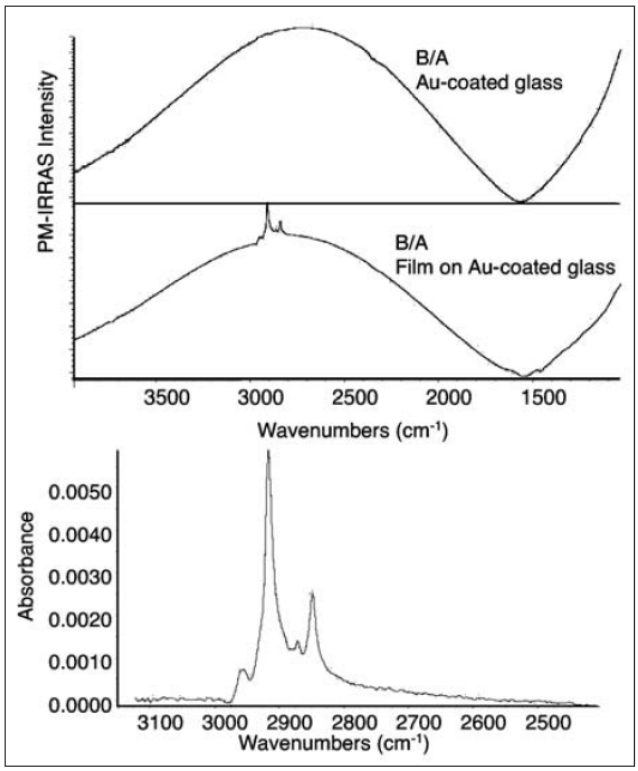

Figure 5.10. Unnormalized PM-IRRAS spectra of gold-coated glass substrate and tetradecanethiol ($C_{14}H_{30}S$) monolayer film on the gold-coated glass substrate (top), and normalized and converted PM-IRRAS spectrum of the film sample in absorbance units (bottom). *Raw data courtesy of Jun Hu of the University of Akron, Akron, Ohio.*

Characterization of lubricants on hard disks. The drive for continuing improvement in storage capacity and miniaturization of data storage media of hard disks used in modern computers has increased the demand for highly sensitive analytical tools that allow fast and reliable measurements of thin films. PM-IRRAS is one of the very successful techniques widely utilized in analyzing computer hard disks.[69]

A typical hard disk has multilayered films deposited/coated on an aluminum substrate. Its cross-section view is shown in Figure 5.11. In order to increase the storage capacity of a hard disk, the distance between the read/write (R/W) head and the magnetic media layer where the data are stored must be as short as possible. A thin layer of lubricant protects the data stored in the magnetic medium of the hard disk from corrosion and contact with the R/W head.[70-72] The lifetime and performance of hard disk drives are critically dependent on the thickness of lubricants on the surface. Over supply of lubricant would increase the stiction force on disk drive motors at startup and shortage of lubricant does not protect the disk from damage due to excessive wear and corrosion.

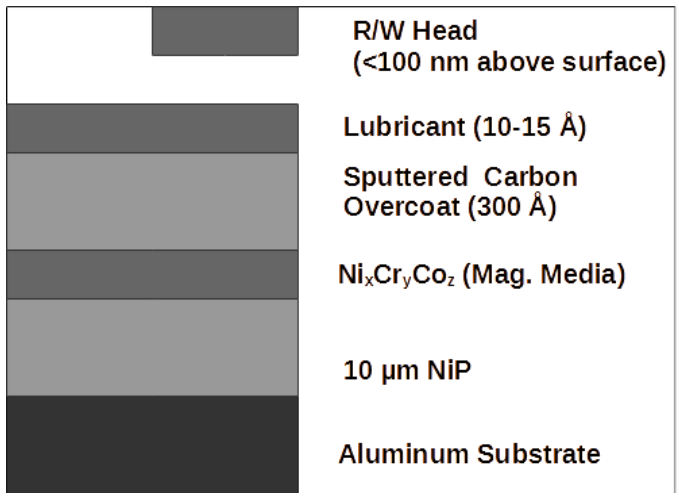

Figure 5.11. Multi-layered structure of surface coatings on a typical computer hard disk drive.

The performance of hard disk drives is enhanced considerably by the addition of small amounts of additives to lubricants. An example of such an additive is a cyclic phosphazine (X1P) lubricant (The Dow Chemical Co., Midland, MI).[73] It is widely used by many disk drive manufacturers as an additive to the traditional perfluoropolyalkyl ether (PFPE) lubricants such as Fomblin® ZDOL (Ausimount USA, Thorofare, NJ). It has been shown to improve significantly the performance of hard disk drives under adverse conditions, particularly hot and humid environments. The amount of the X1P additive used is low and typically covers <10% of hard disk surface as a molecular monolayer. The surface coverage of the X1P has to be controlled precisely in order to achieve the optimal performance.

Traditionally, the amount (or thickness) of the X1P is measured by Xray photoelectron spectroscopy (XPS) or wet chemical extraction followed by GC/MS analysis. The sensitivity of XPS is not sufficient to measure the low concentration of X1P used in manufacturing. The time consuming GS/MS approach only measures the total amount of X1P on the entire surface of a hard disk, thus the calculation of its average distribution lacks spatial information. In addition, both XPS and GC/MS are destructive techniques. These limitations prevent them from potential online or at-line monitoring of the hard disk manufacturing.

PM-IRRAS is ideally suited for analyzing the lubricant and its additives on such hard disks. It has been used successfully for both qualitative and quantitative analysis of thin films on hard disks by a number of disk and lubricant manufacturers in their analytical laboratories. Shown in Figure 5.12 are unnormalized PM-IRRAS spectra of a lubed disk and bare disk substrate. The PEM modulation efficiency was tuned to maximize spectral intensity around 1300 cm^{-1}. The absorption peaks for the lubricant (ZDOL) and the additive (X1P) are very small and they occur above the $J_2(\varphi_0)$ curve in the region where strong water vapor absorption occurs but this was removed nearly completely by the dual-channel data collect.

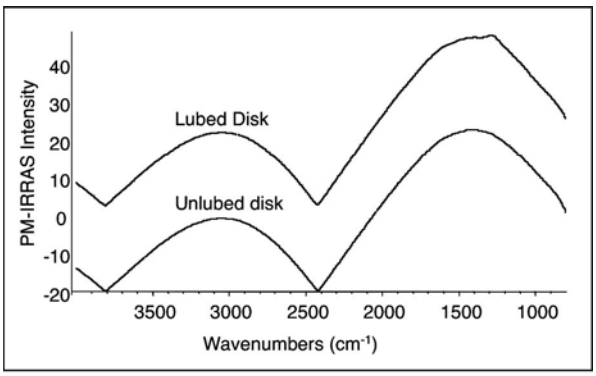

Figure 5.12. PM-IRRAS spectrum of a lubed (top) and unlubed hard disk (bottom). Spectral features of the lubricant are shown above the $J_2(\varphi_0)$ curve for the lubricated disk.

The normalized PM-IRRAS spectra for a set of hard disks that have different amounts (or thickness) of ZDOL are shown in Figure 5.13, where a clear correlation between the intensity of the ZDOL band at 1281 cm^{-1} and the amount of the ZDOL lubricant is observed. The plot in Figure 5.14 shows a linear relationship between the baseline-corrected PM-IRRAS peak height of the ZDOL band at 1281 cm^{-1} and the thickness of the lubricant determined by GC/MS method. A similar relationship can be also found for the amount of X1P additive added in the lubricant.[69]

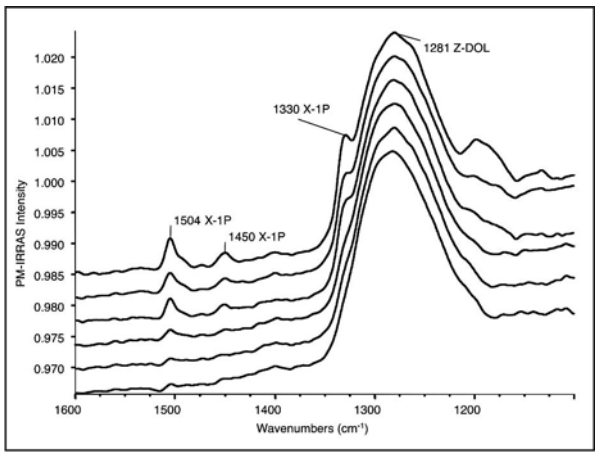

Figure 5.13. Normalized PM-IRRAS spectra for a set of hard disks with different amounts of Z-DOL.

It can be seen from this application that PM-IRRAS is a superior technique for qualitative identification and thickness determination of the hard disk lubricants and additives. All measurements were made without any sample preparation or alteration. The high sensitivity of PM-IRRAS allows the measurement to be made in a few minutes compared to the time-consuming chemical extraction process in the GC/MS approach.

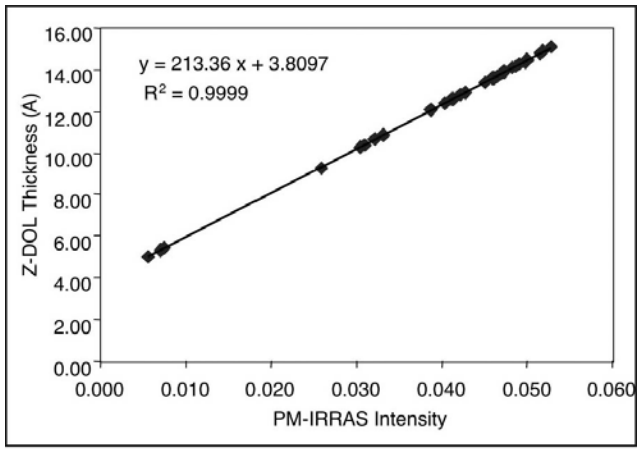

Figure 5.14. Linear relationship between the baseline-corrected PM-IRRAS spectral peak height of the Z-DOL band at 1281 cm^{-1} and the thickness of Z-DOL determined by the GC/MS method.

***In situ* studies on interfacial reactions / films between metal surfaces and gas or liquid phases.** The above PM-IRRAS application examples are considered *ex situ* studies where samples were prepared separately prior to the measurement. Another popular application of the PM-IRRAS technique is *in situ* studies on interfacial reactions between metal surfaces and gas or liquid phases. In this situation, a kinetic PM-IRRAS operation mode may be utilized if monitoring the entire reaction process in real time is critical. Active *in situ* PM-IRRAS research work has been conducted, including the specific interactions of gaseous analytes with polymeric coatings deposited on gold substrates.

In this study, the *in situ* spectra of polycarbonate bisphenol-A and diethyleneglycol adipate coatings exposed to acetonitrile, oxylene, or dimethyl sulfoxide vapor were measured.[74] The resulting spectra were analyzed to determine structural perturbations of the film induced by the overlying vapor and the nature of the interaction between the film and vapor. The principal advantage of PM-IRRAS is that the spectra are measured *in situ*. There is no contribution from the organic vapor reactant even though a fairly high concentration is flowing over the sample while the spectra are measured. Further studies were conducted on reaction kinetics that monitor the reversibility of the reaction as the organic vapor pressure changes.

5.5 Polarization modulation vibrational linear dichroism (PMVLD)

5.5.1 Introduction

The absorption of infrared radiation by an oriented sample is sensitive to the state of polarization of the incident radiation with respect to a reference direction. The reference direction can be defined by the stretching direction of a polymer, the director of a liquid crystal or a monolayer film, the polarization direction of a laser in photoinduced orientation studies, or more generally, by the direction of the external constraint that produces the anisotropy in the sample.

The anisotropic optical absorption of oriented samples, so called dichroism, can be analyzed by measuring spectra using light polarized parallel and perpendicular to the fixed reference direction. This type of experiment is called infrared linear dichroism (IRLD), or in a more general sense, vibrational linear dichroism (VLD). The dichroic ratio R_d and dichroic difference ΔA are the common parameters that are used to characterize the

degree of optical anisotropy in oriented samples and they are defined by Equations (5-8) and (5-9) respectively:

(5-8) $R_d = A_{\parallel}/A_{\perp}$

(5-9) $\Delta A = A_{\parallel}/A_{\perp}$

where $A_{\parallel}$ and $A_{\perp}$ represent, respectively, the integrated absorbance of the investigated band measured with the radiation polarized parallel and perpendicular to the reference direction.

VLD measurement for a selected absorption band of oriented samples involves the determination of either the dichroic ratio or the dichroic difference. This measurement can be achieved using static polarization or modulated polarization. In the case of using static polarization, the direction of the electric field vector is selected by a linear polarizer. Two independent spectra are necessary to calculate the dichroic ratio or the dichroic difference.

For samples showing uniaxial symmetry with respect to a reference axis, the recording of the polarized spectra at normal incidence is the most straightforward way to measure the VLD. The two spectra can be obtained by a 90° rotation of either the polarizer or the sample. In order to avoid any environmental perturbation in the sample compartment of the spectrometer, the rotation of the polarizer or of the sample can be motorized and controlled directly by the spectrometer computer.

For the first case (rotation of the polarizer), the same part of the sample is illuminated by the infrared beam to record the parallel and perpendicular spectra. This method, however, requires the recording of two reference spectra, one for each polarization direction, since the beamsplitter of FTIR instruments is polarization sensitive. In the second case (rotation of the sample), only one reference spectrum is required but it is important to make sure that the sample is perfectly homogeneous, since different areas could be illuminated as the sample is rotated. For both cases, the polarizer should be the last optical element before the sample or the first one after the sample to avoid depolarization by other elements.

5.5.2 VLD measurement by polarization modulation

Dichroism measurements using static polarization require the sequential recording of two different spectra to obtain the polarized absorbance parallel and perpendicular to the reference direction. However, $A_{\parallel}$ and $A_{\perp}$ are subject to instrumental and sample fluctuations occurring between the two measurements. This static method of measuring vibrational linear dichroism lacks sensitivity for the determination of small dichroic effects. Moreover, the need for the separate collection of the $A_{\parallel}$ and $A_{\perp}$ spectra increases total measurement time. To overcome these drawbacks of the static approach, the polarization modulation technique is used to measure the linear dichroism of oriented samples with high sensitivity.[75,66-80] The sensitivity of this method comes from the fact that the dichroic difference spectrum is measured directly by modulating the polarization of the incident infrared beam at high frequency with a PEM. Thus, dichroic difference spectra can be obtained in a few seconds, and the corresponding kinetic measurements can be collected over a short time scale.[81-82]

The optical setup for VLD is shown in Figure 5.15. At the output of the interferometer, the infrared beam presents an intensity modulation at Fourier frequency $f_F = 2v\sigma$, typically between 0.1 to 2 kHz, depending on the IR wavenumber (σ) and the velocity (v) of the interferometer moving mirror. The beam is then polarized with a linear polarizer and passes through a PEM90.

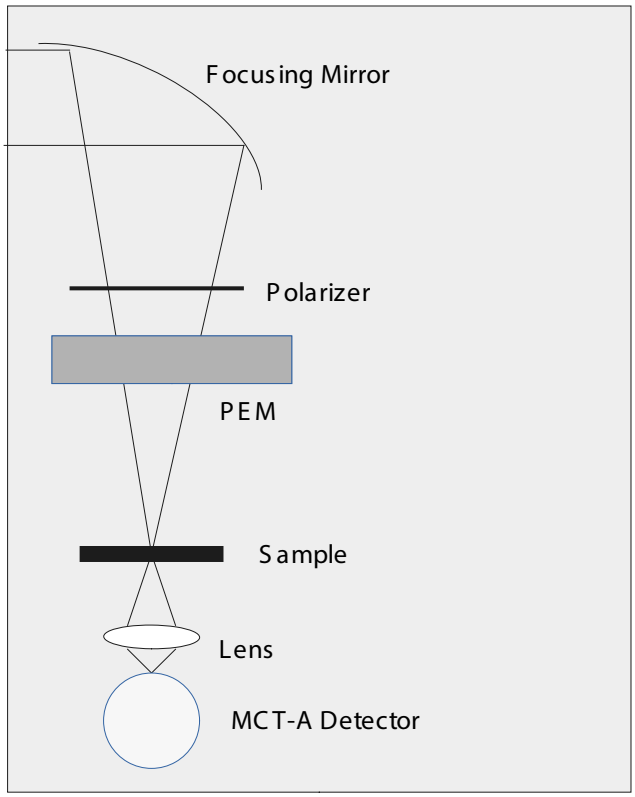

Figure 5.15. Optical setup for a polarization modulation-based VLD experiment. This setup is also similar to the VCD experiment, as will be discussed in **Section 5.6.3**.

The PEM, as described in **Section 5.2**, consists of an infrared transparent material (zinc selenide, calcium fluoride, or silicon) coupled to piezo-elastic drivers, and modulates the polarization of the infrared beam between the parallel and perpendicular polarization states with respect to the reference direction at a fixed frequency $2f_{PEM}$ (100 kHz). After transmission through the sample, the double-modulated infrared beam is focused with a lens on an infrared detector.

In a PMVLD experiment, the detector output can be expressed by Equation (5-10):[83]

$$I_d = CI_0(\omega)[(T_{\parallel} + T_{\perp}) + (T_{\parallel} - T_{\perp})\, J_0(\phi_0)$$

(5-10)

$$+2(T_{\parallel} - T_{\perp})\, J_2(\phi_0)\cos(2\pi f_{PEM}t)]$$

where C is a constant accounting for the transmittance of the optical setup and for the detection yield, $I_0(\omega)$ is the light intensity after the polarizer, $T_{\parallel}$ and $T_{\perp}$ are the parallel and perpendicular transmittance of the sample, respectively, Jn is the Bessel function of order n, φ_0 is the maximum dephasing introduced by the PEM. The detected signal is thus the sum of DC [first two terms in Equation (5-10)] and AC [last term in Equation (5-10)] signals. The DC signal carries mainly the intensity modulation induced by the moving mirror of the interferometer [the term containing $J_0(\phi_0)$ is relatively small in total DC signal], whereas the AC term contains the polarization modulation induced by the PEM. The two signals are separated into two different channels by means of an electronic filter with high and lowpass outputs. The AC signal is demodulated by a lock-in amplifier or a dedicated demodulator, at twice the frequency of the PEM (i.e. $2f_{PEM}$). Both DC and AC signals are treated as usual with high and lowpass filtering and amplification. They are simultaneously

sampled and converted by two analog-to-digital converters. Eventually, the two channel interferograms are Fourier-transformed and then ratioed to give the VLD raw spectrum (S) of the sample without calibration:

$$S = \frac{[AC]_s}{[DC]_s} = \frac{2G(T_{\parallel} - T_{\perp})J_2(\phi_0)}{[(T_{\parallel} + T_{\perp}) + (T_{\parallel} - T_{\perp})J_0(\phi_0)} \quad (5\text{-}11)$$

where G is an overall constant factor due to the different amplification and filtering on the two channels. This experimental spectrum contains $Jn(\varphi_0)$ factors which can be determined by proper VLD calibrations by using a linear polarizer[55,96-97,100] as described in the following section.

5.5.3 VLD calibration and polarization modulation-based dichroic difference

The VLD calibration measurements are performed by replacing the sample with a reference linear polarizer. The linear polarizer is oriented either parallel or perpendicular to the polarizer positioned in front of the PEM. Thus, the polarizer represents a sample that completely transmits one polarization and totally absorbs the other. The respective calibration reference spectra $R_{\parallel,\parallel}$, and $R_{\parallel,\perp}$, derived from **Equation (5-11)** by suppressing $T_{\parallel}$ or $T_{\perp}$, are given by the following relations:

$$R_{\parallel,\parallel} = \frac{[AC]^R_{\parallel,\parallel}}{[DC]^R_{\parallel,\parallel}} = \frac{2\ '|J_2(\phi_0)|}{[1 + J_0(\phi_0)]} \quad (5\text{-}12)$$

and

$$R_{\parallel,\perp} = \frac{[AC]^R_{\parallel,\perp}}{[DC]^R_{\parallel,\perp}} = \frac{2\ '|J_2(\phi_0)|}{[1 - J_0(\phi_0)]} \quad (5\text{-}13)$$

where G' is the same gain factor for the two channels as defined in **Equation (5-11)** for the calibration measurements. Note that in deriving **Equations (5-12)** and **(5-13)**, Mertz phase correction in Fourier transform is assumed, and therefore the reference single beam spectra corresponding to the demodulated AC signals, $R_{\parallel,\parallel}$, and $R_{\parallel,\perp}$, should be positive.

By solving $J_1(\phi_0)$ and $J_2(\phi_0)$ from **Equations (5-12)** and **(5-13)** and substituting them into **Equations (5-11)**, the dichroic difference spectrum can be expressed as a function of the experimental spectrum S and the two calibration reference spectra, $R_{\parallel,\parallel}$, and $R_{\parallel,\perp}$:

$$\Delta A = A_{\parallel} - A_{\perp} = \log\frac{T_{\perp}}{T_{\parallel}} = \log\left[\frac{R_{\parallel,\perp}\left(-, R_{\parallel,\parallel} - S\right)}{R_{\parallel,\parallel}\left(-, R_{\parallel,\perp} + S\right)}\right] \quad (5\text{-}14)$$

When the gain factor for the two channels are identical for both sample and calibration measurements, i.e. G = G', **Equation (5-14)** is further simplified to Equation (5-15):

$$\Delta A = A_{\parallel} - A_{\perp} = \log\frac{T_{\perp}}{T_{\parallel}} = \log\left[\frac{R_{\parallel,\perp}(R_{\parallel,\parallel} - S)}{R_{\parallel,\parallel}(R_{\parallel,\perp} + S)}\right] \quad (5\text{-}15)$$

Thus the dichroic difference can be conveniently calculated from both sample and calibration data. However, the calculation of dichroic ratio ($A_{\parallel}/A_{\perp}$) from PMVLD experimental data remains nontrivial, thus an additional static VLD measurement is suggested.

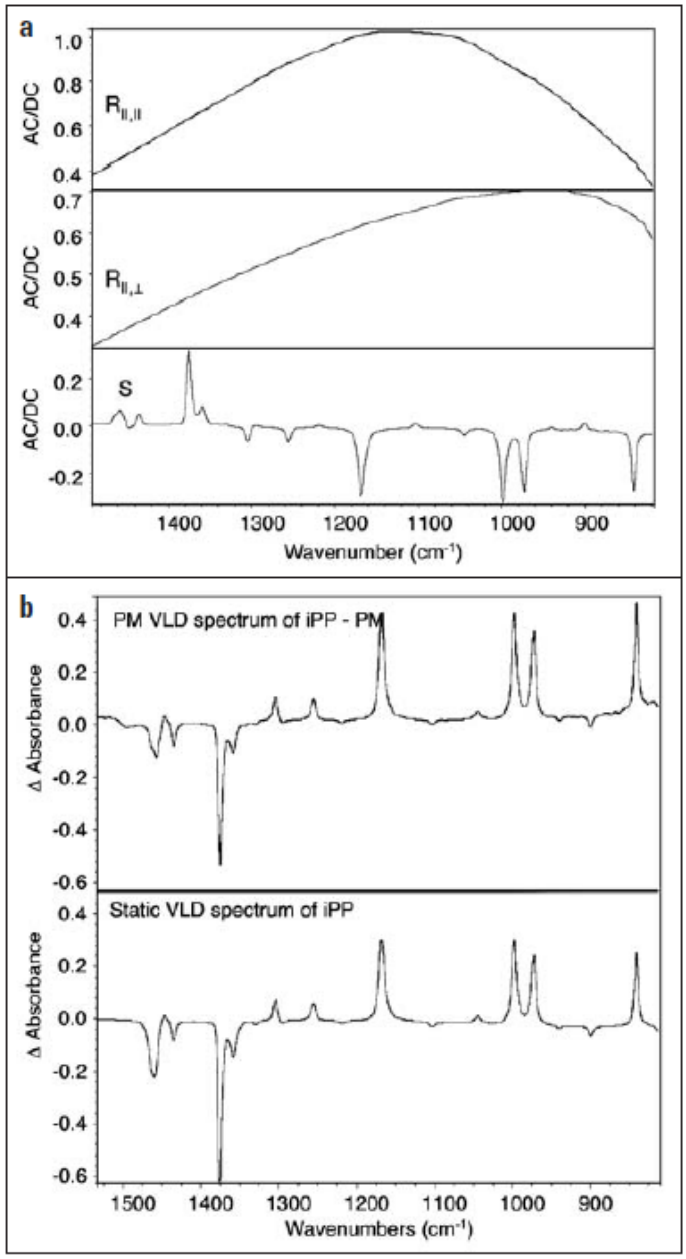

Figure 5.16. a) The PM-VLD spectra of the reference polarizer and iPP film, $R_{\parallel,\parallel}$, and $R_{\parallel,\perp}$ and S; b) The converted and normalized PM-VLD and static VLD spectra of iPP.

5.5.4 Application examples

Polarization modulation vibrational (infrared) linear dichroism has been used to study a variety of polymer films.[78,83] The sensitivity enhancement gained by using polarization modulation over normal static linear dichroic measurement is very significant, allowing dichroic spectral differences as low as 2×10^{-4} absorbance unit to be measured with good SNR.[78]

Polymer samples that have been studied by VLD include isotactic polypropylene (iPP),[78] poly(dimethylsiloxane) (PDMS) networks,[83] poly(methyl methacrylate) (PMMA) doped with the azobenzene dye DR1,[83] and amorphous azopolymer pDR1A.[81] **Figure 5.17** shows a raw PMVLD spectrum of polyvinyl chloride (PVC) collected by using the Dual-channel PEM module. The spectrum is simply the ratio of AC over DC single beams as suggested by **Equation (5-11)**. A more strict spectral process for VLD is illustrated in **Figure 5.16** with a pre-stretched iPP film. The reference spectra $R_{\parallel,\parallel}$, and $R_{\parallel,\perp}$ and sample spectrum S shown in **Figure 5.16a** were the ratios of

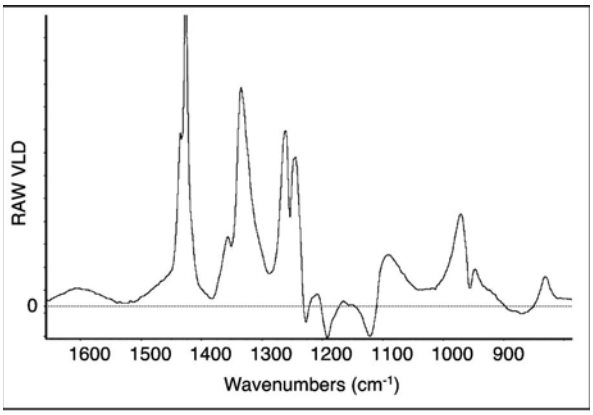

Figure 5.17. Raw PM-VLD spectrum of polyvinyl chloride (PVC).

the dual channel AC over the DC outputs, respectively for the reference linear polarizer in parallel and perpendicular directions, and the pre-stretched iPP sample, as defined by Equations (5-12), (5-13), and (5-11). The gain factors of the demodulator were calibrated for all the ratios. Therefore, a normalized PMVLD spectrum of iPP in absorbance unit was calculated from $R_{\parallel,\parallel}$, and $R_{\parallel,\perp}$ and S spectra by using Equation (5-15), and it is shown in Figure 5.16b together with a static VLD spectrum of the same sample. We can see that the PM-based VLD spectrum, as expected, matches the static spectrum very well. The strong VLD effect, as big as 0.4-0.6 absorbance units, was due to the pre-stretch of the iPP sample. Also it should be noted that in this PM-VLD experiment, a polarization modulation amplitude that maximizes spectral intensity at 1100 cm^{-1} was chosen so that optimum modulation was achieved over the region of interest for the iPP sample.

5.6 Polarization modulation vibrational circular dichroism (PM-VCD)

5.6.1 Introduction

Vibrational circular dichroism (VCD) is the differential absorption between left and right circularly polarized light in the infrared region. It is a measurement of vibrational optical activity for chiral molecules. It is a technique that combines the stereochemical sensitivity of natural optical activity with the rich structural content of vibrational (infrared) spectroscopy. The VCD spectral intensity is generally 45 orders weaker than that of regular infrared spectra (10^{-4} and 10^{-5} absorption units), therefore, high sensitivity polarization modulation (PM) is required for VCD measurements.

The polarization modulation/demodulation approach allows direct measurement of the differential VCD signal with the AC detection and dynamic range advantages over the traditional static method, in which subtraction of the two circular polarizations of light (left and right) is required. Experimental VCD measurements were first reported in the early 1970's using a PEM based dispersive spectrometer,[84-86] then followed by an FTIR-VCD system is focused on in the early 1980's.[87] The PM FTIR-VCD system is focused on in this chapter.

The result of a typical VCD measurement includes two vibrational spectra of a sample, the VCD spectrum and its parent infrared absorption spectrum. These can be used together to deduce information about molecular structure. The principal application of VCD is structure elucidation of biologically significant molecules including peptides, polypeptides, proteins, nucleic and amino acids, carbohydrates, natural products and pharmaceutical molecules, as well as chiral molecules of interest to organic or inorganic chemists. It has growing potential as a sensitive, noninvasive diagnostic probe of chiral purity or enantiomeric separation that is critically important in the synthesis and manufacture of chiral drugs and pharmaceutical products. As a result, VCD is becoming an important tool for studying different levels of molecular structures.

5.6.2 VCD theory and spectral interpretation

VCD is defined simply as the difference in the absorbance of a chiral sample between left and right circularly polarized infrared radiation,

$$\Delta A(\sigma) = A_l(\sigma) - A_r(\sigma) \tag{5-16}$$

where σ is wavenumber (cm^{-1}). If the pathlength and concentration are known, VCD can be expressed in terms of the difference in absorptivity according to the well-known Bouguer-Beer-Lambert Law:

$$\Delta\epsilon(\sigma) = \epsilon_l(\sigma) - \epsilon_r(\sigma) \tag{5-17}$$

Optionally, the sign and magnitude of VCD is conveniently expressed as the dimensionless anisotropy ratio g, defined as the ratio of the experimental VCD band absorbance to the experimental infrared band absorbance. This ratio g, can be further expressed theoretically as follows:[88]

$$g = \frac{\Delta A(\sigma)}{A(\sigma)} = \frac{A_L(\sigma) - A_R(\sigma)}{A(\sigma)}$$

$$= \frac{\epsilon_L(\sigma) - \epsilon_R(\sigma)}{\epsilon(\sigma)} = \frac{4\mathrm{Im}(\mu_\alpha m_\alpha)}{\mu_\alpha^* m_\alpha} \tag{5-18}$$

where μ and m are respectively the electric and magnetic dipole transition moments, given in Cartesian component notation. The repeated Greek subscripts are summed over the coordinate directions x, y and z. VCD arises from the combined effect of linear (electric dipole) and circular (magnetic dipole) oscillation of charges during vibrational motion, whereas ordinary infrared absorption is sensitive only to the linear oscillation of charge. The physical process associated with VCD can be illustrated in terms of fundamental transitions between vibrational energy levels of the ground electronic state. VCD is associated with simple one-photon quantum transitions induced by left or right circularly polarized radiation.

VCD spectra can be interpreted on several levels. The simplest is the empirical level, in which VCD features are associated with a region of vibrational frequencies or normal modes of vibration in a molecule of known absolute configuration. A more sophisticated level of empirical analysis is the statistical approach using, for example, principal components (PC) and factor analysis.

In this approach, a set of spectra of samples with known characteristics is used as a training set; these spectra are then reduced to a series of orthogonal PCs of decreasing significance. An unknown spectrum can then be decomposed, or factored, into the set of PCs, and by the relative PC weighting coefficients it can then be correlated with spectra of known structural or conformational features. Beyond empiricism is spectral interpretation by model calculations. The most powerful and successful approach so far to the interpretation of VCD spectra is

through ab initio quantum-mechanical calculations.[88] For molecules with well-defined conformational structures, ab initio VCD calculations can be carried out with excellent correspondence to the experimental spectrum. Better results can be obtained through the use of density functional theory when electron correlation is included.[88]

5.6.3 VCD experiment and data process

VCD spectra can be measured directly on a polarization modulation-based iS50R Research Module configured for VCD analysis. This accessory is coupled with an iS-50R dual-channel FTIR spectrometer. The optical setup of the VCD is similar to that of the VLD as shown in Figure 5.15, with the exception that the focusing lens has a longer focal length. The infrared light source from the spectrometer is directed onto the focus lens of the module, passing through a linear polarizer, a PEM90 operating at 50 kHz, and then through the sample under study. A liquid nitrogen-cooled MCT detector with focus lens assembly is used since it is fast enough to follow the high frequency of polarization modulation. The processing electronics include a dedicated SSD demodulator with a large dynamic range to demodulate the differential signals at the modulation frequency of the PEM (e.g. 50 kHz) and two digitizers recording both the raw (nondemodulated) signal from channel A (I_{DC}) and the demodulated signal from channel B (I_{AC}). Prior to spectral presentation, built-in deHaseth phase correction in OMNIC is used for Fourier transformation.

Since VCD is based on a transmission measurement, Equation (5-16) can then be expressed in terms of transmitted optical intensity for left circularly polarized radiation I_L, and right circularly polarized radiation I_R,

$$\Delta A(\sigma) = A_l(\sigma) - A_r(\sigma) = log_{10}T_R(\sigma) - log_{10}T_L(\sigma)$$

$$\Delta A(\sigma) = \left(2/ln10\right)\left[\left(I_R(\sigma) - I_L(\sigma)\right)/\left(I_R(\sigma) + I_L(\sigma)\right)\right]$$

(5-19)

where relationships $T = I/I_0$, $I_L \approx I_R \approx 1/2(I_L + I_R)$, and $\ln(1 + x) \approx x$ when x is approaching zero, is used.

In the dual-channel VCD experiment, the simultaneously recorded DC and AC single beams of a sample are represented by the following two equations:

$$I_{DC}(\sigma) = 1/2\left[I_R(\sigma) + I_L(\sigma)\right]$$

(5-20)

$$I_{AC}(\sigma) = \left[I_R(\sigma) - I_L(\sigma)\right]J_1\left[\alpha_M^0(\sigma)\right]exp(-2v\sigma\tau)$$

(5-21)

where v is mirror velocity of the FTIR interferometer, τ is the time constant of the lock-in amplifier or the demodulator used in the experiment, and $J_1[\alpha_M{}^0(\sigma)]$ is the first order Bessel function that describes the wavenumber dependent PEM modulation efficiency. Substituting the ratio of Equation (5-21) over Equation (5-20) into Equation (5-19) gives the theoretical expression for the VCD raw spectrum of a sample,

$$\left[I_{AC}(\sigma)/I_{DC}(\sigma)\right]_{SAM} = \left(ln10\right)J_1\left(\alpha_M^0(\sigma)\right)exp(-2v\sigma\tau)\Delta A(\sigma)$$

(5-22)

The final VCD spectrum can be obtained after a VCD calibration spectrum is collected using a multiple quarter waveplate (CdSe) with axes parallel or perpendicular to the stress axis of the PEM followed by a second polarizer (KRS5 or ZnSe) oriented parallel or perpendicular to the linear polarizer placed before the PEM. The arrangement of optical components for measuring the VCD calibration curve is illustrated in Figure 5.18.

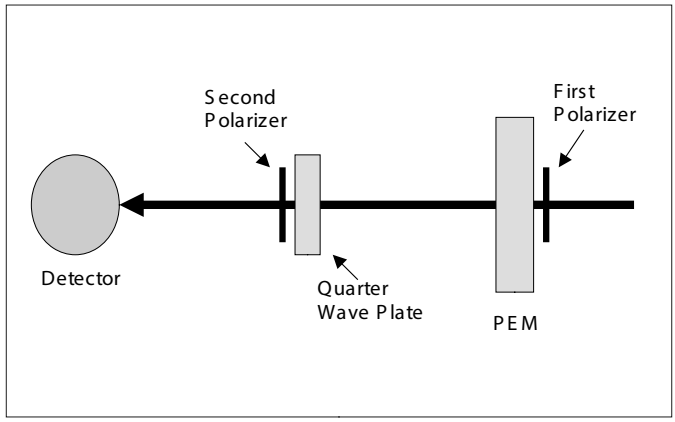

Figure 5.18. Optical setup for VCD calibration curve measurement.

These four possible settings for the waveplate and the second polarizer (or practically speaking, two settings corresponding to the two different directions of the second polarizer would be enough) produce 4 VCD "curves" and the intersection points of the curves define a calibration plot given by Equation (5-23):[89]

$$\left[I_{AC}(\sigma)/I_{DC}(\sigma)\right]_{CAL} = \pm J_1\left[\alpha_M^0(\sigma)\right]exp(-2v\sigma\tau)$$

(5-23)

Ratioing Equation (5-22) over (5-23) then gives,

$$\Delta A(\sigma) = 0.8686\left[I_{AC}(\sigma)/I_{DC}(\sigma)\right]_{SAM}/\left[I_{AC}(\sigma)/I_{DC}(\sigma)\right]_{CAL}$$

(5-24)

where only the positive sign in Equation (5-23) is used. In VCD experiments, usually the AC channel signal is amplified with a gain factor for both the VCD sample (GS) and calibration (GC) measurements, thus Equation (5-24) can be adjusted to:

$$\Delta A(\sigma) = 0.8686\left[I_{AC}(\sigma)/G_S I_{DC}(\sigma)\right]_{SAM}/\left[I_{AC}(\sigma)/G_C I_{DC}(\sigma)\right]_{CAL}$$

(5-25)

Equation (5-25) is thus used to convert experimental VCD spectral ratios to absorbance units with proper intensity calibration that removes the effects of both Bessel function characteristics of the photoelastic modulation and the exponential decay of the demodulator.

5.6.4 Application Examples

VCD can be used for a wide variety of stereo-structural analyses.89 The applications of VCD fall into three areas. The first and also the oldest area since the mid 1970's was to study conformational properties of molecules where the absolute configurations were well known. The examples of this application include some typical biological molecules such as proteins, nucleic acids and sugars. The other two areas are more practical applications in the chemical and pharmaceutical industries. The interest in the potential of using VCD to determine the optical purity of manufactured samples and the absolute configuration of new chiral molecules intended for medicinal applications has been increasing over the last several years.

In this section, only two kinds of classic chiral molecules used in VCD measurement are demonstrated, which are αpinene, S- or R-camphors. Both samples can produce well-defined VCD

spectra, and therefore, they are often used for testing the performance of VCD instruments.

Shown in Figure 5.19 are: a) the VCD calibration intensity calibration curve that was generated from the raw VCD spectra of the quarter waveplate, corresponding to the parallel and perpendicular directions of the second polarizer; and (b) regular absorbance spectrum and intensity calibrated VCD spectrum of (1R)-(-)-αpinene (98%, $C_{10}H_{16}$, Aldrich® Chemical Company) in absorbance units. These spectra were measured by using a Thermo Scientific research-grade spectrometer coupled with a PEM-IRRAS accessory configured for VCD analysis. The VCD intensity calibration was performed by using Equation (5-25).

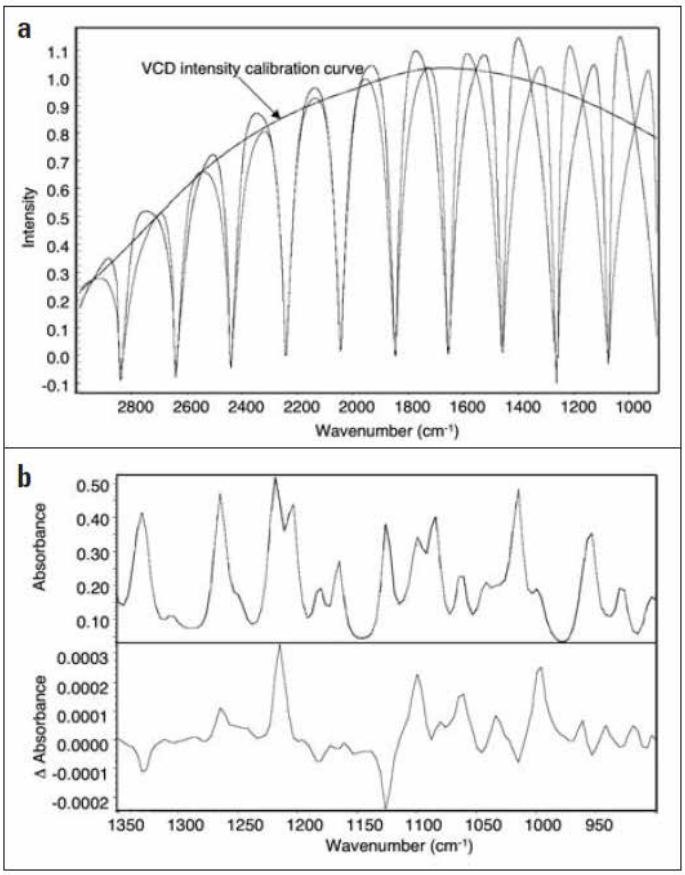

Figure 5-19. a) VCD intensity calibration curve generated from the two VCD spectra of the quarter waveplate corresponding to the parallel and perpendicular directions of the second polarizer; b) regular absorbance spectrum and intensity calibrated VCD spectrum of (1R)-(-)-α-pinene measured with the Research Module in the VCD configuration.

In this VCD experiment, a liquid transmission cell (BaF_2) with pathlength of 50 micrometers was used so that the α-pinene sample can be measured directly without dilution. Under these conditions, spectral saturation over 800 – 1350 cm^{-1} region is generally avoided, and active bands are less than 0.7 absorbance unit, ensuring the linearity required for VCD measurement. Since the VCD signal is on the level of micro-absorbance unit, a large number of scans (typically 1,000 or above) is often needed to improve the signal to noise ratio. Another example of VCD measurement is based on S- and R- camphors. Figure 5.20 illustrates how VCD can be used to distinguish between these two molecules. These two mirror-image molecules also have “mirror-image” VCD spectra whereas their regular IR spectra are virtually identical.

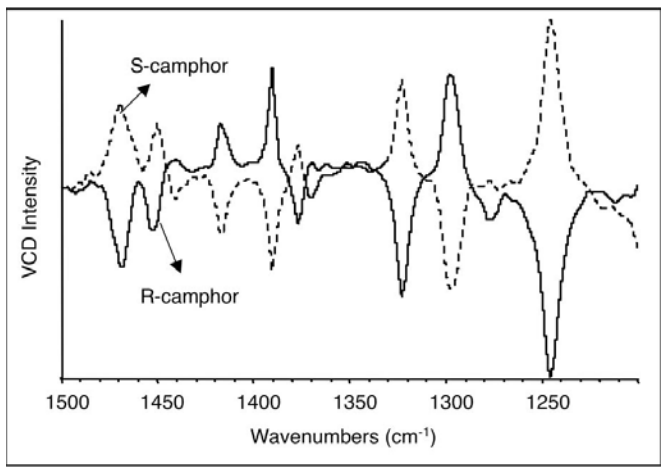

Figure 5.20. VCD spectra of S- and R-camphors. *Data courtesy of Laurance Nafie of Syracuse University, Syracuse, NY.*

Chapter 6:
Two-Dimensional Infrared (2DIR) Correlation Spectroscopyy

6.1 Introduction

Two-dimensional infrared (2DIR) spectroscopy is a spectro-mathematical tool that correlates spectra synchronously and asynchronously in a third dimension defined by a physical parameter in a dynamic system under study. The conventional 2DIR correlation method, proposed in 1990 by Noda, strictly applies to the analysis of a system with a sinusoidal perturbation,[90] where two orthogonal in-phase and quadrature spectra are correlated in a third dimension, i.e. the phase angle. Typical application examples of conventional 2DIR correlation spectroscopy include analysis of the responses of polymer films to mechanical strain[90, 91-93] and the responses of liquid crystals to electric fields.[45,94,95] However, the ambiguities of the conventional 2DIR method, particularly, in situations of phase difference around 45°, and the strict condition on perturbation have limited its application to many systems.[32]

The generalized 2D spectral correlation formalism, based on an arbitrary perturbation waveform, was proposed in 1993.[96] The generalized 2DIR correlation algorithm can be applied to a series of spectra collected over any physical variable, and much broader applications have been reported in many areas of research. These include reaction process studies of photopolymerization,[97] temperature-dependent behaviors of self-associated molecules,[98-101] photoacoustic depth profiling of laminate materials,[36,40] heterogeneous samples with concentration continuously varying components,[102] conformational changes and specific interactions in polymer blends,[103] hetero-spectral correlation analysis of infrared and Raman spectra of N-methylacetamide in the pure liquid state,[104] and many other spectroscopic applications areas. In this chapter, 2DIR theory will be briefly introduced, with a few application examples focusing on the use of generalized 2DIR correlation spectroscopy.

6.2 2DIR theory

The conventional 2DIR correlation spectra are generated from two orthogonal in-phase (I) and quadrature (Q) spectra. The definitions for conventional synchronous (Φ) and asynchronous (Ψ) spectral correlation intensities between wavenumbers $\sigma 1$ and $\sigma 2$ are expressed by the following two equations:

$$\Phi(\sigma_1,\sigma_2) = 1/2\left[I(\sigma_1)Q(\sigma_2) + Q(\sigma_1)I(\sigma_2)\right] \quad \text{(6-1)}$$

$$\Psi(\sigma_1,\sigma_2) = 1/2\left[Q(\sigma_1)I(\sigma_2) - I(\sigma_1)Q(\sigma_2)\right] \quad \text{(6-2)}$$

Alternatively, Equations (6-1) and (6-2) can be rewritten in terms of magnitude [$M = (I^2+Q^2)^{1/2}$] and phase [ρ = arc tan (Q/I)] spectra:

$$\Phi(\sigma_1,\sigma_2) = 1/2M(\sigma_1)M(\sigma_2)cos\left[\theta(\sigma_1) - \theta(\sigma_2)\right] \quad \text{(6-3)}$$

$$\Psi(\sigma_1,\sigma_1) = 1/2M(\sigma_1)M(\sigma_2)sin\left[\theta(\sigma_1) - \theta(\sigma_2)\right] \quad \text{(6-4)}$$

As elucidated previously,[32,44] the tedious and lengthy interpretation rules of conventional 2DIR correlation spectroscopy can be intuitively deduced from the above two equations, because the critical dynamic spectral information, phase angle, is directly involved. The synchronous correlation spectrum highlights the coherence of dynamic IR signal changes at two different wavenumbers (or peak regions). A strong correlation on the synchronous correlation spectrum shows that the changes at those two wavenumbers occur almost synchronously [$\theta(\sigma 1)$–$\theta(\sigma_2)$ is small, approaching zero] with each other. The positive correlation means they change in the same direction and the negative correlation means they change in the opposite direction. In contrast, the asynchronous correlation spectrum highlights the uncoordinated or independent changes of IR signals at two different wavenumbers. A strong correlation on the asynchronous spectrum shows that the changes at those two wavenumbers are almost out of phase, [$\theta(\sigma_1)$-$\theta(\sigma_2)$ is big, approaching 90°].

In generalized 2DIR correlation spectroscopy, we observe and record time-dependent spectral intensity variation $\tilde{Y}(\sigma, t)$ at wavenumbers σ, for a period of time between T_{min} and T_{max}. Then the synchronous and asynchronous correlation intensities between $\sigma 1$ and $\sigma 2$, A ($\sigma 1$, $\sigma 2$) and C ($\sigma 1$, $\sigma 2$), for a generic perturbation waveform, are defined by:

$$\Phi(\sigma_1,\sigma_2) + i\Psi(\sigma_1,\sigma_2) = 1/\left[\pi(T_{max} - T_{min})\right]\int_0^\infty \tilde{Y}_1(\omega)\tilde{\bar{Y}}_2^c(\omega)d(\omega) \quad \text{(6-5)}$$

where $\tilde{Y}(\omega)$ is the Fourier transform of $\tilde{Y}(\sigma_1, t)$ in the varying physical parameter domain and $\tilde{\bar{Y}}_2^c(\omega)$ is the corresponding conjugate of the Fourier transform with a Fourier frequency of ω. Thus the generalized 2D correlation spectra can be obtained from any time-dependent spectra having an arbitrary waveform, as long as the Fourier transform of the time-dependence can be calculated for the intensity changes at each wavenumber. The parameter "time" can be replaced with any other physical perturbation in the system, such as mechanical strain, electric voltage, and optical excitation, etc. as shown in Figure 6.1.

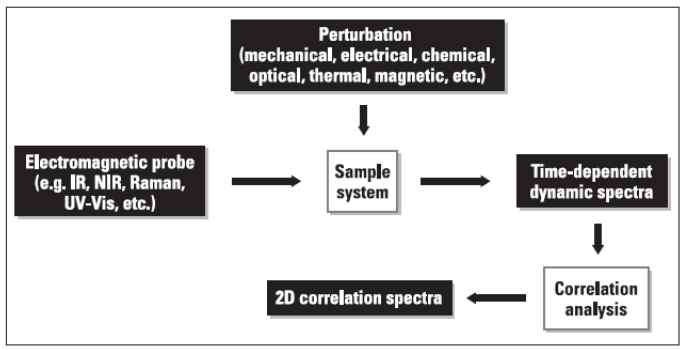

Figure 6-1. Perturbations of arbitrary waveform to sample system in generalized 2D-IR spectroscopy.

Although the generalized 2D algorithm developed by Noda was used in the OMNIC software, the simplified version of the algorithm proposed by Burie[105] offers an easy formula to understand generalized 2D data process. According to Burie, a generalized 2D asynchronous correlation (disrelation) spectrum, C (σ_1, σ_2), between wavenumber σ1 and σ2, can be calculated from N spectra taken at N different times (t_i or t_j or any other parameter) with peak intensities of y (σ_1, t_i or t_j) by using the following formula:

$$\left|\left(\Psi(\sigma_1,\sigma_2)\right)\right| = 1/(N-1)\sqrt{\sum_{i=1}^{N}\sum_{j>1}^{N}\left[y(\sigma_1,t_i)\cdot\left(y\left(\sigma_2,t_j\right)\right)-y\left(\sigma_1,t_j\right)\cdot y(\sigma_2,t_i)\right]^2}$$

(6-6)

The sign of Ψ (σ_1, σ_2) is chosen in such a way that: Ψ (σ_1, σ_2) $[dC(t)/dt]_{t=t0} \geq 0$ where C (t) is the cross-correlation function.[96] The interpretation of generalized 2D correlation spectra generated from a series of exponentially decaying spectra is relatively straightforward. A positive synchronous 2D correlation contour indicates that the decay processes of spectral intensities of a band pair (σ_1, σ_2) (corresponding to a reading on the x-or y-axis respectively) occur at rates similar to each other and in the same direction, whereas a negative synchronous 2D correlation contour means that the process or change occurred in the opposite direction, though at similar rates. A positive asynchronous correlation contour indicates the decay rates of the spectral intensities at the band pair (σ_1, σ_2) are different, and that the intensity change at σ_1 is faster than that at σ_2, whereas a negative asynchronous correlation contour means the opposite, i.e. the change at σ_2 is faster than that at σ_1.

6.3 Applications of 2DIR spectroscopy

6.3.1 Photoacoustic spectral depth-profiling of laminate materials

The conventional 2D spectral correlation analysis based on the use of the two orthogonal spectra (in-phase and quadrature) has been applied to photoacoustic depth profiling analysis as reported previously.[32, 111,112] The ambiguities of this conventional 2D method, particularly for situations of phase difference around 45°, has limited its further applications in depth profiling analysis as discussed in the literature. The direct use of the magnitude and phase spectra would be more effective. However the use of the generalized 2D correlation algorithm, readily available in the OMNIC software, offers unique features and advantages over other depth profiling methods. These include simplifying the photoacoustic phase modulation experiment and 2D correlation analysis rules, avoiding phase-related negative band ambiguities, and enhancing spectral and depth resolutions.

Generalized 2D photoacoustic correlation spectra can be calculated from a series of spectra collected at different modulation frequencies. In FTIR PAS, these spectra can be collected by varying phase modulation frequency in step-scan phase modulation mode. A series of photoacoustic magnitude spectra are used as input for the generalized 2D software in the order of increasing infrared modulation frequency. Since the photoacoustic signal intensity decreases as modulation frequency increases (in the absence of signal saturation), all generalized 2D PAS synchronous contours must be positive according to the theory.[96] This important feature simplifies the generalized 2D PAS analysis rules, making the interpretation more straightforward than conventional 2D spectral analysis.

Subsequently, a positive asynchronous generalized 2D PAS correlation contour at σ_1/σ_2 (σ_1 = wavenumber on x-axis and σ_2 = wavenumber on y-axis) means that the intensity variation (attenuation) at σ_1 occurs before that at σ_2, i.e. the spatial origin for σ_1 is deeper than that for σ_2; and a negative asynchronous generalized 2D PAS correlation contour means the opposite, i.e. the spatial origin for σ_1 is shallower than that for σ_2. Since contours on an asynchronous spectrum are symmetrically located on both sides of the diagonal with opposite signs, using either half of the 2D contour map (top left or bottom right) is sufficient for spectral correlation analysis and the same rules stated above apply to all contours in the map. Successful applications of generalized 2D correlation on step-scan photoacoustic depth profiling analysis have been reported on analysis of multilayered samples such as a two-layer sample, 1μm polystyrene on 100μm mylar,[113] and a four-layer sample, 10μm polyethylene on 10μm polypropylene, on 6μm polyethylene terephthalate, on 6mm polycarbonate.40 Not only can the order of layers be unambiguously distinguished, but the spectral (and thus depth) resolution can be enhanced as shown on the asynchronous correlation spectrum, where the one dimensional polyethylene peak at 1462 cm^{-1} is split into two new 2D peaks at 1450 and 1469 cm^{-1} respectively. The reason for this "splitting" is that both the surface layer (polyethylene) and the second layer (polypropylene) contribute to the peak. This spectral detail was obscured in the one-dimensional photoacoustic spectra.

6.3.2 Microscopic analysis of samples with concentration continuously varying components

Characterization of samples or materials with concentration continuously varying components has been of importance in both research and production in many fields. Recent developments in modern FTIR microscopic mapping and imaging allows easy analysis of samples with thicknesses ranging from a few microns to centimeters. The generalized 2D correlation spectroscopy provides a method to fully elucidate the relatively small changes and different rates of concentration variation along a spatial direction of interest.

One application example of generalized 2DIR for this type of sample is the oxidation profile analysis of a weathered polyethylene electric insulator.[102] An electrical short results from failed insulating material, which becomes conductive with exposure to the atmosphere for an extensive time. Thus it is important to determine the compositional changes across the depth to characterize the weathering effect on this material. The concentration profile of the oxidized component of a weathered electric insulator was studied by using the microscopic line

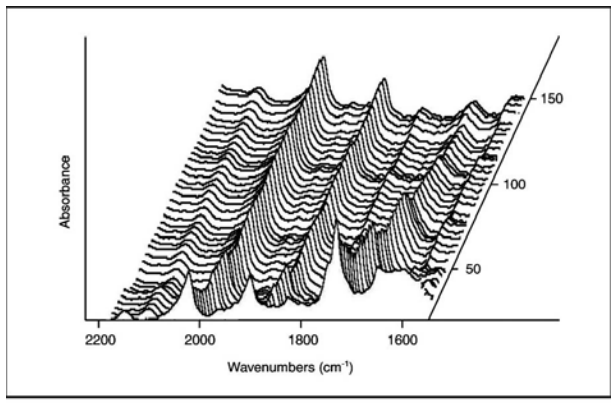

Figure 6-2. Spectra of the weathered insulator from the surface to 150 μu deep into the sample, collected by FTIR microscopic line mapping.

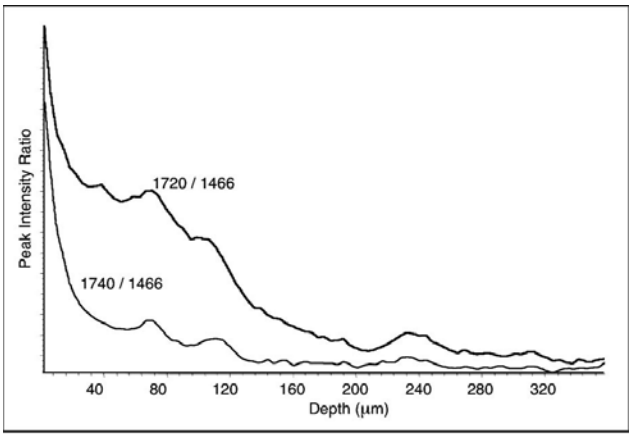

Figure 6-3. Peak intensity ratio profiles for carbonyl bands (around 1740 and 1720 cm^{-1}) over polyethylene band 1466 cm^{-1}.

mapping technique on a Thermo Scientific Continuµm™ IR microscope. Space-resolved FTIR spectra of the weathered electric insulator from the surface to a depth of 150 µm are shown in Figure 6.2. It can be seen that the carbonyl bands at 1740 and 1720 cm^{-1} from the oxidized component extend deeply into the sample and their intensities continuously decrease as the depth increases. This profile is clearly demonstrated by Figure 6.3 where the normalized peak intensity of the carbonyl bands is plotted as a function of depth into the sample. The oxidation extends to about 325 microns as can be seen from the C=O band intensity. It is very visible that within the top 85 µm surface portion of the sample the component associated with the band at 1740 cm^{-1} changes its concentration across the depth faster than that associated with the band at 1720 cm^{-1}.

The dynamic change (concentration variation) associated with the carbonyl bands can be observed from generalized 2D analysis. Illustrated in Figure 6.4, the generalized asynchronous 2D correlation spectrum of the space-resolved FTIR microscopic line mapping spectra were generated from 21 spectra by using the OMNIC generalized 2Dcorrelation routine. These 21 spectra were collected from the surface to a depth of 84 µm with spatial resolution of 4 mm and spectral resolution of 0.5 cm^{-1} (after zero filling). They were all normalized against the polyethylene band at 1466 cm^{-1} to eliminate the thickness effect before being input into the 2D correlation analysis routine.

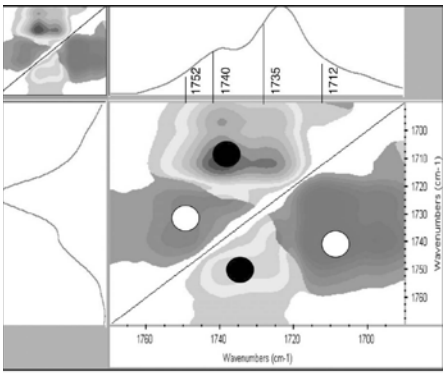

Figure 6-4. Generalized asynchronous 2D correlation spectrum of space-resolved FTIR microscopic spectra. A ● indicates a positive contour and a ○ indicates a negative contour.

The asynchronous correlation spectrum shown in Figure 6.4 illustrates some features of band splitting. Thus details of spectral intensity variation can be obtained from the correlation analysis. The very strong positive cross contour between bands 1740 and 1712 cm^{-1} indicates that the rate of intensity change of band 1740 cm^{-1} is faster than that of 1712 cm^{-1}. Thus the component with 1740 cm^{-1} band decreases its concentration from the surface to the deep part of the sample more quickly than that with 1712 cm^{-1}. However a negative cross contour is seen between bands 1752 and 1735 cm^{-1}, indicating that the former changes its intensity more slowly than the latter. This 2D correlation analysis not only confirms the profile based on the straightforward intensity extraction as shown in Figure 6.3, but it also elucidates much more spectral, and thus chemical compositional, details than the conventional, one-dimensional spectral approach.

6.3.3 Other applications

Applications of 2D correlation spectroscopy have become active with both hardware and software improvement in modern instrumentation for dynamic spectroscopic studies. One of the highlighted events was the first International Symposium on Two-Dimensional Correlation Spectroscopy (2DCOS) held in Sanda, Japan in 1999.[114] Numerous applications of 2D correlation spectroscopy reported to date include a wide range of research work to better understand polymers, liquid crystals, chemical reactions, proteins and biological systems, using electromagnetic radiation probes, such as mid-IR, near-IR, Raman, fluorescence, and electron spin transient nutation spectroscopy. Hetero-spectral correlation analysis between different spectroscopic techniques has been investigated. Other perturbations such as thermal effects, pressure variation, etc. also have been used in 2D spectral correlation analysis.

6.4 Limitations of 2D correlation spectroscopy

As discussed previously, the significant advantages and power of 2D spectral correlation analysis are its effective enhancement of spectral resolution and detailed elucidation of the dynamic behavior of spectral intensity variation in a perturbation-dependent dynamic system, particularly with the analysis of the generalized asynchronous correlation spectra. However, caution must be taken when utilizing 2DIR to avoid either over interpretation of the correlation spectra or ambiguities of the results. First, there are special cases where the Hilbert transform of a dynamic signal (in order to generate asynchronous correlation) does not apply to two signals with totally different shapes in a system – the asynchronous correlation under this condition would be zero;[115] Secondly, new “peaks” generated in the 2D correlation, in some cases may reveal true fine spectral structure, while in others could be totally artificial (mathematical) without physical meaning. Thirdly, particularly in conventional 2D correlation analysis, 2D contours are a combined picture of both signal magnitude and phase; therefore, all the quantitative phase information is naturally hidden in the beauty of the 2D contours, while the direct use of phase and magnitude spectra would provide more quantitative distinctions between dynamic signals. Furthermore, when the phase difference between two bands is neither nearly negligible (approaching zero), nor significantly out of phase (close to 90° difference), both the conventional synchronous and asynchronous spectra will show similar cross peaks. In photoacoustic depth profiling analysis of a multilayered sample, for example, the conventional 2D correlation method will encounter more difficulties, because bands of different layers with phase differences close to 45° will show similar correlation in both synchronous and asynchronous spectra, and the order of the layers is usually hard to determine from the 2D spectra, therefore the generalized 2D approach with the use of magnitude spectra at different modulation frequencies is highly recommended for this application.

Bibliography

1. A. A. Michelson, *Phil. Mag.* 31 (5), 256 (1891).
2. P. R. Griffiths, J. A. deHaseth, "*Fourier Transform Infrared Spectroscopy",* John Wiley & Sons, New York, 11, (1986).
3. E. Y. Jiang, *Spectroscopy*, 17 (1), 22 (2001).
4. 4. J. Chamberlain, "*The Principle of Interferometric Spectroscopy",* John Wiley & Sons, New York, (1979).
5. Spectral resolution test data for iS50R spectrometers (also see Thermo Scientific iS50R Spectrometer Brochure, P/N PS522330_E 1029 M (2020) .
6. W. Shifu and K. Kempfert, *"Applications of Rapid-scan Data Collection."* Thermo Scientific Application Note: AN9584, Madison, WI (1995).
7. R. J. Rosenthal, *"Application of Fourier Transform Infrared Rapid Scan Techniques to Photochemical Investigations."* Mikrochim. Acta I, 273 (1988). (Thermo Scientific Reprint6, Madison, WI).
8. K. Kempfert and E. Y. Jiang,*"Fourier Transform Infrared Spectrometer Requirements for FarInfrared Data Collection."* Thermo Scientific Application Note: AN01129, Madison, WI (2001).
9. https://www.thermofisher.com/order/catalog/product/840-210800?icid=MSD_SPEC_UV-VisVisSelectionGuide#/840-210800?icid=MSD_SPEC_UV-VisVisSelectionGuide
10. Leimer and K. Kempfert, *"Optimizing Optical Bench Performance for Near-IR and Visible Spectroscopy."* Thermo Scientific Technical Note: TN9580, Madison, WI (1995).
11. M. J. Smith, C. J. Manning, R. A. Palmer and J. L. Chao, Appl. Spectrosc., 42, 546 (1988).
12. R. W. Jones and J. F. McClelland, Appl. Spectrosc., 50, 1258 (1996).
13. C. J. Manning and P. R. Griffiths, Appl. Spectrosc., 47, 1345 (1993).
14. D. L. Drapcho, R. Curbelo, E. Y. Jiang, R. A. Crocombe and W. J. McCarthy, Appl. Spectrosc., 51, 453 (1997).
15. R. Curbelo, *Fourier Transform Spectroscopy, Proceedings of the 11th International Conference on Fourier Transform Spectroscopy*, Edited by J. A. deHaseth, AIP Proceedings 430, 74 (1997).
16. R. Hapanowicz, *Laser Focus World*, July (1996). (Thermo Scientific Reprint94).
17. R. A. Palmer, *Spectroscopy*, 8 (2), 26 (1993).
18. A. G. Bell, Am. *J. Sci.*, 20, 305 (1880).
19. A. Rosencwaig and A. Gersho, *Science*, 190, 556 (1975).
20. A. Rosencwaig and A. Gersho, *J. Appl. Phys*., 47, 64 (1976).
21. R. A. Palmer, *Photoacoustics and Photothermal Spectroscopies*, in Determination of Electronics and Optical Properties, Edited by B. W. Rossiter and Roger C. Baetzold. Physical Methods of Chemistry Series, 2nd ed., Vol. VIII. 61. John Wiley & Sons, Inc. (1993).
22. E. Y. Jiang, R. A. Palmer and J. L. Chao, *J. Appl. Phys.*, 78, 460 (1995).
23. G. Mead, S. R. Lowry, D. W. Vidrine and D. R. Mattson, Proc. IEEE 4th Int. Conf. *Infrared and Millimeter Waves and their Applications*, 231 (1979).
24. M. G. Rockley, *Chem. Phys.* Lett., 68, 455 (1979).
25. W. Vidrine, in *Fourier Transform Infrared Spectroscopy*, Vol. 3, Eds. J. R. Ferraro and L. J. Basile, Academic Press, New York, 125148 (1982).
26. K. Krishnan, S. Hill, J. P. Hobbs, and C. S. P. Sung, Appl. *Spectrosc.*, 36, 257 (1982).
27. C. J. Manning, R. M. Dittmar, J. L. Chao and R. A. Palmer, *Infrared Physics*, 33, 53 (1992).
28. R. A. Palmer and R. M. Dittmar, *Thin Solid Films, Section A*, 223, 31 (1993).
29. R. A. Palmer, E. Y. Jiang and J. L. Chao, *Proc. SPIE* 2089, 250 (1993).
30. R. A. Palmer and E. Y. Jiang, *J. Phys.* IV, 4 (July), C7337 (1994).
31. R. A. Palmer, E. Y. Jiang, and J. L. Chao, Mikrochim. Acta [Suppl.] 14, 591 (1997).
32. E. Y. Jiang and R. A. Palmer, *Anal. Chem.*, 69 (10), 1931 (1997).
33. E. Y. Jiang, R. A. Palmer and N. Morosoff, *Appl. Spectrosc.*, 51, 1238 (1997).
34. R. W. Jones and J. F. McClelland, *Appl. Spectrosc.*, 50, 1258, (1996).
35. J. F. McClelland, R. W. Jones, S. J. Bajic and J. F. Power, Mikrochim. *Acta* [Suppl.] 14, 613614 (1997).
36. E. Y. Jiang, W. J. McCarthy and D. L. Drapcho, *Spectroscopy*, 13 (2), 2140 (1998).
37. R. M. Dittmar, J. L. Chao and R. A. Palmer, *Appl. Spectrosc.*, 45, 1104 (1991).
38. B. O. Budevska and C. J. Manning, *Appl. Spectrosc.*, 50, 939 (1996).
39. E. Y. Jiang and M. J. Smith, *"Characterization of Polymer Laminates by Time-resolved Step-scan FTIR Photoacoustic Spectroscopy (TRS2 FTIRPAS)."* Thermo Scientific Application Note: AN01127, Madison, WI (2001).
40. E. Y. Jiang, W. J. McCarthy, D. L. Drapcho, and R. A. Crocombe, *Appl. Spectrosc.*, 51 1736 (1997).
41. L. Burggraf and D. E. Leyden, *Anal. Chem.*, 53, 759 (1981).
42. J. F. McCleland, *Anal. Chem.*, 55, 89A (1983).
43. R. O. Carter III, *Appl. Spectrosc*., 46, 219 (1992).
44. E. Y. Jiang, Ph.D. Dissertation (Duke University, Durham NC, USA), 87 (1995).
45. R.W. Jones and J.F. McClelland, *Appl. Spectrosc.*, 56, 409 (2002).

46. T. Nakano, T. Yokoyama, and H. Toriumi, *Appl. Spectrosc.*, 47 (9), 1354 (1993).
47. S. E. Plunkett, J. L. Chao, T. J. Tague, and R. A. Plamer, *Appl. Spectrosc.*, 49, 702 (1995).
48. M. Shim, S. V. Shilov, M. S. Braiman, and P. GuyotSionnest, *J. Phys. Chem.*, B104, 1494 (2000).
49. X. Z. Sun, S. M. Nikiforov, J. Yang, C. S. Colley and M. W. George, *Appl. Spectrosc.*, 56 (1), 31 (1997). (Thermo Scientific Reprint –134, Madison, WI).
50. S. Williams, T. P. Causgrove, R. Gilmanshin, K. S. Fang, R. H. Callender, W. H. Woodruff, B. R. Dyer, *Biochemistry*, 35, 691 (1996).
51. C. Y. Huang, J. W. Klemke, Z. Getahun, W. F. DeGrado, and F. Gai, *J. Am. Chem. Soc.*, 123, 9235 (2001).
52. C. Y. Huang, Z. Getahun, T. Wang, W. F. DeGrado, and F. Gai, *J. Am. Chem. Soc.*, 123, 12111 (2001).
53. S. E. Bromberg, H. Yang, M. C. Asplund, T. Lian, B.K. McNamara, Kotz, J. S. Yeston, M.Wilkens, H. Frei, R. G. Bergman, and B. Harris, Science, 278, 260 (1997).
54. E. Kauffmann, H. Frei, and R. A. Mathies, *Chem. Phys. Lett.*, 266, 554 (1997).
55. R. Rammelsberg, S. Boulas, H. Chorongiewski, and K. Gerwert, *Vibra. Spectrosc.*, 19, 143 (1999).
56. J. R. Schoonover, G. F. Strouse, and R. B. Dyer, *Inorg. Chem.*, 35, 273 (1996).
57. P. Y. Chen, R. A. Palmer, and T. J. Meyer, *J. Phys. Chem. A*, 102, 3042 (1998).
58. P. Y. Chen, R. A. Palmer, *Appl. Spectrsoc.*, 51 (4), 580 (1997).
59. J. Eberhard, P. S. Yeh, and Y. P. Lee, *J. Phys. Chem.*, 107 (16), 6499 (1997).
60. S. V. Shilov, S. Okretic and H. W. Siesler, Vibra. *Spectrosc.*, 9, 57 (1995).
61. X. Hu, H. Frei, and T. G. Spiro, *Biochem.*, 35 (40), 13001 (1996).
62. W. Uhmann, A. Becker, C. Taran and F. Siebert, *Appl. Spectrosc.*, 45 (3), 390 (1991).
63. W. Hage, M. Kim, H. Frei and R. A. Mathies, *J. Phys. Chem.*, 100, 16026 (1996).
64. H. Kandaori, Y. Yamazaki, M. Hatanaka, R. Needleman, L. Brown, H. Richter, J. Lanyi and A. Maeda, *Biochem.*, 36 (17), 5134 (1997).
65. J. Umemura, *"ReflectionAbsorption Spectroscopy of Thin films on Metallic Substrates,"* in the *"Handbook of Vibrational Spectroscopy,"* Eds., J. M. Chalmers, P. R. Griffith, John Wiley & Sons, Ltd., Chichester, UK, Vol. 2, 982 (2001).
66. T. Buffeteau, B. Desbat, J. M. Turlet, *Appl. Spectrosc.*, 45, 380 (1991).
67. B. L. Frey, R. M. Corn and S. C. Weibel, *"PolarizationModulation Approaches to ReflectionAbsorption Spectroscopy,"* in the *"Handbook of Vibrational Spectroscopy,"* Eds., J. M. Chalmers, P. R. Griffith, John Wiley & Sons, Ltd., Chichester, UK, Vol. 2, 1042 (2001).
68. http://corninfo.chem.wisc.edu/writings/ftir2.html
69. P. Y. Chen, M. J. Smith and B. Garland, *American Laboratory*, 32 (22), 36 (2000).
70. J. Cui, B. Marchon, *J. Appl. Phys.*, 78, 4206 (1985).
71. C. M. Mate, *J. Appl. Phys.*, 72, 3084 (1992).
72. C. M. Mate, *Data Storage*, Jul./Aug., 45 (1997).
73. M. Yang, F. E. Talke, D. J. Perettie, T. A. Morgan, K.K. Kar, *IEEE Trans Magn.*, 30, 4143 (1994).
74. Marc Porter, Iowa State University, Ames, Iowa, Private Communications.
75. I. Noda, A. E. Dowrey and C. Marcott, *Appl. Spectrosc.*, 42, 203 (1988).
76. L. A. Nafie and M. Diem, *Appl. Spectrosc.*, 33, 130 (1979).
77. L. A. Nafie, and D. W. Vidrine, *"Double Modulation Fourier Transform Spectroscopy in Fourier Transform Infrared Spectroscopy, Techniques using Fourier Transform Interferometry,"* Eds. J.R. Ferraro, and L. J. Basile, Academic Press, NY, 3, 83123 (1982).
78. C. Marcott, *Appl. Spectrosc.*, 38, 442 (1984).
79. V. Abetz, G. G. Fuller and R. Stadler, Makronmol. *Chem. Macromol. Symp.,* 52, 23 (1991).
80. T. Buffeteau, B. Desbat, M. Pézolet and J.M. Thurlet, *J. Phys. Chem.*, 90, 1467 (1993).
81. T. Buffeteau, and M. Pézolet, *Appl. Spectrosc.*, 50, 948 (1996).
82. M. Pézolet, C. Pellerin, R. E. Prud'homme and T. Buffeteau, *Vibra. Spectrosc.*, 18, 103 (1998).
83. T. Buffeteau, and M. Pézolet, *"Linear Dichroism in Infrared Spectroscopy,"* in the *"Handbook of Vibrational Spectroscopy,"* Eds., J. M. Chalmers, P. R. Griffith, John Wiley & Sons, Ltd., Chichester, UK, Vol. 1, 693 (2001).
84. G. Holzwarth, E. C. Hsu, H. S. Mosher, T. R. Faulkner, A. Moscowitz, *J. Am. Chem. Soc.*, 96, 251 (1974).
85. L. A. Nafie, J. C. Cheng, P. J. Stephens, *J. Am. Chem. Soc.*, 97, 3842 (1975).
86. L. A. Nafie, T. A. Keiderling, P. J. Stephens, *J. Am. Chem. Soc.*, 98, 2715 (1976).
87. E. D. Lipp, C. G. Zimba, L. A. Nafie, *Chem. Phys. Lett.*, 90, 15 (1982).
88. L. A. Nafie, Appl. *Spectrosc.*, 50 (5), 14A26A (1996).
89. R. K. Dukor and L. A. Nafie, *"Vibrational Optical Activity of Pharmaceuticals and Biomolecules,"* in *Encyclopedia of Analytical Chemistry*, Ed. R. A. Meyers, 662676, John Wiley & Sons Ltd, Chichester, UK (2000).
90. I. Noda, *Appl. Spectrosc.*, 44, 550 (1990).
91. C. Marcott, A. E. Dowrey, and I. Noda, *Appl. Spectrosc.*, 47, 1324 (1993).
92. A. Singhal and L. Fina, *Appl. Spectrosc.,* 49, 1073 (1995).
93. R. A. Ingemey, G. Strohe and W. S. Veeman, Mikrochim. *Acta [Suppl.]* 14, 607 (1997).

94. R. Hasegawa, M. Sakamoto, H. Sasaki, *Appl. Spectrosc.*, 47, 1386 (1993).

95. H. Sasaki, M. Ishibashi, A. Tanaka, N. Shibuya and R. Hasegawa, *Appl. Spectrosc.*, 47, 1390 (1993).

96. I. Noda, *Appl. Spectrosc.*, 47, 1329 (1993).

97. T. Nakano, S. Shimada, R. Saitoh and I. Noda, *Appl. Spectrosc.*, 47, 1337 (1993).

98. I. Noda, Y. Liu, Y. Ozaki and M. Czarnecki, *J. Phys. Chem.*, 99, 3068 (1995).

99. Y. Liu, Y. Ozaki, and I. Noda, *J. Phys. Chem.*, 100, 7326 (1995).

100. I. Noda, Y. Liu and Y. Ozaki, *J. Phys. Chem.*, 100, 8665 (1996).

101. I. Noda, Y. Liu and Y. Ozaki, *J. Phys. Chem.*, 100, 8674 (1996).

102. E. Y. Jiang and K. Kempfert, *"Oxidation Profile Analysis of a Weathered Polyethylene Electric Insulator Using FTIR Microscopic Mapping and Generalized 2D Correlation Spectroscopy."* Thermo Scientific Application Note: AN01128, Madison, WI (2001).

103. T. Nishioka, Y. Ren, N. Tsubahara, K. Nakashima, I. Noda, and Y. Ozaki, *Anal. Sci.*, 17, i689 (2001).

104. I. Noda, Y. Liu and Y. Ozaki, *Proceedings of the 15th International Conference on Raman Spectroscopy*, paper 514, Pittsburgh, PA, August 1116, (1996).

105. J. Burie, Appl. Spectrosc., 50, 861 (1996).

106. Y. Ozaki, *"2D Correlation Spectroscopy in Vibrational Spectroscopy,"* in the *"Handbook of Vibrational Spectroscopy,"* Eds., J. M. Chalmers, P. R. Griffith, John Wiley & Sons, Ltd., Chichester, UK, Vol. 3, 2135 (2001).

107. R. S. Stein, M. M. Satkowski and I. Noda, in *"Polymer Blends, Solutions, and Interfaces,"* Eds. I. Noda and D. N. Rubingh, Elsevier, NY, 109131 (1992).

108. C. Marcott, A. E. Dowrey, and I. Noda, *Anal. Chem.*, 66, 1065A (1994).

109. I. Noda, "*TwoDimensional Infrared Spectroscopy,"* in *Modern Polymer Spectroscopy*, Ed. G. Zerbi, WileyVCH, Weinheim, 132 (1999).

110. H. Wang, R. A. Palmer, J. R. Schoonover and D. K. Graff, *"Study of Estane Polyester/Polyurethane Block Copolymer by Use of 2DIR DMAFTIR: Understanding of Polymer Rheology from Molecular Dynamics,"* in *TwoDimensional Correlation Spectroscopy*, Eds. Y. Ozaki and I. Noda, AIP Conference Proceedings, 508, Melville, NY (2000).

111. G. M. Story, C. Marcott, and I. Noda, *SPIE* 2089, 242 (1993).

112. 112. C. Marcott, G. M. Story, and I. Noda, paper 1043, *Abstracts of the Pittsburgh Conference on Analytical and Applied Spectroscopy*, New Orleans, LA (1995).

113. E. Y. Jiang, D. L. Drapcho, W. J. McCarthy and R. A. Crocombe, in *Fourier Transform Spectroscopy, Proceedings of the 11th International Conference on Fourier Transform Spectroscopy*, Ed. J. A. deHaseth, AIP Proceedings 430, 380 (1997).

114. Y. Ozaki and I. Noda, *"TwoDimensional Correlation Spectroscopy,"* AIP Conference Proceedings, 508, Melville, NY (2000).

115. H. Wang, R. A. Palmer, *"Further Insights on 2DCorrelation Theory,"* in "*TwoDimensional Correlation Spectroscopy,"* Eds. Y. Ozaki and I. Noda, AIP Conference Proceedings, 508, Melville, NY (2000).

thermo scientific

Notes

Find out more at **thermofisher.com/FTIR**

ThermoFisher SCIENTIFIC

For current certifications, visit thermofisher.com/certifications. © 2021 FEI Company. All rights reserved.
All trademarks are the property of Thermo Fisher Scientific and its subsidiaries unless otherwise specified. WP0026-EN-08-2021